“The impact of granulocyte-macrophage colony-stimulating factor on lung epithelial cell injury and repair in severe influenza virus pneumonia”

Inaugural dissertation

submitted to the Faculty of Medicine

in partial fulfillment of the requirements

for the PhD-Degree

of the Faculties of Veterinary Medicine and Medicine

of the Justus Liebig University Giessen

by

Theresa M. Schäfer

of Marburg, Germany

Gießen, 2025

From the Department of Medicine V, Infectious Diseases, and Infection Control
Director: Prof. Dr. med. Susanne Herold, PhD
of the Faculty of Medicine of the Justus Liebig University Giessen

Chair: Prof. Dr. Martin Diener
Vice-chair and Co-Supervisor: Prof. Dr. Friedemann Weber
First Reviewer and Supervisor: Prof. Dr. Susanne Herold, PhD
Second Reviewer: Prof. Dr. Ali Önder Yildirim

Date of Doctoral Defense: July 16th 2025

Table of Contents

1 Introduction

1.1 Histology of the alveolar region

The alveolar epithelium is comprised of two main cell types, namely alveolar epithelial cells type I (AECI) and type II (AECII), covering approximately 96% and 4% of the alveolar surface.[1] Morphometric analysis has demonstrated that in humans, the blood air barrier consists of around 42% endothelial cells, 11% AECIs, 13% AECIIs, and 35% interstitial cells.[2] In mice, the percentages of the respective cell types are probably very similar to those in humans.[2] Within the alveolar spaces tissue-resident alveolar macrophages (AMs) that have protective function, constitute the first-line defense against inhaled pathogens reaching the alveolar space.[2] Positioned beneath the alveolar epithelium is a dense capillary network surrounded by loose connective tissue composed of elastic and reticular fibers, fibroblasts, myofibroblasts, pericytes, AMs, lymphocytes, mast cells, and a few collagen fibers.[2] This connective tissue, along with the capillaries situated between two adjacent alveolar walls, is termed the alveolar septum.[2]

At multiple sites, there is no connective tissue between the endothelium of the capillary wall and the alveolar epithelium, thereby ensuring optimal gas exchange efficiency.[2] AECIs are thin, elongated cells facilitating gas exchange.[1] They harbor the Na^+, K^+-ATPase (sodium, potassium-adenosine triphosphatase) which enables transcellular sodium transport for fluid clearance, suggesting their potential involvement in maintaining lung liquid homeostasis.[3,4] Due to their elongated shape, AECIs are particularly susceptible to environmental insults rendering them extremely vulnerable to injury.[5,6] Nonetheless, the alveolar epithelium is indispensable for preserving the integrity of the blood-gas barrier.[7] Consequently, the replenishment of AECIs by distal epithelial stem cells following alveolar epithelial injury is essential for the restoration of epithelial barrier function.[8,9]

1.2 Influenza virus infection

Influenza A, B, C, and D viruses belong to the family of *Orthomyxoviridae*[10] characterized by a segmented, single-stranded negative-sense RNA genome.[11] Influenza A virus (IAV) primarily infects epithelial cells lining the respiratory tract, spanning from the upper nasal to the lower alveolar regions.[12,13] The clinical manifestations of IAV infection range from asymptomatic infections to severe pneumonia.[14] In critical disease courses, IAV causes damage to the epithelial-endothelial barrier in the alveolar region, which is associated with edema formation and impaired gas exchange (see chaper 1.3).[15] AEC depletion happens due to both the cytopathic effects of the virus itself and the inflammatory response of the host .[15]

The world health organization (WHO) estimates that approximately 1 billion cases of influenza virus infections, along with 3–5 million instances of severe illness, and 300,000-500,000 fatalities occur during annual influenza epidemics.[11] In Germany, the incidence of influenza-related lower respiratory tract infections across all age groups was 121.6 per 100,000 individuals in 2017.[16] Patients with comorbidities, such as asthma, cardiovascular, hepatic, and renal diseases, obesity, and immunocompromised people are at higher risk for hospitalization and mortality due to IAV infections.[11,14] Typically, elderly individuals (>65 years of age) and infants (< 1 year of age) represent the most vulnerable populations to severe disease progression.[11] Additionally, pregnant women are at heightened risk for severe complications related to IAV infections.[11]

1.2.1 Highly pathogenic avian H5N1 influenza A virus

Since 2020, a panzoonotic wave of highly pathogenic avian influenza A (HPAI) H5N1 infections has been ongoing, posing a risk for the emergence of a new human pandemic IAV strain.[17] Influenza virus subtypes A and B contain the surface proteins haemagglutinin (HA) and neuraminidase (NA) within their envelope.[18] HA binds to sialic acid on epithelial cells, enabling viral entry, while NA cleaves sialic acid to facilitate the virus's release and spread.[18,19] IAV circulates in both humans and animals, particularly birds and mammals.[20] When a host is infected with different HA and NA subtypes, reassortment can occur, leading to increased virus diversity, known as antigenic shift.[11] This phenomenon can result in the emergence of new human pandemic virus strains of zoonotic origin featuring HA and NA surface glycoproteins to which the human immune system has limited pre-existing immunity.[11,21]

Infections with the HPAI H5N1 virus have been documented in over 48 mammal species across 26 countries.[17] The extent of geographic spread and the number of species affected appear to exceed those of previous HPAI outbreaks.[17] The most likely route of transmission to mammals is through close contact with infected birds or their ingestion.[17] Sequencing of H5N1 viruses from mammalian hosts has revealed significant mutations in the polymerase basic protein 2, linked to increased virulence and replication efficiency in mammals.[17,22,23,24] Infected mammals typically exhibit respiratory and neurological symptoms, although subclinical cases have also been documented in individual animals.[17] Between 2003 and 2023, 878 human cases of H5N1 were confirmed, resulting in 458 fatalities, indicating an approximate lethality rate of 52%[17].

Recently, HPAI H5N1 outbreaks in dairy cattle herds were reported across several U.S. states, with efficient cow-to-cow and interspecies transmission (including birds, domestic cats, and a raccoon).[25] In humans, three cases with mild conjunctivitis and respiratory infection were confirmed.[25] However, in November 2024, a Canadian teenager was infected with HPAI H5N1, which was circulating in poultry in British Columbia.[26] The infection led to severe disease progression, including the development of acute respiratory distress syndrome (ARDS).[26] This indicates the virus's zoonotic and pandemic potential, and the need to understand pathomechanisms of influenza-induced lung injury, as well as to define targets for new treatment options.[25]

1.2.2 Prevention and treatments

Vaccines are the most important measure in the prevention of IAV infections.[27] The antibody immune response against IAV mainly targets the surface glycoproteins HA and NA.[28] Due to frequent antigenic drifts, HA and NA exhibit high levels of antigenic variability.[28] Antigenic drift is defined by the gradual accumulation of mutations, particularly at critical antigenic sites within the HA globular head, which occurs due to the lack of proofreading capability in the viral RNA polymerase, combined with the selective pressure imposed by the host immune system.[28,29] Consequently, the seasonal IAV vaccine needs to be reformulated annually to match circulating strains.[28] However, the effectiveness of currently licensed vaccines varies annually, depending on how well the vaccine strains match the circulating viruses.[30] The WHO recommends IAV vaccination to the high-risk groups mentioned above as well as to

healthcare workers.[31] Nevertheless, a 2022 study reported that in Germany, the influenza vaccination rate was about 24% in the general population and only around 13% among pregnant women.[32] Despite the heightened importance of vaccinating the elderly and immunocompromised patients, the influenza vaccine shows lower effectiveness in these patient groups.[33,34,35]

In addition to vaccination, antiviral drugs play a crucial role in the prevention and treatment of IAV infections and diseases.[11] The WHO recommends the use of antiviral drugs for patients at high risk of complications with suspected or confirmed IAV infections.[36] NA inhibitors, such as oseltamivir, function by binding to the active site of NA, mimicking sialic acid binding and thereby blocking viral release from infected cells.[37] Other treatment options include monoclonal antibodies, as well as replication and HA inhibitors.[38] However, drug resistances due to viral mutations remain a significant challenge.[39,38]

Given the limitations of preventive and therapeutic measures to combat severe influenza, it is crucial to identify host pathways that can be targeted for the treatment of severe IAV infections.

1.3 Influenza virus-induced pneumonia and acute lung injury

Typically, IAV infections involve the upper respiratory tract, including trachea and major bronchi. However, among individuals especially within specified risk groups, IAV infections may advance to distal regions of the respiratory system, resulting in alveolar epithelial injury.[40,41] The predominant cell types infected by IAV in the lower respiratory tract comprise ciliated cells, goblet cells, club cells, and AECIIs.[42,43,44,45] The damage to the alveolar epithelium arises from both the cytolytic effect of the virus itself and the side effects of the host's immune response.[46,47,48,49,50] Histopathological examination of IAV-induced lung injury in humans reveals characteristic features, including diffuse pulmonary edema with varying degrees of hemorrhage. Furthermore, observable cytopathic effects on bronchial and alveolar epithelial cells, along with epithelial hyperplasia, are evident.[42,51,52,15]

Primary IAV-induced pneumonia can progress to acute respiratory distress syndrome (ARDS), characterized by hypoxemia, pulmonary edema, and respiratory failure, ultimately leading to multiorgan failure associated with a high mortality rate, reaching up to 60%.[15,53] ARDS can be triggered not only by IAV infections but also by other disease conditions such as sepsis, trauma, or aspiration of gastric contents.[15,54] The acute phase of ARDS is marked by damage to the epithelial-endothelial barrier.[15,54] Severe lung destruction during this phase can result in inadequate repair processes, thereby promoting lung fibrosis.[55]

1.3.1 Pathogenesis of influenza A virus-induced acute respiratory distress syndrome

1.3.1.1 Epithelial cells

Among the first cells within the alveolar region to become infected by IAV are AECIs and AECIIs (Fig. 1.1, p. 7).[15] In a healthy state, AECs form a barrier that restricts the passage of proteins into the alveolar lumen, thereby maintaining an osmotic gradient to prevent the formation of pulmonary edema.[15,53,56] Adjacent epithelial cells form transmembrane tight junctions (including claudins and zona occludens 1, 2, 3) essential for reducing alveolar epithelial permeability and preserving the barrier function.[15,57]

Another crucial factor contributing to the establishment of the osmotic gradient between the alveolar lumen and lung interstitium is ion transport facilitated by several ion transporters and channels expressed by AECs. The epithelial sodium channel

(ENaC), located at the apical surface of AECIs and AECIIs, enables sodium transport from the alveolar lumen into the cytoplasm. Subsequently, sodium ions are actively transported into the interstitium by the Na+, K+-ATPase located in the basolateral membrane of these cells.[15,58,59]

IAV disrupts ion transport across the respiratory epithelium by various mechanisms. IAV infection inhibits the activity of ENaC in the respiratory epithelium. This inhibition is mediated by the activation of phospholipase C and protein kinase C, triggered by the binding of the viral HA to its cell surface receptor.[15,60,61] Additionally, ENaC activity may be inhibited by the viral M2 protein, which induces the production of reactive oxygen species (ROS), leading to the activation of phospholipase C.[15,62] Furthermore, research in our group revealed that IAV infection diminishes the function and abundance of the Na+, K+-ATPase in the plasma membrane of AECs.[63] This effect is induced by paracrine crosstalk between infected and uninfected AECs as well as AMs, resulting in impaired alveolar fluid clearance.[63] The paracrine signaling involves the binding of type I interferon and tumor-necrosis-factor-related apoptosis-inducing ligand (TRAIL) to their respective receptors, interferon-α/β receptor (IFNAR) and death receptor 5 (DR5), expressed on AECs.[63] Consequently, Adenosine monophosphate-activated protein kinase (AMPK) activity is enhanced in AECs, leading to impaired Na+, K+-ATPase function.[63]

Moreover, IAV-induced epithelial cell death is a significant factor in disrupting the epithelial-endothelial barrier, and this process is mediated through various mechanisms.[15] In lung tissue samples from patients with fatal IAV infection, apoptosis in AECs was observed, suggesting its importance in IAV pathogenesis in humans.[15,64] *In vitro* studies using a human bronchiolar epithelial cell line (NCL-H292) have shown that IAV infection leads to caspase 8-dependent apoptosis.[15,65] Expression of the H5N1 non-structural protein 1 (NS-1) alone is sufficient to induce apoptosis in the NCL-H292 cell line.[15,66] Additionally, IAV infection can induce epithelial cell apoptosis by activating protein kinase R, leading to upregulation of proapoptotic genes such as FAS (cell surface death receptor).[15,67] Moreover, the viral NA protein is capable of converting the latent form of Tgf-β into its active form, which binds to its receptor, inducing apoptosis.[15,68] However, *in vitro* infection of primary human bronchial epithelial cells with a mouse-adapted H1N1 IAV results in necrosis rather than apoptosis.[15,69] Furthermore, damage to the epithelial barrier caused by IAV infection

is exacerbated by disruption of tight junction formation, particularly in infections with specific IAV strains containing a PDZ-ligand binding motif in the viral NS-1.[15,70]

1.3.1.2 Endothelial cells

Endothelial cells line the inner surface of capillaries, thereby directly interfacing with circulating blood.[15,53] Upon IAV-induced activation, endothelial cells upregulate the expression of adhesion molecules such as E-cadherin, E-selectin, P-selectin, intercellular adhesion molecule 1 (ICAM1), and vascular cell adhesion molecule 1 (VCAM1), which are crucial for recruiting leukocytes into the alveolar lumen.[15,71,72] Endothelial cells possess a basement membrane on their basolateral side, which is closely associated or fused with the epithelial basement membrane of alveoli, facilitating close contact between AECs and endothelial cells.[15,73] Consequently, cytokine signals or virus particles released from AECs and inflammatory cells in the alveolar lumen profoundly impact endothelial cell activity.[15] The recruitment of leukocytes by activated endothelial cells is essential for mounting an effective immune response against IAV infections.[15] However, an excessive influx of neutrophils and monocytes/macrophages can also compromise alveolar integrity.[15]

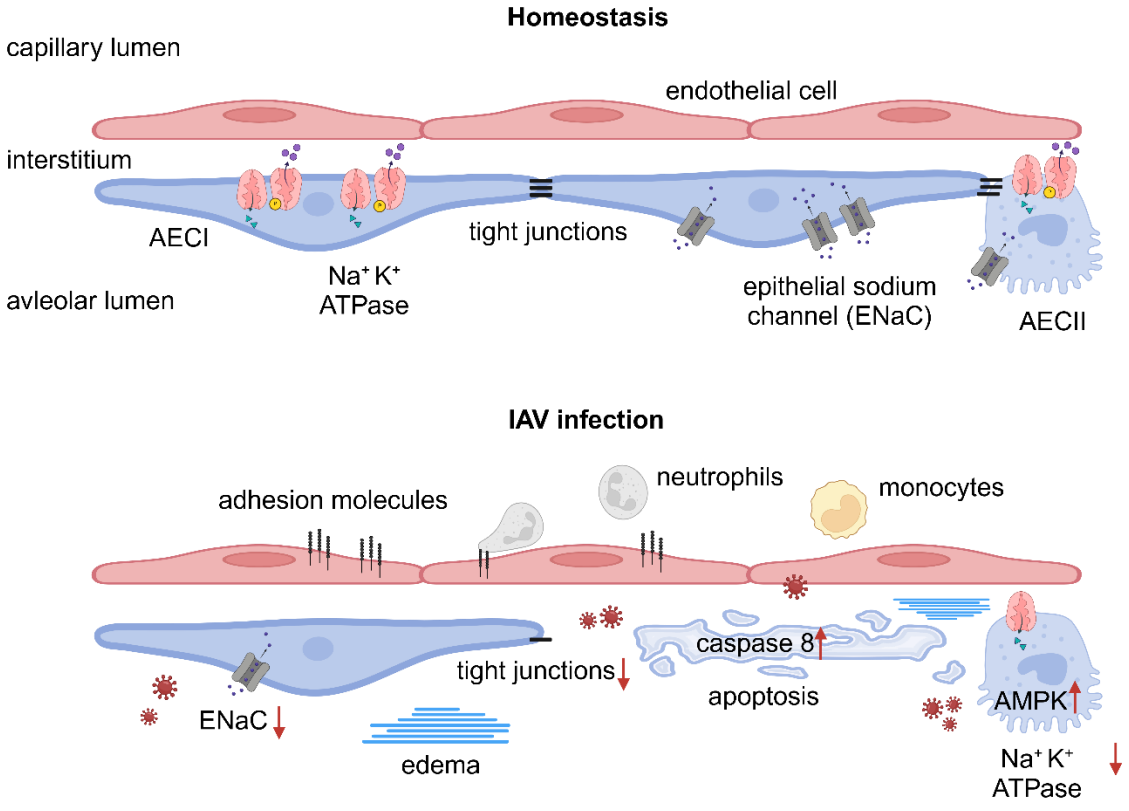

Figure 1.1: IAV infection disrupts the integrity of the epithelial-endothelial barrier by reducing the expression of ion channels and tight junction proteins, while promoting apoptosis. Upon IAV infection, the activity of ENaC in the apical membrane of AECs is diminished.[15,60,61,62] Additionally, IAV-induced activation of AMPK decreases the abundance of Na+/K+ ATPase in the basolateral membrane of AECs.[63] This results in impaired sodium transport, contributing to the formation of pulmonary edema and impaired gas exchange.[63] Furthermore, IAV disrupts tight junctions and induces apoptosis in AECs through caspase 8 activation.[15,65,70] Infected endothelial cells upregulate adhesion molecules, promoting neutrophil and monocyte/macrophage infiltration into the alveolus.[15,71,72] Created with BioRender.com.

1.3.1.3 Neutrophils

Neutrophils are recruited into the alveoli within one day of IAV infection.[15,74] For extravasation, neutrophils adhere to selectins and adherins expressed by endothelial cells, allowing them to transmigrate across the endothelial and epithelial cell layers into the alveolar lumen, where they become activated by locally present cytokines and pathogens.[15,75] Once activated, neutrophils can phagocytose pathogens, forming phagosomes that fuse with intracellular granules to eliminate the internalized pathogens.[15] Granules are also released during degranulation to kill pathogens or remodel tissues.[76,77] The excessive release of neutrophil granular enzymes can cause collateral pulmonary tissue damage in ARDS.[76,78,79]

Additionally, neutrophils release reactive oxygen species (ROS) generated by the activation of the nicotinamide adenine dinucleotide phosphate (NADPH) oxidase complex (NOX2).[15,76,80,81] NOX2, located on the cell membrane, converts oxygen into the superoxide anion, which is then released extracellularly.[76,82,83] The superoxide anion subsequently transforms into hydrogen peroxide (H_2O_2), which can cross cell membranes and, in the presence of myeloperoxidase, forms reactive products such as hydroxyl radicals and hypochlorous acid.[76,82,83] ROS serve multiple functions: they contribute to DNA damage and lysis of target cells, and they also induce intracellular protein phosphorylation and activate transcription factors, leading to the release of inflammatory mediators.[76] However, due to the detrimental effects of ROS on pulmonary tissue, increased neutrophil infiltration can exacerbate the progression of ARDS (see Fig. 1.2).[15,76]

As an additional defense mechanism, neutrophils generate neutrophil extracellular traps (NETs).[15] These extracellular, net-like structures are composed of DNA,

histones, and neutrophil granule proteins, which function to capture and eliminate pathogens.[15,76,84,85] However, excessive formation of NETs can occlude small airways and compromise the alveolar-capillary barrier, potentially resulting in inflammatory lung injury.[76,86,87,88]

1.3.1.4 Macrophages

AMs reside within the alveolar airspace and play a crucial role in maintaining tissue homeostasis by preventing infections and controlling aberrant immune responses.[89,90] Upon infection, the tolerogenic state of AMs is disrupted, prompting these typically anti-inflammatory cells to overcome local immunosuppressive signals and adopt a proinflammatory phenotype.[89,90] AMs coordinate the immune response against viral pathogens by releasing proinflammatory cytokines/chemokines like IL-6, IL-8, or C-X-C motif chemokine ligand 10 (CXCL10), by inducing type I interferon signaling, and increasing pattern recognition receptor expression, as well as reducing nuclear export of viral genome during IAV infection.[90,91,92,93,94,95]

Depletion of the AM pool can occur during the course of disease and is often observed in respiratory viral infections,[90,96,97,98] which is linked to increased morbidity and mortality.[90,99,100,101,102,103,104,105] However, the alveolar niche can be restored through either local AM proliferation or the recruitment of bone marrow-derived macrophages (BMDMs), triggered by chemoattractants like CC-chemokine ligand 2 (CCL2).[90,106] Over an individual's lifespan, different types of injuries typically lead to the gradual replacement of the original yolk sac–derived AMs by BMDMs creating a mosaic of resident macrophages with diverse origins.[90,107,108]

BMDMs exhibit a more proinflammatory profile than AMs, marked by increased release of molecules like tumor necrosis factor α (TNF-α), IL-6, and inducible NOS, aiding in pathogen clearance during the acute phase of infection.[90,100,109,110,111,93] However, BMDMs can also contribute to inflammatory tissue damage.[90] The recruited macrophages express tumor-necrosis-factor-related apoptosis-inducing ligand (TRAIL), which interacts with death receptor 5 (DR5), a receptor upregulated by AECs during IAV infections. This interaction induces apoptosis in AECs.[15,110] Additionally, IAV infection stimulates macrophages to release nitric oxide species (NOS), which subsequently form peroxynitrite, a molecule that can be detrimental to the integrity of the epithelial-endothelial barrier.[15,112,113] All in all, BMDM induced inflammatory tissue damage is characterized by epithelial injury, destruction of the extracellular matrix,

and prolonged cytokine-dependent inflammation. These effects can exacerbate barrier loss and impair gas exchange function, potentially leading to worse disease outcomes.[63,90,96,100,103,110,114, 115,116,117]

1.3.1.5 Adaptive immune system

Adaptive responses are initiated soon after the activation of the innate immune system.[118] In reaction to the initial release of cytokines, pulmonary dendritic cells (DC) migrate to nearby lymph nodes, where they stimulate the activation, proliferation, and differentiation of naïve $CD4^+$ thymus cells (T cells) into various effector $CD4^+$ T cell subsets.[118] Different cytokine milieus influence the differentiation into T helper (T_H)1, T_H2, T_H17, regulatory T cells (T_{reg}), and follicular T helper cells (T_{FH}).[119,120,121] Activated T cells leave the lymphoid tissue and travel to the site of infection.[122,123]

Memory T cells can develop through natural infection or vaccination.[122,124,125] These versatile cells may either remain at the original infection site as tissue-resident memory cells or circulate between tissues as central and effector memory T cells.[122,126,127] Unlike naïve T cells, memory T cells require fewer T cell receptor and costimulatory signals for activation, often depending on proinflammatory signals (e.g. type I interferon (IFN), interleukins (IL) 12, 15, and 18, Toll-like receptors, complement proteins) in a process called “bystander activation”.[122,124,126,127] This activation mechanism enables a rapid response to respiratory viral infections by pathogen-specific and cross-reactive memory T cells but can also lead to nonspecific, widespread T cell activation.[122] Such nonspecific activation can disrupt the balance between effective antiviral immunity and infection-induced inflammation, potentially contributing to prolonged inflammation.[122] Persistent bystander activation of T cells has been associated with severe disease outcomes in patients with SARS-CoV-2 or IAV infections.[122]

Upon antigen presentation by DCs, $CD8^+$ T cells undergo differentiation into cytotoxic or memory $CD8^+$ T cells.[118] $CD8^+$ T cells recognize antigens presented by MHC complexes via their T cell receptors, leading to cytotoxic responses through three primary mechanisms: (1) perforin/granzyme-mediated cytolysis, (2) FasL/Fas signaling, and (3) TRAIL/TRAIL-DR5 signaling.[118] Perforin forms pores in the target cell membrane, allowing granzyme entry to induce apoptosis.[118] FasL binding to the Fas receptor and TRAIL binding to DR5 on infected cells also trigger apoptosis.[118]

In addition to their cytolytic functions, cytotoxic T cells secrete cytokines such as IFNγ, TNFα, and IL-2, which promote the proliferation and survival of cytotoxic T cells and exhibit strong cytotoxic effects.[118] Cytotoxic T cells, along with T_{reg} cells, produce IL-10, which modulates their inflammatory responses, preventing excessive inflammation.[118] Memory T cells can also secrete IL-22, IL-17, and IFNγ independently of T cell receptor stimulation, contributing to the pathology of ALI.[118,128]

T_{H17} cells are the main source of cytokines IL-17A, IL-17F, IL-21, and IL-22.[118] The key cytokine IL-17 stimulates the production of chemokines C-X-C motif chemokine ligand 9 (CXCL9) and CXCL10 for the recruitment of neutrophiles.[118] Lipopolysaccharide (LPS)-induced ARDS in mice caused a clonal expansion of T_{H17} cells in the lungs, leading to increased alveolar epithelial permeability.[118,129] Reduced permeability was observed with T_{H17} cell deficiency, IL-17 receptor loss, or anti-IL-17 treatment.[118,129] Inhibiting IL-17 and IL-22 decreased neutrophil and macrophage recruitment while increasing T_{reg} cells.[118,130] Human studies showed elevated IL-17A in bronchioalveolar lavage fluid (BALF) from ARDS patients and higher T_{H17} cells in children with severe sepsis-induced ALI.[118,129,131] Despite their inflammatory role, T_{H17} responses may aid lung repair through IL-22.[118,132]

Sawitzki et al. found that the IgG Fc receptor CD16 on $CD38^+$ $CD4^+$ and $CD8^+$ T cells enables TCR-independent degranulation and cytotoxicity. This process results in microvascular endothelial cell damage and heightened inflammation by attracting neutrophils and monocytes. Consequently, this leads to tissue damage and contributes to severe disease in COVID-19 and other respiratory infections.[115,122,133,134,135]

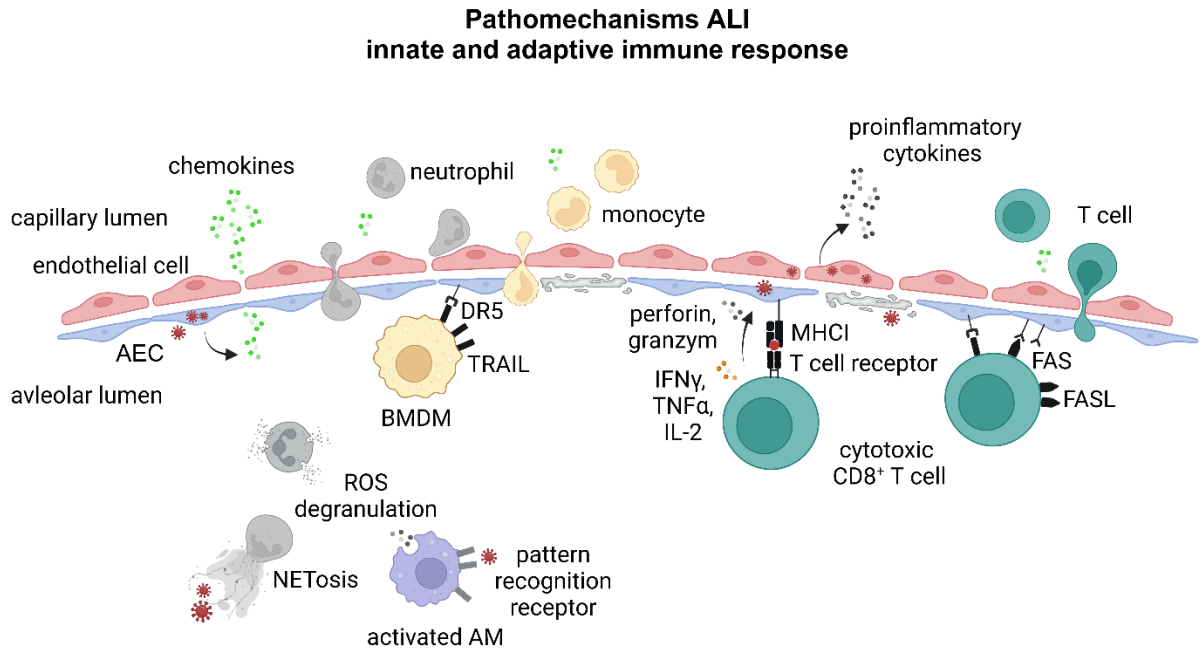

Figure 1.2: Innate and adaptive immune responses contribute to the pathogenesis of acute lung injury (ALI). Infected AECs secrete chemokines that recruit neutrophils, monocytes and T cells, while infected endothelial cells produce proinflammatory cytokines, further amplifying the inflammatory response.[15] This inflammation compromises the integrity of the epithelial-endothelial barrier through multiple mechanisms: excessive release of NOS/ROS and granule contents from activated AMs and neutrophils, along with neutrophil extracellular traps (NETs), all of which are harmful to lung tissue.[15,110,112,113] Additionally, BMDMs are recruited to the lung, where they adopt a proinflammatory phenotype and induce AEC apoptosis via TRAIL/DR-5 signaling.[15,90,110] Cytotoxic CD8+ T cells further contribute by recognizing infected AECs through T cell receptor/MHCI interactions, leading to the release of perforin and granzyme, and inducing apoptosis via TRAIL/DR-5 and FAS/FASL signaling pathways.[118] Created with BioRender.com.

1.3.2 Metabolic changes in AECs during IAV infection

Prior investigations have demonstrated that IAV infection induces activation of adenosine monophosphate kinase (AMPK),[63] a master regulator of cell metabolism.[136] AMPK constitutes a heterotrimeric complex comprising one catalytic α-subunit and two regulatory β- and γ-subunits.[137] Activation of AMPK occurs upon binding of adenosine monophosphate (AMP) or adenosine diphosphate (ADP) to the γ-subunit, whereas adenosine triphosphate (ATP) competitively hinders the binding of both AMP and ADP to the γ-subunit.[137] Consequently, AMPK is triggered under cellular stress conditions in response to an elevation in the ratios of AMP:ATP and ADP:ATP.[136,137] Activated AMPK functions restore cellular energy levels by inhibiting energy-consuming anabolic processes while inducing catabolic pathways to regenerate ATP levels.[136,137] Multiple studies suggest that activated AMPK suppresses cell growth and proliferation primarily through direct inhibition of the mechanistic target of rapamycin complex 1 (mTORC1), a key regulator of cell proliferation downstream from AMPK.[136,138] Notably, Ishii et al. (2009) has shown that macrophage proliferation is suppressed upon AMPK activation.[139]

And vice versa, AMPK inhibition and subsequent activation of mTORC1 increases cell growth and proliferation: activated mTORC1 phosphorylates its effectors, 70-kDa ribosomal protein S6 kinase (p70S6K) and eukaryotic initiation factor 4E (eIF4E)-binding protein 1 (4EBP1).[140] Phosphorylated p70S6K recruits the 40S ribosomal subunit to form active translation polysomes, enhancing the translation of mRNAs encoding ribosomal proteins or elongation factors crucial for cell growth.[140] Another target of mTORC1 is eIF4E, a subunit of the mRNA cap-binding complex eukaryotic initiation factor 4F (eIF4F).[140] Phosphorylation of 4EBP1 by mTORC1 and other kinases leads to eIF4E dissociation from 4EBP1, joining the 5' cap-binding complex eIF4F.[140] This increases the translation of specific mRNAs essential for the G1-to-S phase transition of the cell cycle, such as cyclin D1 (*Ccnd1)* and *cMyc*.[140]

1.3.3 Diagnosis and treatment of acute respiratory distress syndrome

The Berlin definition of ARDS outlines four main criteria for the diagnosis of ARDS.[141] Firstly, the onset of symptoms is acute which means within one week of a known clinical insult.[141] Secondly, ARDS patients typically experience hypoxemia, which is categorized into three severity levels.[141]

- mild: 200mmHg <PaO2/FIO2 ≤ 300mmHg with PEEP or CPAP ≥5cm H2O
- moderate: 100mmHg <PaO2/FIO2 ≤ 200mmHg
- severe: PaO2/FIO2 ≤ 100mmHg

(PaO2: partial pressure of arterial oxygen; FIO2: fraction of inspired oxygen; PEEP: positive end-expiratory pressure; CPAP: continuous positive airway pressure)[141]

The third criterion states that edema attributable to heart failure must be excluded as the underlying cause for lung failure.[141,142] Lastly, chest radiographs of ARDS patients must demonstrate bilateral opacities that cannot be entirely accounted for by effusions, lobar or lung collapse, or nodules.[141]

While mechanical ventilation remains the primary tool for managing ARDS, its implementation follows recent guidelines aimed at minimizing ventilator-induced lung injury.[141] Pharmacological treatments targeting the underlying mechanisms of ARDS, such as β2 agonists,[143,144,145] statins,[146,147] and keratinocyte growth factor[148], have not demonstrated beneficial effects and have been associated with harm.[141] However, a promising candidate for ARDS treatment is granulocyte-macrophage colony-stimulating factor (GM-CSF).[149]

1.4 Lung regeneration and repair

Following IAV infection, multiple processes are required to restore the integrity of the alveolar epithelial barrier.[150] Primarily, stem/progenitor cells within the (bronchio)alveolar epithelium play a critical role in the regeneration of the epithelial layer.[150] Additionally, the restoration process needs a well-coordinated interaction between the epithelial and immune cell compartment.[150]

1.4.1 Epithelial compartment

1.4.1.1 AECII

The morphology of AECIIs is characterized by a cuboidal shape, lamellar bodies, and distinct apical microvilli.[3,151] A primary function of AECIIs is the synthesis and secretion of surfactant aimed to reduce alveolar surface tension preventing lung parenchymal collapse (atelectasis).[3,152] Surfactant primarily consists of phospholipids but also contains surfactant proteins A, B, C, and D, which possess antimicrobial and anti-inflammatory properties.[3,153] Following alveolar epithelial injury, AECIIs are recognized to serve as progenitor cells for AECIs (see Fig. 1.3).[154,155] In case of acute lung injury, AECIs are decimated, yet their replenishment is facilitated by residual AECIIs.[1,156,157]

During lung development in mice, a bipotent progenitor cell gives rise to both AECIs and AECIIs, a process that continues until the lung reaches full maturation a few weeks after birth.[8,158] In the adult mouse lung, a small subset (1%) of all mature AECIIs exhibits stem cell properties, characterized by multipotency, self-renewing capacity, and lifelong persistence.[8,158] These cells serve as progenitors for both AECIs and AECIIs.[8,158] Renewal events occur within monoclonal foci each originating from a single, self-renewing AECII and gradually expanding over time, forming what is termed an alveolar renewal focus.[158] Barkauskas et al. (2013) elucidated that in co-culture with platelet-derived growth factor receptor α (Pdgfrα)-positive mesenchymal cells, individual AECIIs possess the capability to differentiate into alveolar-like structures termed alveolospheres.[8] These organoids encompass not only mature AECIIs but also cells with AECI marker expression.[8]

In the trans-differentiation process of AECIIs into AECIs, wingless-related integration site (Wnt) signaling plays an essential role.[159,160,161] Nabhan et al. identified a subset of Axin-like protein (Axin2) positive AECIIs with active Wnt signaling.[162,161] This AECII population is termed as alveolar epithelial progenitors (AEPs).[150] $Axin2^{+}$ AEPs are

found in close proximity to single, Wnt-expressing fibroblasts.[162] Maintaining Wnt signaling prevents transdifferentiation of Axin2$^+$ AEPs into AECIs, whereas abrogation of Wnt signaling facilitates this process.[162] Following injury, autocrine Wnt signals transiently promote expansion of the progenitor pool.[162] Wnt-responsive AEPs displayed heightened sensitivity to fibroblast growth factor (Fgf) signaling through Fgf7 and Fgf10 in organoid cultures, compared to non-AEP AECIIs.[150] Moreover, the differentiation of AECIIs into AECIs is enhanced upon the loss of fibroblast growth factor receptor 2 (Fgfr2), suggesting that Fgf signaling helps to preserve the AECII fate in response to injury.[150,163]

Within the last years, single cell RNA sequencing has revealed new AECII subpopulations that differ in their gene expression profiles.[150] It has been shown that during alveolar regeneration, airway and alveolar epithelial stem cells (Club cells and AECIIs) transition into a keratin 8 (Krt8) positive transitional cell state characterized by activation of specific gene programs and morphologic changes towards a squamous shape.[164] These Krt8$^+$ alveolar intermediate cells (ADIs) precede the regeneration of AECIs.[164] ADIs are characterized by high expression of marker genes such as *Krt8* and Claudin 4 (*Cldn4*), occurring after bleomycin injury.[165] Moreover, in the single cell RNA sequencing analysis, cycling AECIIs with high expression of proliferation markers like KI 67 (*Mki67*) and cyclin dependent kinase 1 (*Cdk1)* were identified, along with primed AECIIs displaying reduced expression of essential AECII lineage markers.[165] Pseudotime analysis unveiled a differentiation trajectory of AECIIs towards AECI cell fate, transitioning through primed AECIIs and ADIs during regeneration.[165] It has been demonstrated that in idiopathic pulmonary fibrosis AECIIs are unable to proceed with differentiation into AECIs and remain trapped in the ADI cell state.[164,166] Krt8$^+$ alveolar epithelial cells have also been observed in human lung tissue sections from patients with ARDS caused by IAV and pneumococcal infection.[164]

Furthermore, the Hippo signaling pathway is crucial for stem cell renewal and cellular mechanotransduction.[150,167,168] When Hippo is active, the transcriptional effectors Yap and Taz are in the cytoplasm; when inhibited, they move to the nucleus to regulate gene expression.[150,169] Yap promotes AECII proliferation and inhibits differentiation into AECIs during lung injury.[150,170]

The Tgf-β superfamily also influences AECII self-renewal and differentiation, with high Bmp signaling promoting AECII-AECI differentiation and its inhibition promoting AECII self-renewal.[150,171] Transforming growth factor (Tgf)-β inhibitors are often used in organoid models to enhance AECII cell growth post-injury.[150,163,172]

However, after severe IAV infection, dysplastic epithelial repair can occur, marked by the occurrence of cuboidal Krt5$^+$ epithelial cells that fail to reconstitute the functional alveolus.[150,173,174,175,176] They originate from a lineage of epithelial cells in the distal airways that express transformation related protein 63 (Trp63), known as lineage-negative epithelial progenitors (LNEPs).[150,174,177] The accumulation of Krt5$^+$ clusters in response to hypoxia is dependent on the expression of hypoxia-inducible factor 1α (HIF1α).[150,178] Furthermore, the expansion of Krt5$^+$ cells is driven by Notch signaling, which is induced by local hypoxia during severe IAV infection.[150,178] In contrast, Wnt/β-catenin signaling promotes the differentiation of LNEPs into AECIIs.[150,178]

1.4.1.2 BASC

Another cell type implicated in alveolar epithelial renewal is the bronchioalveolar stem cell (BASC), located at the bronchioalveolar duct junctions.[9,179] BASCs represent a rare population co-expressing surfactant protein C (Sftpc, AECII marker) and secretoglobin family 1A member 1 (Scgb1a1, club cell marker).[179] These cells possess self-renewal capabilities and can not only give rise to AECIIs and AECIs but also to club and ciliated cells.[179] Thereby, BASCs serve as progenitor cells for both the alveolar and bronchiolar compartments.[179] Previous investigations have demonstrated self-renewing capacity and multipotency in isolated BASCs.[180,181] *In vivo* lineage tracing studies and intersectional genetics have further revealed that BASCs are epithelial stem cells contributing to alveolar and bronchiolar regeneration following lung injury.[9,182]

The structure of the human lung is different from that of mice.[183] Humans have respiratory bronchioles, which are absent in mice.[183] In the human lung, respiratory airway secretory (RAS) cells have been discovered within these respiratory bronchioles.[183] These RAS cells can differentiate into AECIIs through processes mediated by Notch and Wnt signaling.[183] RAS cells play a crucial role in regenerating and maintaining the alveolar niche in humans.[183]

Recently, the bronchioalveolar lung organoid (BALO) model has been established by our group.[179,184] In this model, BASCs and a distinct population of mesenchymal stem cells (rMCs) are co-cultured to facilitate the development of BALOs.[179,184] Each BALO originates from a single BASC which undergoes clonal expansion and generates branched organoid structures through self-organization within a period of 21 days.[179,184] BALOs accurately recapitulate the bronchioalveolar compartment of the lung and consist of various differentiated cell types, including secretory, basal, and ciliated cells as well as AECIs and AECIIs.[179,184] In general, the BALO model is a valuable tool for investigating epithelial-mesenchymal-(immune) cell interactions and facilitates the study of injury and repair mechanisms associated with IAV infection.[179,184]

To enrich BASCs (defined as $Sftpc^{+}Scgb1a1^{+}$), a population of epithelial cellular adhesion molecule $(EpCAM)^{high}CD24^{low}Sca\text{-}1^{+}$ cells is isolated and then co-cultured with resident mesenchymal cells (rMCs) (defined as $EpCAM^{-}Sca\text{-}1^{+}$) for the generation of BALOs.[184,42] However, the enriched BASC population comprises not only $Sftpc^{+}Scgb1a1^{+}$ double-positive cells but also $Sftpc^{+}Scgb1a1^{-}$ as well as $Sftpc^{-}Scgb1a1^{+}$ single-positive cells.[184] This heterogeneity results in organoids with distinct morphologies, with BALOs constituting the majority (80%) of the organoids.[184] Additionally, bronchiolospheres derived from $Scgb1a1^{+}$ club cells account for 11% of all organoids, while alveolospheres derived from $Sftpc^{+}$ AECIIs make up the remaining 9%.[184]

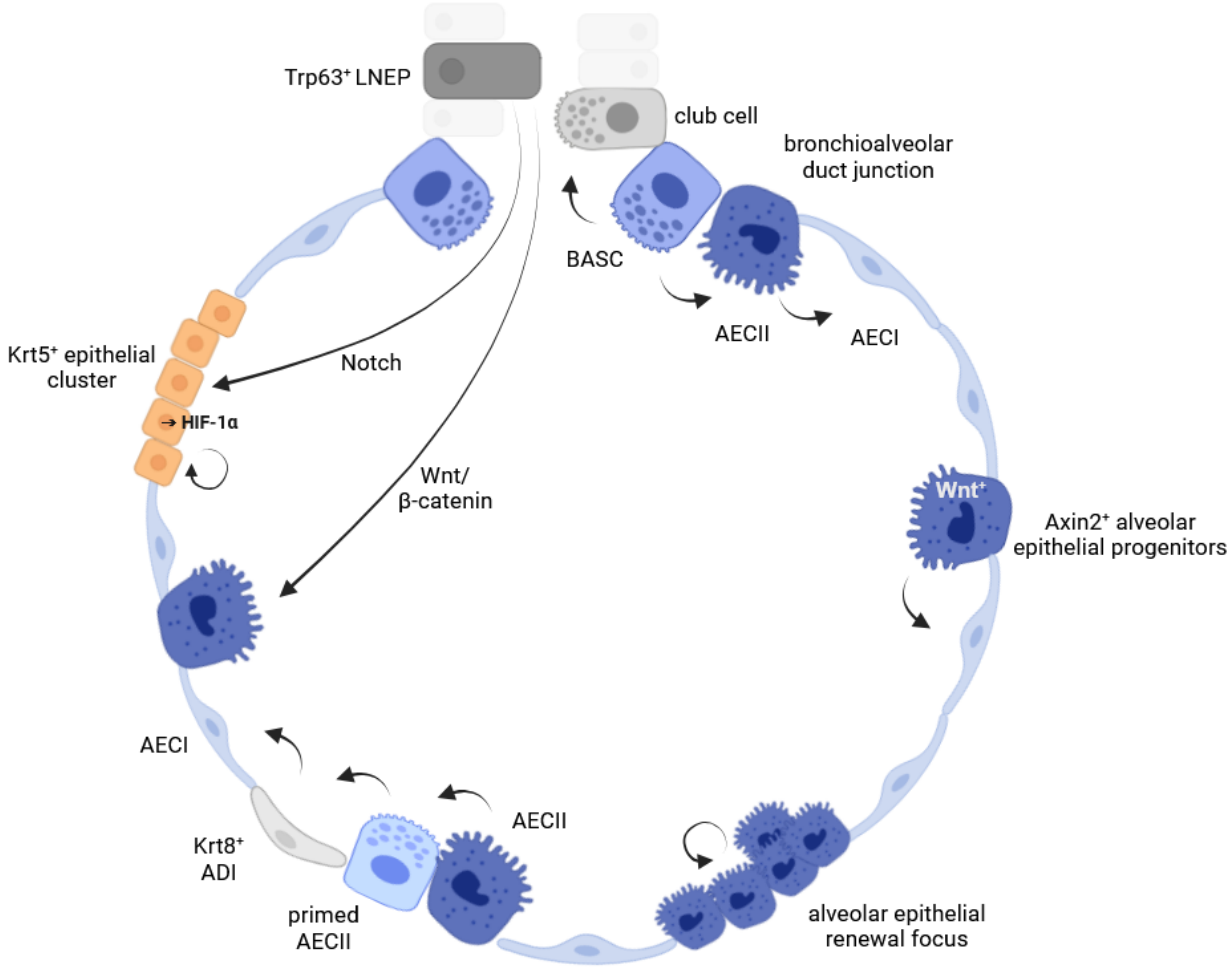

Figure 1.3: Alveolar epithelial repair is facilitated by various stem cell populations. BASCs, located at bronchioalveolar duct junctions, have the capacity to regenerate both bronchiolar and alveolar epithelium by differentiating into Club cells or AECIIs.[179] Additionally, Axin2⁺ alveolar epithelial progenitors give rise to AECIs by Wnt signaling.[158] AECII expansion occurs in an alveolar epithelial renewal focus, originating from a single, self-renewing AECII.[158] Recent findings indicate that the differentiation of AECIIs into AECIs progresses through distinct cellular states, including primed AECIIs and Krt8⁺ ADIs.[165] Trp63⁺ LNEPs, located in the peribronchiolar region, can either differentiate into AECIIs via Wnt/β-catenin signaling or mediate dysplastic repair by generating Krt5⁺ epithelial cells through Notch signaling.[150,178] In response to hypoxia, HIF1α expression leads to the accumulation of Krt5⁺ clusters.[150,178] Created with BioRender.com.

1.4.2 Immune signaling mediating epithelial repair

While cytokine signaling is often studied for its impact on immune cells, recent research shows that inflammatory cytokines also promote alveolar epithelial cell growth.[150] *In vitro* studies with AECII organoids revealed that cytokines like TNF-α, IL-1, and IL-17 enhance epithelial cell proliferation, increasing the organoid size.[150,185] IL-1β, produced by interstitial macrophages, induces a transcriptional response in AECIIs resembling intermediate states in AECII-to-AECI transition (see Fig. 1.4).[150,165] Prolonged IL-1β signaling inhibited full AECII-to-AECI differentiation, but removing IL-1β enabled it.[150,165]

Another important cytokine in aiding alveolar epithelial regeneration is IL-10, expressed by AECIs, AECIIs, and macrophages. It restrains inflammation by suppressing cytokines like IL-1, IL-6, and TNF-α.[150,186,187,188] T_{reg} cells help to control excessive inflammation and restore homeostasis by releasing IL-10 and TGF-β.[118] TGF-β plays a crucial role in epithelial growth, regeneration, and maintaining homeostasis between the epithelium and the innate immune system.[150] It was shown that TGF-β receptor expression in $CD11c^+$ myeloid cells is essential for AM development.[150,189] Overall, TGF-β supports AM maintenance while limiting excessive inflammation.[150]

To support inflammation resolution and tissue repair, AMs release immunomodulatory cytokines, including IL-10 and C-C motif chemokine ligand 2 (CCL2), along with various growth factors such as TGF-β, vascular endothelial growth factor (VEGF), trefoil factor 2, and PDGF.[90] TNF-α released from AMs has been shown to stimulate the release of GM-CSF from AECIIs, thereby supporting alveolar epithelial repair.[90,190]

Moreover, in the repair phase, a drop in interferon levels causes a significant increase in epithelial proliferation and differentiation.[150,191] The anti-inflammatory effects of T_{reg} cells are partially ascribed to the suppression of $CD8^+$ T cell IFNγ production.[118,192]

Further mediators of alveolar epithelial repair are placenta-expressed transcript 1 (Plet1) and amphiregulin. Plet1, which is highly expressed by AMs and regenerative BMDMs, induces proliferation of AECs and facilitates the re-sealing of the alveolar epithelial barrier.[193] Amphiregulin, which is produced by ALI lung tissue and activated

AMs upon LPS challenge, inhibits TNF-α-induced apoptosis and caspase signal transduction in AECs.[194]

AECs transmit immunomodulatory signals to AMs through CD200-CD200R interactions.[150] AECIIs express CD200, which binds to CD200R on AMs.[150,195,196] CD200 knockout mice show milder influenza symptoms and less lung inflammation, aligning with findings that monocytes and macrophages can cause inflammatory lung damage during IAV infection.[150,195,197]

The distal lung balances protection from environmental insults with controlling inflammation through interactions between AECs and macrophages.[150] During viral infections, these interactions activate antiviral defenses, recruit leukocytes, and halt epithelial proliferation, which resumes after virus clearance.[150] The coordination of these processes remains under investigation.[150]

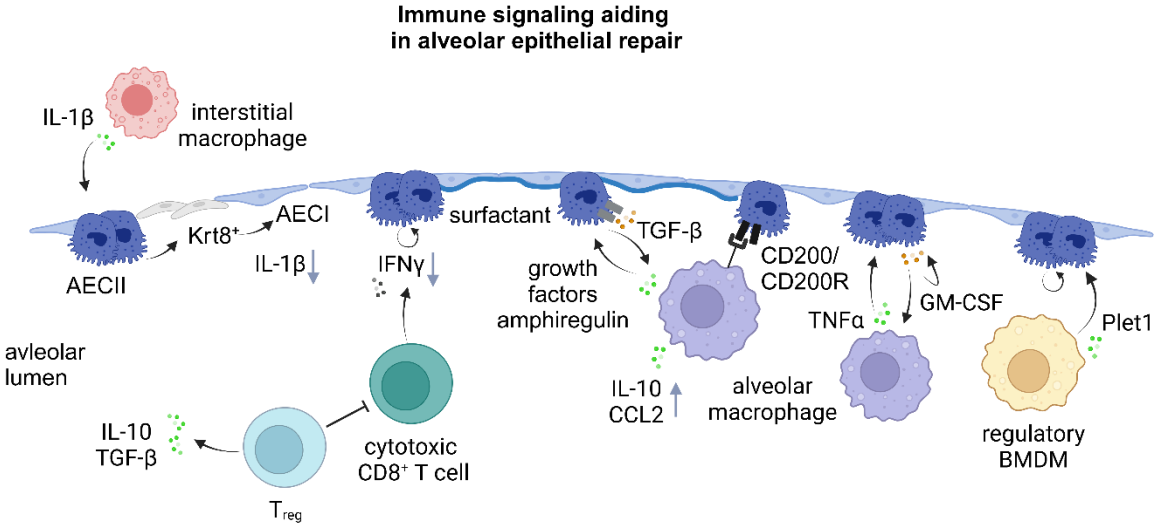

Figure 1.4: Immune signaling aids in alveolar epithelial repair. IL-1β, produced by interstitial macrophages, induces the transition of AECIIs into an intermediate cell state. The subsequent decrease in IL-1β levels allows for their full differentiation into AECIs.[150,165] Concurrently, T_{reg} release anti-inflammatory cytokines (IL-10, TGF-β) and suppress cytotoxic $CD8^+$ T cells, leading to a reduction in IFNγ release.[118,192] The decline in type I and II IFNs promotes the growth and proliferation of AECIIs, which is essential for alveolar epithelial regeneration.[150] Crosstalk between the alveolar epithelium and AMs is also essential for proper lung regeneration.[150] AMs release growth factors and amphiregulin, which promote AEC growth and protect them from apoptosis.[90,194] The presence of the cell surface ligand CD200 on AECIIs transmits immunoregulatory signals to AMs via the CD200 receptor (CD200R).[150] TGF-β bound to integrin αVβ6 on AECs is crucial for maintaining AMs and limiting their inflammatory response.[150,198,199,200,201] TNF-α released from AMs stimulates GM-CSF production by AECIIs, which not only enhances alveolar epithelial repair in an autocrine manner but is also crucial for sustaining AM function.[90,150,190] Moreover, both AMs and regenerative BMDMs express Plet1, which promotes AEC proliferation and enhances repair of the alveolar epithelial barrier.[193] Created with BioRender.com.

1.5 Granulocyte-macrophage colony-stimulating factor

1.5.1 Biology and major functions

GM-CSF, also referred to as colony-stimulating factor 2 (Csf2), was initially identified as a hematopoietic-cell growth factor due to its capacity to induce proliferation and differentiation of bone marrow-derived myeloid precursor cells, leading to the formation of granulocytic and macrophage colonies *in vitro*.[202,203,204,205,206]

GM-CSF is a glycosylated secreted protein comprising a single polypeptide chain. The GM-CSF receptor is a heterodimer consisting of a specific ligand-binding subunit, colony-stimulating factor 2 receptor α (Csf2rα), and a common signal-transduction subunit, colony-stimulating factor 2 receptor β (Csf2rβ).[202,203,207,208,209] Notably, the Csf2rβ chain is responsible for facilitating signal transduction and is also utilized by IL-3 and IL-5. In contrast, the α chain does not participate in signaling but confers cytokine specificity.[210] Several ways of signal transduction initiated by GM-CSF have been described. In macrophages the interaction of GM-CSF with its receptor induces phosphorylation of two different domains in the β-chain of the receptor which activates the janus kinase 2 (JAK2) and signal transducers and activators of transcription 5 (STAT5) pathway and the mitogen activated protein kinases (MAPK) or the phosphoinositide 3-kinase (PI3K)/ proteinkinase B (PKB/Akt) pathway.[211] The PI3K/Akt pathway resides upstream of AMPK and mTORC1, capable of both inhibiting AMPK and activating mTORC1 through direct or indirect mechanisms.[212]

GM-CSF is known for its immunomodulatory functions, facilitating the proliferation, differentiation, and activation of monocytes, granulocytes, macrophages, and DCs *in vivo*.[201,202,213] A pro-inflammatory network has been proposed, involving macrophages and neighboring tissue resident cells (such as fibroblasts, endothelial, and epithelial cells), as well as T cells, communicating through GM-CSF and the pro-inflammatory cytokines like IL-1 and tumor necrosis factors (TNF). This intercellular crosstalk may potentially establish a positive feedback loop leading to chronic inflammatory or autoimmune diseases.[201,202] Nonetheless, GM-CSF has been demonstrated to regulate the homeostasis of nonlymphoid tissue-resident DCs[214] and is indispensable for the development of inflammatory macrophages and monocytes during infections.[214,215] The GM-CSF-dependent interaction between AECs and $CD103^+$ DCs is crucial for effective viral clearance and recovery from lung injury following IAV infection.[216]

1.5.2 Pulmonary GM-CSF during IAV infection

In the lung, GM-CSF has been demonstrated to play a role in mediating allergic airway inflammation.[217,218] Conversely, during bacterial and fungal infections, GM-CSF exhibits a protective effect by promoting the differentiation and activation of pulmonary DCs and macrophages.[219,220,221] Moreover, GM-CSF is vital for maintaining lung homeostasis and normal pulmonary physiology. In patients suffering from pulmonary alveolar proteinosis (PAP), GM-CSF or GM-CSF receptor dysfunction or auto-antibodies can be identified resulting in impaired phagocytic functions of AMs.[201,222] Consequently, surfactant proteins and phospholipids accumulate in the alveolar lining fluid, resulting in impaired gas exchange and increased susceptibility to microbial infections.[201,221,223]

One of our previous studies by Unkel et al. (2012) revealed that AECs are the primary source of GM-CSF in the distal lung at baseline and in particular upon PR8 infection.[216] While macrophages, endothelial cells, fibroblasts, and T cells are among the cell types capable of producing GM-CSF, AECs were identified as the exclusive $CD45^-$ cell population within the distal lung parenchyma that increases GM-CSF expression following IAV infection, leading to elevated GM-CSF levels in the alveolar lining fluid.[216,201] Additionally, Ito et al. (2015) demonstrated that GM-CSF secretion by AECs after IAV infection is mediated by hepatocyte growth factor (HGF)/ mesenchymal-epithelial transition factor (c-Met) and transforming growth factor-α (Tgf-α)/ EGFR signaling pathways.[224,201] Furthermore, our previous studies showed that TNF-α released from activated AMs following LPS challenge induces epithelial GM-CSF expression, which subsequently triggers proliferation of AECIIs and facilitates barrier repair.[190]

1.5.2.1 Alveolar macrophage functions are mediated by GM-CSF

Tissue-resident AMs originate from fetal monocytes that migrate to the lung during prenatal development, specifically around embryonic days E12.5 to E16.5.[225,226,227] The initial signs of AM differentiation become evident during the saccular stage of lung development (E18.5).[225] During this stage, the expression of the transcription factor PPAR-γ, which is dependent on GM-CSF, is crucial for the local differentiation of fetal monocytes into AMs within the lungs.[199] In the adult lung, the maintenance of AMs is dependent on GM-CSF and Tgf-β, which both activate the transcription factor PPAR-γ.[90,225,228,189] Circulating monocytes have a minimal role in contributing to the

steady-state AM population, likely due to the sequestration of the AM microenvironment from circulation under homeostatic conditions.[225,228,229,230] This isolation may account for the self-renewal capacity of AMs, enabling them to recover from minor losses without significant peripheral input.[90]

It has been shown that GM-CSF has a protective effect during IAV infection by enhancing AM activity.[231] GM-CSF plays a crucial role in the terminal differentiation and activation of AMs by upregulating the myeloid master transcription factor, PU.1.[201,221,222] The expression of PU.1, stimulated by GM-CSF, is essential for Fcγ receptor (FcγR) expression in AMs. Additionally, the interleukin-18/interleukin-12 stimulated crosstalk between AMs and natural killer cells (NK cells) or T cells upon pathogen exposure also depends on GM-CSF-mediated PU.1 expression augmenting FcγR expression and hence, the phagocytic function of AMs.[232] Moreover, elevated GM-CSF levels in transgenic mice result in AMs displaying higher resistance to apoptosis, providing protection against lethal courses of IAV infection.[201,233] Furthermore, GM-CSF mediates enhanced production of ROS in AMs, thereby reducing susceptibility to secondary bacterial pneumonia subsequent to sublethal IAV infections.[234]

1.5.2.2 GM-CSF enhances adaptive immunity

The protective effects of GM-CSF during viral or bacterial infections can not only be attributed to elevated innate immune functions but also enhanced adaptive immunity.[201] GM-CSF released by AECs activates pulmonary $CD103^+$ DCs, promoting their migration to the mediastinal lymph nodes (MLN) for the priming of $IFNγ^+CD4^+$ and $IFNγ^+CD8^+$ T-cells.[201,216] This GM-CSF-mediated increase in the recruitment of antigen-specific T-cells to the lung enhances viral clearance and facilitates recovery from epithelial injury.[201,216] Moreover, GM-CSF is secreted by naïve $CD8^+$ T-cells during priming in the MLNs, serving as a licensing factor for DC activation, thereby enhancing T-cell proliferation in a positive feedback loop.[201,235] Additionally, GM-CSF signaling regulates the homeostasis of nonlymphoid tissue-resident DCs, which are crucial for the induction of $CD8^+$ T-cell immunity upon antigen challenge.[201,214] Furthermore, GM-CSF promotes the maturation of DCs, B-cells, and T-cells, thereby enhancing antigen-specific antibody responses against IAV.[201,236]

1.5.2.3 Alveolar epithelial repair is facilitated by GM-CSF

GM-CSF protects from alveolar epithelial injury and enhances survival upon IAV pneumonia in mice.[237] Additionally, following LPS-induced acute lung injury, GM-CSF promotes AECII proliferation and facilitates restoration of the alveolar barrier.[190] In hyperoxic conditions, GM-CSF maintains the integrity of the epithelial barrier by reducing apoptosis of cells in the alveolar wall.[238] Furthermore, during oxidative stress, the expression of GM-CSF is inhibited by microRNAs (miR133a and miR133b), which downregulate GM-CSF mRNA translation.[239]

Interstitial lung disease encompasses a group of diverse lung disorders marked by inflammation and fibrosis of the pulmonary parenchyma.[240] GM-CSF plays a role in the progression of pulmonary fibrosis, as its levels are elevated in the bronchioalveolar lavage fluid (BALF) of affected patients.[240] GM-CSF induces macrophages to release profibrotic cytokines and directly promotes fibrosis in airway smooth muscle cells.[240,241,242]

Elevated concentrations of GM-CSF in the alveolar fluid have been correlated with enhanced epithelial barrier function and improved survival among patients suffering from ARDS.[243,244] Accordingly, apoptosis in neutrophils is diminished following *ex vivo* treatment with BALF containing elevated concentrations of GM-CSF, obtained from patients with ARDS.[243] In inflamed human lung tissue sections, hyperplastic AECIIs expressing GM-CSF have been observed, which lead to the accumulation of $CD1a^+$ DCs[245]. However, in critically ill children infected with IAV, high levels of GM-CSF in the blood have been associated with innate immune suppression and mortality.[246] This highlights that the beneficial effects of GM-CSF are predominantly attributed to its presence within the alveolar compartment rather than its systemic distribution.[201] However, the molecular mechanisms underlying GM-CSF-mediated alveolar epithelial repair remain elusive.

1.5.2.4 Animal models of GM-CSF deficiency

Csf2-/- (as well as Csf2rβ-/-) mice develop an accumulation of surfactant phospholipids and proteins in the lung resembling PAP in humans.[221,247] In Csf2-/- mice alveolar macrophages appear as enlarged, foamy, and without inclusions.[221] Moreover, in the alveolar regions, amorphous eosinophilic material can be found.[221] Due to these impairments, Csf2-/- mice have a high susceptibility to opportunistic

bacterial and fungal infections.[221,223,248,249] They are more susceptible to IAV infections compared to WT mice.[216]

Transgenic SPC-GM mice are characterized by a global GM-CSF knockout but overexpression of GM-CSF in SPC-positive cells, like AECIIs and BASCs, causing elevated GM-CSF levels only in the lung but not in blood.[250] SPC-GM mice were generated from Csf2-/- mice by insertion of a chimeric gene consisting of the GM-CSF sequence controlled by the human SPC promoter.[250] The abnormal accumulation of phospholipids and proteins in the alveolar region due to dysfunctional AMs is corrected in SPC-GM mice even though a few aggregations of enlarged, multinucleated AMs were found.[250] In SPC-GM mice, lung size is 30-40% larger than in mice not expressing the transgene (Csf2-/-).[221,251] This morphology is affiliated with increased AECII and AM proliferation and hence, cell numbers.[221,251] No gross abnormalities in hematology were observed in SPC-GM mice.[221,251] Upon IAV infection with the same lethal virus dose, their survival rate is increased compared to WT mice.[216]

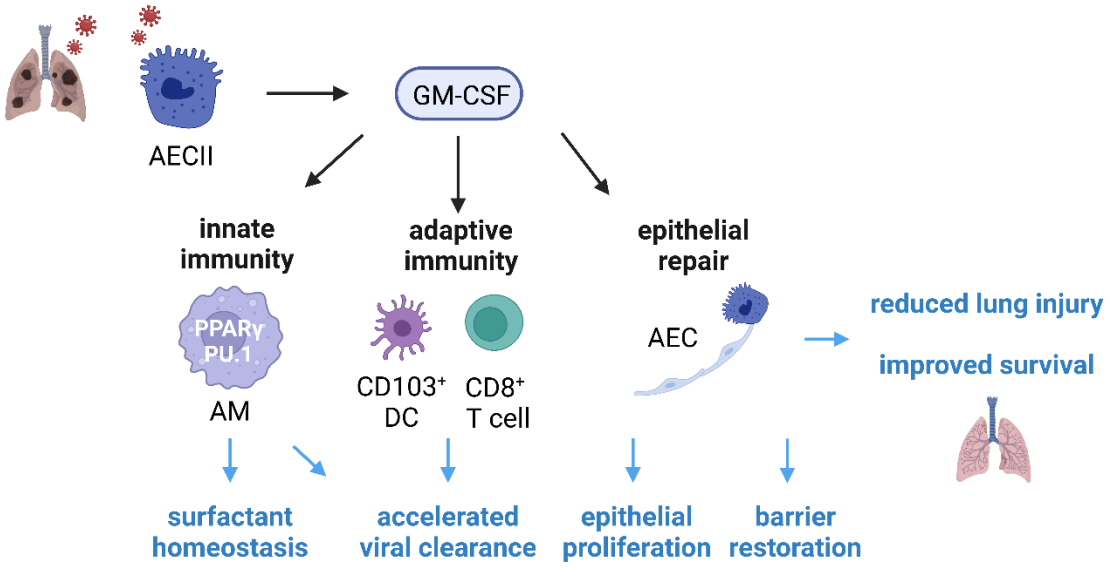

Figure 1.5: GM-CSF facilitates lung regeneration following IAV infection by enhancing both innate and adaptive immune functions and promoting epithelial repair. During IAV infection, GM-CSF expression is upregulated in AECIIs. GM-CSF enhances AM activity, which is crucial for surfactant homeostasis, and activates CD103⁺ DCs, which are essential for the effective recruitment of CD8⁺ T cells and accelerated viral clearance. Additionally, GM-CSF influences AECs in an autocrine mechanism, promoting epithelial repair and thereby improving the survival of ARDS patients. Adapted from Rösler & Herold et al. (2016).[201] Created with BioRender.

2 Aims of the study

Previous studies demonstrated that GM-CSF has a protective effect against IAV infection.[201] However, the specific mechanisms behind GM-CSF-induced alveolar regeneration remain unclear. This study aimed to characterize how GM-CSF facilitates alveolar epithelial repair and elucidate the molecular mechanisms mediated by GM-CSF in distal lung epithelial stem cells.

1) Characterizing the compartment of the distal lung in which GM-CSF is expressed during the course of IAV infection. Evaluating its effects on the proliferation and apoptosis of distal epithelial stem cells and how this affects repair of the alveolar epithelial barrier upon IAV-induced damage.

2) Investigating the influence of GM-CSF on the development of BALOs. Determining how GM-CSF and the regulation of the GM-CSF-mediated signaling pathway influence the ability of BASCs and AECIIs for organoid formation and evaluating the impact on alveolarization in the BALO model.

3) Investigating GM-CSF-induced alterations in the gene expression profiles of BASCs in response to IAV infection. Based on these findings, the GM-CSF-mediated signaling pathways in distal epithelial stem cells that contribute to enhanced lung repair were identified.

3 Methods

3.1 Mouse strains

8-12 weeks old C57BL/6 (abbreviated as WT) mice were purchased from Charles River Laboratories. GM-CSF deficient (Csf2-/-) [B6.129S-Csf2^{tm1Mlg}][247], GM-CSF receptor β-deficient (Csf2rb-/-) [B6.129S1-Csf2rb^{tm1Cgb}] knock-out mouse strains, and transgenic SPC-GM [B6.129S1-csf2$^{tm1mlg(SPC\text{-}GM\text{-}CSF)}$][250] mice were bred in the animal facility at Justus-Liebig University Giessen. SPC-GM mice were received as a gift from Dr. Jeffrey Whitsett (University of Cincinnati, OH).

All mouse strains were housed and treated under specific-pathogen-free (SPF) conditions. All animal experiments were performed at Justus-Liebig University Giessen and were approved by the responsible animal ethics committee and by the local authorities by the state of Hesse (Regierungspräsidium Giessen).

During infection experiments, mice were monitored 1-3 times per day according to the scoring guidelines. The scoring was based on loss of body weight, general health (condition of eyes, fur, and orifices), spontaneous behavior as well as experiment-specific criteria (breath frequency and chest breathing). For each measurement or observation, a specific score value was assigned (see table 3.1). Depending on the sum of score values, each mouse was categorized into a level of stress: no burden (0), low (5-9), medium (10-19), or high (≥20) stress. According to the level of stress, specific measures were implemented. The mouse was monitored two times per day under mild stress and three times per day under medium stress. Moreover, soaked food was provided. Under high stress, the mouse was monitored every 4-6 hours. However, if a high-stress condition lasted for more than 24 hours or a medium-stress condition for more than 5 days, the mouse had to be euthanized.

score	Classification of Criteria
0	- No change in body weight or increase - Shining fur, clean and open eyes, clean orifices - Attentive and quick behavior
5	- Matte fur, dull eyes - Unusual behavior, restricted movement or hyperactivity, reduced exploration behavior - Quick and visible breathing
10	- > 10% reduction of initial body weight - Blunt fur, dull eyes, unclean orifices - Isolation, coordination disturbances, sterotypic or hyperkinetic behavior, lethargy - Exsiccosis (> 4 sec)
15	- > 20% reduction of initial body weight
20	- > 25% reduction of initial body weight - Ruffled fur, closed eyes, convulsions, paralysis, breathing sound - Automutilation, necrosis, rectal prolapse - Chest breathing with reduced breath frequency, apathy, immobility, strong exsiccosis (> 4 sec and sunken bulbs), blue mucous membranes, visible shortness of breath, gasping respiration

Table 3.1: Definition of score values.

3.2 Human material

Human lung tissue samples were obtained from patients who underwent lobectomy after informed written consent at Justus-Liebig-University Giessen. The approval for the use of human lung tissue samples from the biobank (AZ 10/06, amendment to proposal 31/93) was given in the context of the research centre SFB 1021 by the Ethics Committee of Justus-Liebig University Giessen (June 2016 and December 2020).

3.3 Cell line culture

MDCK II cells (Madin-Darby canine kidney cells) were cultured in cell culture flasks at 37°C and 5% CO_2 in MDCK growth medium (see Materials 9.2.4). For passage, the cell layer was washed with PBS-/- and EDTA-Trypsin was added to detach and singularize the cells. The cells were passaged two times per week in a ratio of 1:30. For experiments, the cells were passaged 24 h before the treatment and seeded on a 96-well cell culture plate in a 1:3 ratio to reach 85-90% confluency the following day.

MRC-5 cells (Medical Research Council cell strain 5), a human fibroblast cell line from fetal lung tissue, were cultured in flasks at 37°C and 5% CO_2 in Eagle's Minimum Essential Medium with 10% fetal calf serum (see Materials 9.2.4). For passage, the cell layer was briefly rinsed with Trypsin-EDTA which was then added for 5 to 15 min until the cells were detached and singularized. The MRC-5 cells were split 1 to 2 times per week in a ratio of 1:2 to 1:5.

3.4 Primary human alveolar epithelial cells

3.4.1 Handling of primary human alveolar epithelial cells from company

Primary human alveolar epithelial cells (hAEC) were obtained from Cell Biologics and handled according to the manufacturer's instructions. Cell Biologics' primary hAECs were isolated from normal human lung tissue. To isolate the cells, they were incubated with an EpCAM-1 (CD326) antibody, followed by the introduction of magnetic beads coated with a secondary antibody. The primary hAECs were assessed for the expression of markers such as E-cadherin or ZO-1 using immunofluorescence staining. Prior to shipping, the cells were cryopreserved at passage 3.[252]

The thawed primary hAECs were cultured in Complete Human Epithelial Cell Medium (Cell Biologics) in cell culture flasks pre-coated with a gelatin-based coating solution (Cell Biologics). The primary hAECs were propagated for up to 3-6 passages. For passage, the cell layer was washed with prewarmed PBS-/-, followed by incubation with 0.25% Trypsin-EDTA solution for 3-6 min at 37°C. As soon as the cells were detached, 8-10 ml of Complete Human Epithelial Cell Medium (Cell Biologics) supplemented with 10% FCS was added and the cells were plated in fresh flasks or plates pre-coated with the gelatin-based coating solution (Cell Biologics). The cells were split in a ratio of 1:2 and the culture medium was changed every 24-48 hours depending on cell confluency.

3.4.2 Isolation of primary human alveolar epithelial cells

Lung tissue samples were dissected with forceps and scissors, washed with human AEC medium (see Materials 9.2.4), and filtered through a 100 µm cell filter. The cells were further digested by 2.5% dispase II in 2 mM calcium and 1.3 mM magnesium for 180 min at 37 °C and filtered through 100, 40, and 20 µm cell filters. After centrifugation at 1,500 rpm for 25 min at 20°C, the cells were segregated by Ficoll density centrifugation at 2,500 rpm for 15 min at room temperature (RT). The interphase was collected, washed, and resuspended in human AEC medium. For depletion of leukocytes, anti-human CD45 magnetic beads were added according to the manufacturer's instructions and incubated for 15 min at 4°C, followed by magnetic separation. To assess the purity of the isolated human AEC, flow cytometry was used (usually 90-98% epithelial cells). Trypan blue staining was utilized to determine cell

viability (>95%). Human AECs were plated at a density of 300-450,000 cells/cm^2 and grown for 5-6 days until 85-90% confluency before further treatment.

3.5 Isolation of primary murine alveolar epithelial cells

The AEC isolation was based on a modified protocol published by Herold *et al.* (2006).[253] For organ taking, mice were anesthetized by isoflurane inhalation and sacrificed by cervical dislocation. The chest cavity was opened and the mouse lungs were perfused with 25 ml sterile HBSS via the right ventricle. The trachea was punctured and a shortened 21-gauge cannula was inserted and fixed. The lungs were then filled with 1.5 ml dispase followed by 0.5 ml prewarmed low-melting-point agarose (1% in PBS-/-) to allow enzymatic digestion of distal but not proximal epithelial cells. If the murine alveolar epithelial cells (mAEC) were used for flow cytometry, no low-melting-point agarose was administered. After the agarose had solidified at RT, the lung and trachea were taken out of the chest cavity and placed in 1.5 ml dispase for 45 min at RT. After removal of the heart, thymus, and larger airways, the lung lobes were transferred into gentleMACS C tubes (Milteny Biotec) filled with DMEM/2.5% HEPES medium containing 0.01% DNase (5mg/ml). Lung homogenization was done using the gentleMACS Dissociator (Milteny Biotec). The lung homogenate was incubated for 8 min at RT and filtered through 100 and 40 µm nylon filters. After the cells were centrifuged at 500 g for 10 min at 4°C, the supernatant was removed and stored. The cell pellet was resuspended in 1 ml lysing buffer for red blood cells. After incubation for 120 sec under constant shaking, 6-8 ml DMEM/10% FCS was added to stop the cell lysis. The cell suspension and the supernatant were centrifuged at 500 g for 10 min at 4°C. The cell pellets were combined by resuspension in 10 ml DMEM/2.5% HEPES per lung. 10 µl of the cells were stained with DAPI and put on a chamber slide for the NucleoCounter (ChemoMetec) to determine the total cell number. With the ascertained cell numbers, the required volumes of biotin-labeled antibodies (see table 3.2), magnetic beads, and DMEM/2.5% HEPES medium were calculated for the depletion of endothelial cells and leukocytes.

Target of Biotin-labeled Antibody	Volume of Antibodies (µl)
CD45	Cell no. / 1,000,000 * 0.9
CD16/32	Cell no. / 1,000,000 * 0.675
CD31	Cell no. / 1,000,000 * 0.4

Table 3.2: Formulas to determine the volumes of biotin-labeled antibodies for cell depletion. When the cells were prepared for flow cytometry, the antibody volumes were reduced by 10%.

$$\text{Volume magnetic beads (µl)} = \frac{\text{Cell no.}/1{,}000{,}000 * 0.65}{3}$$

Volume DMEM/2.5% HEPES medium (ml)= Volume magnetic beads (µl) * 50

The biotin-labeled antibodies were added to the cell suspension and incubated for 30 min at 37°C. The cells were centrifuged at 500 g for 10 min at 4°C and resuspended in the calculated volumes of DMEM/2.5% HEPES medium and streptavidin-linked magnetic beads (washed three times with PBS-/-). After incubation for 30 min at RT under constant rotation, the magnetic separation was performed for 15 min by placing the cell suspension on the MPC™-6 (Magnetic Particle Concentrator, ThermoFisher). The supernatant containing the isolated mAECs was harvested and either used for FACS staining or for mAEC culture. For the later, 150,000-200,000 mAECs/cm^2 were seeded on 6-well cell culture plates and incubated at 37°C and 5% CO_2 for 4 days to reach 85-90% confluency.

3.6 Fluorescence-activated cell sorting (FACS)

3.6.1 Analysis of Ki67$^+$ and AnnexinV$^+$ AECIIs and BASCs

Protein expression was measured in multicolor flow cytometry using LSR Fortessa with DIVA software (BD Bioscience). After determining the cell number in the lung homogenate, the cells were washed in FACS buffer once and distributed on a U-bottom 96-well plate with 1-2*10^6 cells per well. The cells were centrifuged at 1,000 g for 3 min at 4°C, the supernatant was discarded, and the cells were resuspended in 50 µl extracellular staining solution per well (see tables 3.3 and 3.4).

Antibody		Dilution
Anti-CD31/45	FITC	1:50
Anti-CD326	APC-eFluor780	1:50
Anti-Sca-1	APC	1:50
Anti-CD24	PacificBlue	1:200

Table 3.3: Extracellular staining for the analysis of Ki67 protein.

Antibody		Dilution
Anti-CD31/45	FITC	1:50
Anti-CD326	APC-eFluor780	1:50
Anti-Sca-1	APC	1:50
Anti-CD24	PE-Cy7	1:200

Table 3.4: Extracellular staining for the analysis of AnnexinV$^+$ cells.

After incubation for 15 min at 4°C in the dark, the cells were centrifuged at 1,000 g for 3 min at 4°C and the supernatant was discarded.

3.6.1.1 Ki67 staining

The Foxp3/Transcription Factor Staining Buffer Set (ThermoFisher) was used for staining the nuclear protein Ki67. The permeabilization/fixation buffer was prepared by diluting the fix/perm concentrate in the fix/perm diluent in a ratio of 1:3. The cells were resuspended in 150 µl permeabilization/fixation buffer per well and incubated for 30 min at RT. 1x permeabilization/wash buffer diluted in ddH_2O was added (100 µl/well) and the cells were centrifuged at 1000 g for 3 min at 4°C. The supernatant was discarded, and the cells were resuspended in 50 µl FACS buffer per well containing the anti-Ki67 PE antibody or the corresponding isotype control (see table 3.5).

Antibody		Dilution
Anti-Ki67	PE	1:50
IgG2a kappa isotype	PE	1:50

Table 3.5: Antibody dilutions for Ki67 staining.

After incubation for 1 h at 4°C in the dark, 150 µl 1x permeabilization/wash buffer per well was added and the cells were centrifuged at 1,000 g for 3 min at 4°C. The supernatant was discarded, the cells were resuspended in FACS buffer, and filtered through a 40 µm cell strainer cap into a FACS tube for the measurement.

3.6.1.2 AnnexinV staining

During the staining procedure, reactives and samples were kept on ice. Pacific Blue-labeled AnnexinV (ThermoFisher) was diluted 1:20 in Annexin Binding Buffer prepared in a 1:5 dilution of Annexin Binding Buffer (5X) concentrate (Thermo Fisher) with ddH_2O. 100 µl of the AnnexinV staining solution plus 10 µl Sandoglobulin® were added per well. For the negative control, the cells were resuspended in 100 µl AnnexinV Binding Buffer without Pacific Blue-labeled AnnexinV. After an incubation time of 15-25 min at 4°C in the dark, the cells were transferred through a cell strainer cap into a FACS tube, and the measurement was done immediately.

3.6.2 Cell sorting

FACS sorting was done either to isolate AECI, AECII and BASC populations for qPCR or Western Blot analysis or to isolate epithelial and mesenchymal stem cells for organoid cultures. BD FACS Aria™ III cell sorter with DIVA software (BD Bioscience) was utilized for cell sorting using an 85 µm nozzle.

3.6.2.1 Sort of AECIs and AECIIs for qPCR analysis

After the isolation of mAECs (see Methods 3.5), the cells were washed in MACS buffer once. Hereafter, the cells were centrifuged for 10 min at 500 g and 4°C, the supernatant was taken and kept for the negative control. Then the cell pellet was resuspended in 100 µl staining solution per lung that contained the immunofluorescence-labeled antibodies for the cell surface staining (see table 3.6) diluted in MACS buffer plus 10% gammaglobulins (Sandoglobulin®) for blocking.

Antibody		Dilution
Anti-CD45	FITC	1:50
Anti-CD31	FITC	1:50
Anti-CD365 (EpCAM)	APC-Cy7	1:50
Anti-T1α	APC	1:50

Table 3.6: Fluorescence-labeled antibodies for the sort of living AECIs and AECIIs for qPCR.

The mAECs were incubated with the staining solution for 15 min at 4°C. After centrifugation at 500 g for 10 min at 4°C, the mAECs were transferred into a FACS tube by passing through a cell strainer cap. Immediately before the FACS sort, Sytox™ Blue (ThermoFisher) was added to the cell suspension in a 1:1,000 dilution for the distinction of live and dead cells.

3.6.2.2 Sort of AECIIs and BASCs for qPCR or Western Blot analysis

Following the isolation of mAECs (see Methods 3.5), the cells were resuspended in PE-labeled Lysotracker diluted 1:10,000 in DMEM/10% FCS. After an incubation of 30 min at 37 °C and 5% CO_2, the cells were centrifuged at 500 g for 10 min at 4°C and washed in MACS buffer. The mAECs were resuspended in 100 µl MACS buffer per lung containing the diluted fluorescence-labeled antibodies (see table 3.7) plus 10% gammaglobulins (Sandoglobulin®) for blocking.

Antibody		Dilution
Anti-CD45	FITC	1:50
Anti-CD31	FITC	1:50
Anti-CD365 (EpCAM)	APC-Cy7	1:50
Anti-CD24	PE-Cy7	1:200
Anti-Ly6c (Sca-1)	APC	1:50

Table 3.7: Fluorescence-labeled antibodies for the sort of living AECIIs and BASCs for qPCR.

The cells were incubated with the antibody mix for 15 min at 4°C in the dark. After centrifugation at 500 g for 10 min at 4°C, the cells were transferred through a cell strainer cap into the FACS tube, and immediately before cell sorting Sytox™ Blue (ThermoFisher) was added for the distinction of live and dead cells (1 µl Sytox™ Blue per ml cell suspension).

3.6.2.3 Sort of epithelial and mesenchymal stem cells for organoid culture

The isolated mAECs were washed in MACS buffer once. The cells were centrifuged at 500 g for 10 min at 4 °C, the supernatant was removed and kept for negative control. The cell pellet was resuspended in MACS buffer (100 µl/lung) containing the antibodies for staining (see table 3.8) plus 10% Sandoglobulin® for blocking.

Antibody		Dilution
Anti-CD45	FITC	1:50
Anti-CD31	FITC	1:50
Anti-CD365 (EpCAM)	APC-Cy7	1:50
Anti-CD24	PE-Cy7	1:200
Anti-Ly6c (Sca-1)	Pacific Blue	1:50

Table 3.8: Fluorescence-labeled antibodies for the sort of rMCs, AECs, and BASCs.

After incubation for 15 min at 4°C, the cells were centrifuged at 500 g for 10 min at 4°C and resuspended in 1 ml MACS buffer per lung. The cell suspension was filled into a FACS tube through a 40 µm mesh for cell sorting. rMC, BASC, and AECII enriched populations were sorted for organoid cultures.

3.7 *In Vitro* experiments

3.7.1 Murine organoid cultures

Lung organoid cultures were prepared as described previously by Vazquez-Armendariz et al. (2020)[184]. Flow-sorted rMCs (EpCAM^{-}Sca-1^{+}) and BASCs (EpCAM^{high}CD24^{low}Sca-1^{+}) or AECIIs (EpCAM^{low}) were centrifuged at 500 g for 10 min at 4°C. The supernatants were removed, and the cells were resuspended in mouse organoid medium (see Materials 9.2.4). For co-cultivation, the cell concentration was adjusted to 15,000-20,000 rMCs and 5,000 BASCs per 50 µl medium per 12 mm cell culture insert (Millipore). For alveolosphere cultures, 15,000-20,000 rMCs and 40,000 AECs were applied per insert. The cells were mixed with cold growth factor reduced Matrigel® (Corning) in a 1:1 ratio as described before[42] and incubated for 10 minutes at 37°C and 5% CO_2 for Matrigel polymerization. 350 µl mouse organoid medium per well was added and changed three times per week. Organoids were treated with AMPK activator AICAR (0.5 mM), AMPK inhibitor Compound C (1 µM), mTORC1 activator MHY1485 (1 µM), mTORC1 inhibitor Rapamycin (0.5 nM) (Merck), or recombinant murine GM-CSF (50 or 100 pg/ml) (R&D Systems).

3.7.2 Human alveolosphere cultures

Human alveolosphere cultures were prepared as further described.[254] The 85-90% confluent cell layers of primary hAECs and MRC-5 cells were washed 1-2 times with PBS-/- and EDTA-Trypsin was added to detach and singularize the cells. They were resuspended in human alveolosphere medium consisting of Small Airway Epithelial Cell Growth Medium (SAGM^{TM}) supplemented with 1% Penicillin (100 U/ml) / Streptomycin (10 mg/ml) and 5% FCS. 25 µl human alveolospheres medium containing 5,000 primary hAECs and 30,000 MRC-5 cells were mixed with 50 µl cold growth factor reduced Matrigel® (Corning) and applied to one 12 mm cell culture insert (Millipore). After incubation for 10 minutes at 37°C and 5% CO_2, 350 µl SAGM containing 10 µM ROCK inhibitor (STEMCELL Technologies) was added. After 48 h, it was replaced by SAGM without ROCK inhibitor. The human alveolospheres were treated with AMPK activator AICAR (0.5 mM) or AMPK inhibitor Compound C (1 µM) (Merck) from day 21 to 28 of culture.

3.7.3 Infection of primary human and murine alveolar epithelial cells

For IAV infection, the virus strain A/Puerto Rico/8/34 (PR8, H1N1) was utilized, a mouse-adapted laboratory strain of IAV that was propagated on canine epithelial MDCK II cells.[255] Primary human and murine AECs were infected with PR8 IAV with a multiplicity of infection (MOI) 0.1. On the day of infection, the confluency of the primary AECs was assessed to be between 85-95% using the BX41 light microscope (Olympus, Germany). The cell layer was washed with PBS+/+ and the virus diluted in 0.2% bovine serum albumin (BSA) in PBS+/+ was added to the cells. After incubation for 45 min at 37°C and 5% CO_2 under regular movement, the inoculum was removed and the cells were washed with PBS+/+ before the infection medium for human or murine AECs was added (see Materials 9.2.4). Depending on the experimental plan, human (100 ng/ml) or murine (50 ng/ml) recombinant GM-CSF (R&D Systems) was added to the infection medium. To analyze the activation state of AMPK and mTOR, murine AECs were lysed at 24 h post-infection in NP40 cell lysis buffer for Western Blot analysis. Human AECs were lysed at 30 or 45 min after infection.

3.7.4 SDS-PAGE and Western Blot

Western Blot was utilized to analyze quantitative differences in protein abundance in primary human or murine AECs in IAV-infected or PBS-treated conditions and upon GM-CSF treatment. Moreover, murine AECIIs isolated by FACS were applied for Western Blot analysis. NP40 cell lysis buffer (see Materials 9.2.4) was mixed with protease and phosphatase inhibitor cocktails before use. The cell lysates were placed on ice and incubated for 20 minutes with regular mixing. Following centrifugation at 8,000 rpm for 10 minutes at 4°C, the protein-containing supernatant was collected. To determine the protein concentration the Dc Protein Assay (Bio-Rad) was used according to the manufacturer's instructions. Colorimetric measurement was performed using a 96-well microplate reader (Bio-Rad) measuring the adsorption at a wavelength of 595 nm. 18-25 µg protein sample was prepared for SDS-PAGE by mixing with 5x Western Blot loading buffer (see Materials 9.2.4) and heating at 95°C for 10 min. The sample was briefly cooled down on ice, centrifuged, and then applied to a 2-14% precast TGX mini gel (Bio-Rad). 1x Tris/Glycine/SDS buffer from Bio-Rad was used as an electrophoresis buffer. Polyacrylamide gel electrophoresis (PAGE) was performed at 90-100 V and 40 mA for 90 min under denaturing and reducing conditions. Afterward, the proteins were transferred to a 0.2 µm PVDF membrane

using the Trans-Blot Turbo Transfer System (Bio-Rad). To block unspecific epitopes, the membrane was incubated in 5% milk powder dissolved in 0.2% Tween-20 in PBS-/- for 1 h at RT or overnight at 4°C. The antibodies were diluted in 2% milk powder dissolved in 0.2% Tween-20 in PBS-/-. The primary antibody was incubated for 1 h at RT or over night at 4°C on the laboratory shaker, then washed three times for 5 min with 0.2% Tween-20 in PBS-/- and the secondary HRP-linked antibody was added. For visualization, the chemiluminescence reaction of HRP with luminol was used and detected with the ChemiDoc imaging system (Bio-Rad). Image Lab software (Bio-Rad) was utilized for the quantification of bands that were related to an internal GAPDH control.

3.7.5 Influenza A virus titration

On the day before infection, MDCK II cells were seeded in a ratio of 1:3 on a 96-well plate, to reach a density of 85–90% the following day. Virus titration in BALF was done in triplicates. A 1:10 dilution series of the BALF with eight steps was performed ranging from $1:10^1$ to $1:10^8$. MDCK II cells were washed with 150 µl PBS+/+ twice before 50 µl virus inoculum per well was added. After incubation at 37°C for 40 min, the inoculum was removed, and the cell layer was covered with 100 µl Avicel® overlay medium (see Materials 9.2.4). The high viscosity of the Avicel®-containing overlay medium prevents the virus from widespread and only direct cell-to-cell infections are possible leading to plaque formation. After incubation for 24-36 h at 37°C and 5% CO_2, the overlay medium was removed, and the cells were washed with PBS-/-. The cells were incubated with 4% PFA for 20 min at 4°C for fixation followed by permeabilization with 0.3% Triton-x-100 in PBS-/- for 15 min at RT. Afterward, the cells were blocked with normal horse serum (NHS) diluted 1:100 in PBS/0.2% BSA for 30 min at RT. The plaques were visualized by an immunohistochemistry staining of the nucleoprotein. The primary anti-nucleoprotein antibody was diluted 1:100 in 10% NHS and 0.05% Tween80 in PBS-/- and incubated for 1h at RT followed by the 1:1,000 diluted secondary horseradish peroxidase (HRP)-linked anti-mouse antibody. After three washing steps with 0.05% Tween80 in PBS-/-, the KPL TrueBlue™ peroxidase substrate (seracase) was added to visualize the plaques. The plate was washed 2-3 times with distilled water and dried to count the plaques at the microscope and calculate the virus titer.

The following formula was used for the virus titer calculation:

virus titer = number of plaques per well * dilution^{-1} * 20

3.7.6 GM-CSF ELISA

To determine the GM-CSF concentration in cell culture supernatants, the mouse Quantikine ELISA Kit from R&D Systems was used due to the manufacturer's instructions. The samples were stored at -80°C and applied undiluted in the ELISA. A GM-CSF standard curve was utilized to determine the GM-CSF concentrations in the samples. After the addition of a luminescent substrate, the adsorption at a wavelength of 450 nm was measured in a microplate reader (Bio-Rad).

3.8 *In vivo* experiments

3.8.1 Intratracheal application of IAV, AMPK activator, and AMPK inhibitor

For *in vivo* IAV infection, mice were anesthetized with isoflurane. The mice were fixed on the intubation table at their hind legs and upper teeth in a supine position. Then, the nose was placed inside the isoflurane mask to maintain anesthesia. An endotracheal tube was inserted through the vocal cords into the trachea and 70 µl PR8 virus inoculum was applied. The virus was diluted in PBS-/- to a titer of 500 FFU (foci forming units) per 70 µl for C57BL/6 mice. Csf2-/- mice were infected with 100 FFU and SPC-GM mice with 2,000 FFU diluted in 70 µl PBS-/-. Mice from PBS control groups were inoculated with 70 µl sterile PBS-/- without any additives.

To analyze the *in vivo* effect of the AMPK activator AICAR (CAS-No.: 2627-69-2, MedChemExpress) or AMPK inhibitor Compound C dihydrochloride (CAS-No: 1219168-18-9, MedChemExpress), they were injected intratracheally. AICAR was applied in a concentration of 500 µg/g bodyweight diluted in a total volume of 70 µl NaCl compared to 70 µl NaCl as a control. Compound C dihydrochloride was utilized in a concentration of 20 µg/g bodyweight diluted in PBS. 70 µl PBS was applied as a control.

3.8.2 Intravenous FITC albumin application

To measure alveolar barrier integrity, fluorescein Isothiocyanate (FITC)-labeled albumin was applied intravenously. Before treatment, mice were anesthetized with Xylazine hydrochloride (application 16 mg/kg; diluted in 0.09% sterile NaCl to 3.33 mg/ml) and Ketamine hydrochloride (application 100 mg/kg; diluted in 0.09% sterile NaCl plus 3.33 mg/ml Xylazine hydrochloride to a concentration of 25 mg/ml) applied intraperitoneally at 0.2 ml per 20 g body weight. Once the mice were anesthetized, 1 mg FITC albumin diluted in 100 µl NaCl was applied to the mouse's tail vein. After 45 min, the mice were sacrificed by cervical dislocation and the chest cavity was opened to take the blood from the *vena cava*. The trachea was punctured to insert and fix a shortened 21-gauge cannula. 1.2 ml PBS/EDTA in total was filled into the lungs in three steps (300, 400, and 500 µl) to obtain BALF. The BALF was centrifuged at 500 g for 10 min at 4°C and 100 µl of the supernatant was applied to a 96-well plate (Costar). The collected blood had to rest at RT in the dark for at least 2 h for complete blood coagulation. Afterward, the blood was centrifuged at 3,500 rpm for 10 min at RT. The supernatant was centrifuged again at 3,500 rpm for 4 min to

remove the remaining blood cells. The blood serum was diluted 1:10 in PBS-/- and 100 µl of it was applied to the 96-well plate. The fluorescence intensity of FITC at a wavelength of 525 nm was measured with the Plate-Reader FLX800 (Biotech). The alveolar leakage was determined by calculating the ratio of fluorescence in BALF to blood serum (alveolar leakage = fluorescence BALF / fluorescence blood serum). The alveolar barrier normal ratio is about 0.05, whereas the ratio rises when the alveolar barrier is damaged.

3.9 Analysis of gene expression

3.9.1 RNA isolation

Ribonucleic acid (RNA) was isolated using the RNeasy Micro Kit (Qiagen) according to the manufacturer's instructions. After isolation, the cells were centrifuged (500 g, 10 min, 4°C) and the pellet containing up to $5*10^5$ cells was lysed and homogenized in RLT buffer. The subsequent steps were automated using the QIAcube Connect system (Qiagen). One volume of 70% ethanol was added to the sample, and the mixture was transferred to an RNeasy MinElute spin column (Qiagen). Following centrifugation for 15 s at ≥ 8,000 g, the flow-through was discarded. Then, 350 µl of RW1 buffer was added to the spin column and centrifuged for 15 s at ≥ 8,000 g, with the flow-through discarded. Afterward, 80 µl of DNase incubation mix was added to the spin column and incubated for 15 min at room temperature. After incubation, 350 µl of RW1 buffer was added, and the spin column was centrifuged for 15 s at ≥ 8,000 g, with the flow-through and collection tube discarded. Next, 500 µl of RPE buffer was added to the spin column, and after centrifugation for 15 s at ≥ 8,000 g, the flow-through was discarded. Subsequently, 500 µl of 80% ethanol was added to the spin column, and after centrifugation for 2 min at ≥ 8,000 g, the flow-through was discarded. The spin column was then placed in a new collection tube and centrifuged for 5 min at full speed to dry the membrane. Finally, the spin column was transferred to a new collection tube, 14 µl of RNase-free water was added to the center of the spin column membrane, and the column was centrifuged for 1 min at full speed to elute the RNA.

The RNA concentration was measured by spectrophotometry using NanoDrop (ThermoFisher).

3.9.2 cDNA synthesis

For copy deoxyribonucleic acid (cDNA) synthesis, 250 ng of the isolated RNA was mixed with 1.5 µl random hexamers and 1 µl deoxyribonucleotide triphosphates (dNTP) due to the manufacturer's instructions. The RNA mixture was heated up at 65°C for 5 min to break RNA secondary structures and linearize the RNA. The sample was put on ice and 8 µl of the master mix containing the reverse transcriptase RT M-MLV was added (4 µl 5x first strand buffer, 2 µl DTT, 1 µl RNase out, 1 µl RT M-MLV). The following thermocycler program was used:

Temperature (°C)	Time
25	00:10:00
37	00:50:00
70	00:15:00
4	∞

Table 3.9: Thermocycler program for cDNA synthesis.

3.9.3 Quantitative real-time polymerase chain reaction (qRT-PCR)

qRT-PCR analysis was performed with the iTaq SybrGreen Mix (BioRad) and the AB Step one plus Detection System (Applied Bioscience) or the QuantStudio™ 3 Real-Time PCR System (ThermoFisher). The primer pairs were applied in a concentration of 200 nM and 1 µg cDNA was added per reaction. The following qPCR program was used:

Temperature (°C)	Time	
95	00:10:00	
95	00:00:15	} 40 cycles
60	00:01:00	

Table 3.10: Program for qPCR.

Primer specificity was validated by analyzing the melt curve plot. To test primer efficiency, a 1:2 cDNA dilution series was prepared for qPCR analysis. The resulting CT values (y-axis) and log dilutions (x-axis) were plotted and the slope was used to calculate amplification efficiency ($2^{(-1/slope)}$). Primer pairs with an efficiency between 95 and 105 were chosen. GAPDH or mRPS18 expression served as the normalization control. The following primer pairs were used to analyze gene expression in murine AECIIs:

GAPDH fwd 5'- CCC CCA TGT TTG TGA TGG GT -3'
rev 5'- TCT TCT GGG TGG CAG TGA TG -3'
mRPS18 fwd 5'- CCG CCA TGT CTC TAG TGA TCC -3'
rev 5'- TTG GTG AGG TCG ATG TCT GC -3'

GM-CSF	fwd	5'- GTC TCT AAC GAG TTC TCC TTC A -3'
	rev	5'- CCT TGA GTT TGG TGA AAT TGC C -3'
cMyc	fwd	5'- ACC ACC AGC AGC GAC TCT GA -3'
	rev	5'- TGG CAG GGG TTT GCC TCT TC -3'
Ccnd1	fwd	5'- CGT GGC CTC TAA GAT GAA GG -3'
	rev	5'- CTG GCA TTT TGG AGA GGA AG -3'

Primer pairs were designed with NCBI Primer-BLAST and purchased from metabion (Germany). Data are presented as ΔCt (Ct target – Ct reference) or fold change ($2^{-\Delta\Delta Ct}$).

3.9.4 Bulk RNA sequencing

BASCs were isolated from the lung homogenate of WT and Csf2-/- mice, IAV-infected or mock-treated, utilizing FACS. The RNA was isolated as previously described (see chapter 3.9.1). RNA sequencing was carried out by PD Dr. Torsten Hain from the Institute for Medical Microbiology at Justus-Liebig-University in Giessen, Germany.

The Invitrogen™ Qubit™ 3 Fluorometer and the Qubit™ RNA High Sensitivity (HS) Kit (Thermo Fisher Scientific Inc., Waltham, MA, USA) were employed to quantify the concentration of total RNA. Quality was subsequently evaluated using an RNA Nano 6000 Kit (Agilent, Santa Clara, CA, USA) in the Bioanalyzer 2100 instrument. Prior to library preparation with the Nextera® XT DNA Library Preparation Kit (Illumina, San Diego, CA, USA), the SMART-Seq® v4 Ultra® Low Input RNA Kit for Sequencing (Takara, Kusatsu, Shiga, JP) was applied to account for the low concentration of RNA. To facilitate multiplex sequencing, Nextera XT V2 Index Kit (Illumina, San Diego, CA, USA) was used. Libraries were further purified with Agencourt AMPure XP Reagent (Beckman Coulter, Pasadena, CA, USA), and quality and quantity of the amplified cDNA were assessed with a DNA High Sensitivity Kit (Agilent, Santa Clara, CA, USA). Following this, samples were pooled, denatured, and diluted to 1.8 nM. They were sequenced with 1% of PhiX Sequencing Control v3 on NextSeq 500/550 High Output Kit v2.5 (150 cycles or 300 cycles) reagents (Illumina, San Diego, CA, USA).

Per condition 4-5 biological replicates were analyzed and included in the final analysis, comprising principal component (PCA) and Kyoto Encyclopedia of Genes

and Genomes (KEGG) pathway analysis. In the KEGG pathway analysis, the top 20 pathways with differential gene expression were assessed. Genes were considered differentially expressed when the adjusted p-value was below 0.05 and the logarithmized fold change was above 1 or below −1.

3.10 Microscopy

3.10.1 Immunofluorescence staining of organoids

3.10.1.1 Organoid fixation

To fix the organoids, the mouse organoid medium was removed from the well, and the insert was washed with 500 µl PBS-/- once. The PBS-/- was removed and 500 µl 4% paraformaldehyde (PFA) was added. After incubation for 10-15 min at RT, the 4% PFA was discarded, and the insert was washed three times with 500 µl PBS-/-.

3.10.1.2 Immunofluorescence staining of organoids within Matrigel

The fixed organoids were permeabilized and blocked with 500 µl of perm/block buffer (5% serum and 0.5% Triton-X-100 in PBS-/-) overnight at 4°C. The serum was chosen from the same species as the host of the secondary antibody. Primary and secondary antibodies were diluted in perm/block buffer and incubated overnight at 4°C. For DAPI staining, NucBlue™ Fixed Cell ReadyProbes™ Reagent (Thermo Fisher) was utilized. The insert was washed three times with 500 µl washing buffer (2% serum and 0.3% Triton-X-100 in PBS-/-) for 10-15 minutes and afterward, the Matrigel containing the organoids was cut out of the insert with a scalpel. The sample was placed on an object slide and covered with 3-4 drops of the mounting medium (ProLong™ Diamond Antifade Mountant, ThermoFisher). A coverslip was placed on the sample and after drying for 1-2 days at RT in the dark, the imaging was done at a confocal microscope.

3.10.1.3 Immunofluorescence staining of organoids with Matrigel removal

To analyze the signal intensity of an organoid immunofluorescence staining, the Matrigel® (Corning) was removed. The described protocol is based on a publication by C. Pleguezuelos-Manzano *et al.* (2020).[256] The fixed organoids were collected with a pre-coated 1 ml pipette tip that has a cut end in 1 ml Cell Recovery Solution (Corning) and transferred into a 1.5 ml microtube pre-coated with FCS. After incubation for 30 min under regular inversion, the organoids were centrifuged at 300 g for 3 min at RT and the SN was removed. 1 ml permeabilization solution (0.5% Triton-X-100 and 2% donkey serum in PBS-/-) was added and incubated under constant rolling for 30 min at 4°C. After centrifugation at 300 g for 3 min at RT, the supernatant was removed, 1 ml blocking solution (0.1% Tween-20 and 2% donkey serum in PBS-/-) was added and incubated for 15 min at RT under constant rolling. After centrifugation at 300 g for 3 min at RT, the SN was removed, and the primary

antibodies diluted in blocking solution were added to the organoids. After incubation at 4°C overnight under constant rolling, the organoids were centrifuged and the SN was removed. Then, the organoids were washed 3 times with PBS-/- each 10 min at RT under constant rolling. The secondary antibodies and NucBlue™ Fixed Cell ReadyProbes™ Reagent (Thermo Fisher) for DAPI staining were diluted in blocking solution and added to the organoids for incubation at 4°C overnight under constant rolling. After centrifugation at 300 g for 3 min at RT, the SN was removed and the organoids were washed three times with PBS-/- as previously described, followed by an additional washing step with water. Then, the organoids were resuspended in 50 µl mounting medium (ProLong™ Diamond Antifade Mountant, ThermoFisher) utilizing a 200 µl pipette tip pre-coated with FCS and with a cut tip. The sample was transferred to a microscope slide and mounted with a coverslip. After drying the sample for 1-2 days at RT in the dark, the imaging was performed at a confocal microscope.

3.10.2 Preparation of lung sections for histology

3.10.2.1 Preparation of lung tissue for paraffin sections

For the preparation of paraffin sections from mouse lung tissue, lungs were clipped at the trachea before the chest cavity was opened. Then the lungs were perfused with 25 ml HBSS, removed, and fixed for 24 h in 4% PFA at 4 °C. Lungs were embedded in Paraffin (Leica ASP200S), and cut into 3-5 µm thick sections that were stained with H&E or immunofluorescence antibodies for lung histological analysis.

3.10.2.2 Hematoxylin and eosin (H&E) staining

Paraffin sections were stained with H&E in the following procedure: Xylene 5 min (twice), 100% ethanol 30 sec (twice), 96% ethanol 30 sec (twice), 70% ethanol 30 sec (twice), hematoxylin 3 min, 0.1% HCl 2 sec, H_2O 5 min, Eosin G solution 3 min, H_2O 30 sec, 70% ethanol 30 sec, 90% ethanol 30 sec, 100% ethanol 30 sec (twice), xylene 5min (twice).

3.10.2.3 Immunofluorescence staining of paraffin lung sections

The paraffin-embedded lung tissue sections were first deparaffinized by incubating them two times for 3 min each in Neo-Clear™ (Sigma-Aldrich). Following deparaffinization, the sections were rehydrated by sequential washes in an ethanol series: 2x for 3 min in 100% ethanol, 1x for 3 min in 95% ethanol, 1x for 3 min in 80% ethanol, 1x for 3 min in 70% ethanol, and 1x for 3 min in 50% ethanol. Finally, the

sections were washed twice for 3 min each in distilled water to remove residual ethanol. For antigen retrieval, the sections were incubated in a preheated antigen retrieval buffer (Citrate Buffer pH 6.0, ThermoFisher) at 95°C for 20 min. Afterward, the sections were allowed to cool in the buffer for 20 min at RT. The sections were then removed from the antigen retrieval solution and washed three times for 3 min each in distilled water. To permeabilize the tissues, the sections were briefly washed in PBS-/- for 1 min and then incubated in permeabilization buffer (0.5% Triton X-100 in PBS-/-) for 20 min at RT. Following permeabilization, the sections were washed once in PBS-/- for 3 min. Blocking was performed by incubating the sections in blocking buffer (10% NHS, 1% BSA in PBS-/-) for 1 h at RT to reduce nonspecific antibody binding. The sections were then washed once in PBS-/- for 3 min before being incubated with the primary antibodies diluted in the blocking buffer. The sections were incubated overnight with the primary antibodies at 4°C. On the following day, the sections were washed three times for 3 min each in PBS-/-. Secondary antibodies and DAPI (NucBlue™ Fixed Cell ReadyProbes™ Reagent, Thermo Fisher), both diluted in blocking buffer, were then added to the sections and incubated for 1 h at RT. After the incubation, the sections were washed three times for 3 min each in PBS-/- and once briefly in distilled water at RT. Excess water was removed, and three drops of mounting medium (ProLong™ Diamond Antifade Mountant, ThermoFisher) were applied to the slides. Coverslips were placed on top, and the sections were dried overnight at RT before imaging using a confocal microscope.

3.10.3 Microscopes and image analysis

For confocal imaging, the Leica SP8 CLSM system (Leica Microsystems, Germany) running on LAS X 3.5.7 software was utilized, equipped with a 405 nm and a white light laser (WLL). For the excitation of DAPI, Alexa Fluor 488 and Alexa Fluor 647, the 405 nm laser as well as the 499 nm and 653 nm laser lines from the WLL respectively were used. Upon a line-by-line sequential scan, all emissions were captured with 3 different hybrid detectors (HyD). In all cases, a 20x/0.75NA air objective with a voxel size of 0.28x0.28x1 µm was utilized while the pinhole was set at 1 A.U. Z-stack images were acquired with a z-step size of 1 µm. The confocal images were acquired and analyzed in cooperation with Ioannis Alexopoulos, Multiscale Imaging Platform, Institute for Lung Health, JLU Giessen.

All acquisitions were computationally cleared using the Lightning module of LAS X software with the default settings. These cleared acquisitions were used further for quantification with custom-made macros of Fiji software following the steps below.

- For each acquired z-stack, a maximum intensity projection for all channels was generated.
- This projection was further filtered using the median filter of FIJI with a radius of 1.5 pixels.
- With the user's input, each organoid was delineated using the polygon selection tool. Each organoid's projected area was measured in μm^2 from this selection.
- The ProSPC$^+$ area was measured in μm^2 within the user's selection upon removal of the background signal using the Li threshold algorithm and then normalized by the organoid area to calculate the ProSPC$^+$ area ratio.
- The same approach was followed for all extra markers of which the area ratios were calculated.

For the measurement of the phospho-protein (phospho-ACC or phospho-mTOR) mean intensity within the ProSPC$^+$ area the following steps were done in addition:

Upon thresholding out the background signal of the respective channels, we multiplied a binary (0,1) version of the mask of the ProSPC channel with the phospho-protein channel. From the resulting image, the area of the phospho-protein$^+$ signal within the ProSPC$^+$ area was measured, as well as its mean intensity.

Bright-field images of the organoids were acquired on the EVOS™ FL Auto Imaging System (Thermo Scientific). Tiled images of the organoid cultures were acquired with the 10x objective.

3.11 Statistics

Normally distributed data are given as mean ± standard error of the mean (SEM). To analyze the statistical significance between two groups, an unpaired Student's t-test was used. For three or more groups ANOVA was utilized. To test whether the residuals are Gaussian, the following normality tests were applied: Anderson-Darling, D'Agostino, Shapiro-Wilk, and Kolmogorov-Smirnov. For non-normally distributed data, the median and interquartile ranges are shown and statistical differences between two groups were determined utilizing the Mann-Whitney test. GraphPad Prism 9 was applied for statistical analysis and preparation of the graphs. A p-value less than 0.05 was considered significant, *$p<0.05$; **$p<0.01$; ***$p<0.005$, ****=$p<0.0001$.

4 Results

4.1 GM-CSF expression is upregulated in AECIIs and BASCs after IAV infection

During IAV infection, there is a significant upregulation of GM-CSF expression in AECIIs, which promotes epithelial repair in an autocrine manner by stimulating epithelial proliferation and facilitating restoration of the alveolar epithelial barrier.[201] In one of our previous studies conducted by Unkel et al. (2012), the GM-CSF-driven cross-talk between CD103$^+$ DCs and AECs following IAV infection was investigated.[216] As part of this study, the expression of GM-CSF in the distal lung during IAV infection was examined.[216] Apart from CD45$^+$ leukocytes, there was a significant increase in GM-CSF expression observed in AECIIs in the lung parenchyma at 3 days post-infection (dpi).[216] The first aim of our study was to characterize in more detail in which cellular compartment of the distal lung GM-CSF is expressed during the course of influenza infection.

For this purpose, C57BL/6 WT mice were infected with 500 FFU PR8 IAV and the lungs were harvested at 2, 4, 7, and 10 dpi (Fig. **4.1 A**). BASCs, AECIs and AECIIs, airway epithelial cells, as well as rMCs were isolated via FACS from the lung cell suspension and subsequently subjected to GM-CSF gene expression analysis using qPCR. Cells were first separated from cell debris and doublets, the discrimination between live and dead cells was achieved through Sytox^{TM} Blue staining (Fig. **4.1 B**). BASCs were characterized by the markers CD31$^-$CD45$^-$EpCAM^{high}CD24^{low}Sca-1$^+$. Airway epithelial cells were identified as CD31$^-$CD45$^-$EpCAM^{high}CD24^{high}, and rMCs as CD31$^-$CD45$^-$EpCAM$^-$Sca-1$^+$. AECs were defined by CD31$^-$CD45$^-$EpCAM^{low}, and from these, living (Sytox$^-$) alveolar epithelial cells type 1 (T1α$^+$) and type 2 (T1α$^-$) were isolated.

In BASCs, the expression of the GM-CSF gene was significantly upregulated at 4 dpi (9 ± 2.75) and 7 dpi (6.68 ± 4.22) compared to the mock treatment (Fig. **4.1 C**). At 2 dpi (3.05 ± 3.41) and 14 dpi (1.73 ± 1.57), GM-CSF gene expression was present in BASCs but did not show a significant increase relative to the mock treatment. In AECs, GM-CSF gene expression was detectable at all time points, although no significant upregulation was observed. GM-CSF gene expression was not detectable in airway epithelial cells or rMCs.

The subsequent objective was to conduct a detailed analysis of GM-CSF gene expression within the AEC subpopulations and to determine whether GM-CSF is expressed in AECIs or AECIIs during IAV infection. GM-CSF gene expression was significantly upregulated in AECIIs at 4 and 7 dpi (Fig. **4.1 D**). At 4 dpi, GM-CSF gene expression in AECIIs was increased with a fold change of 4.3 ± 0.83 compared to mock-treated control while GM-CSF gene expression was increased with a fold change of 2.3 ± 1.04 at 7 dpi. There was no significant upregulation of GM-CSF gene expression in AECIs during IAV infection, suggesting that GM-CSF gene expression correlated with stem/progenitor function within the AEC compartment.

In summary, increased GM-CSF gene expression was observed in epithelial stem cells of the distal lung, particularly in BASCs and, to a lesser extent, in AECIIs at 4 and 7 dpi, correlating with their level of stemness. With these findings, our investigation prioritized exploring the impact of increased GM-CSF expression on alveolar epithelial repair mechanisms after IAV-mediated injury.

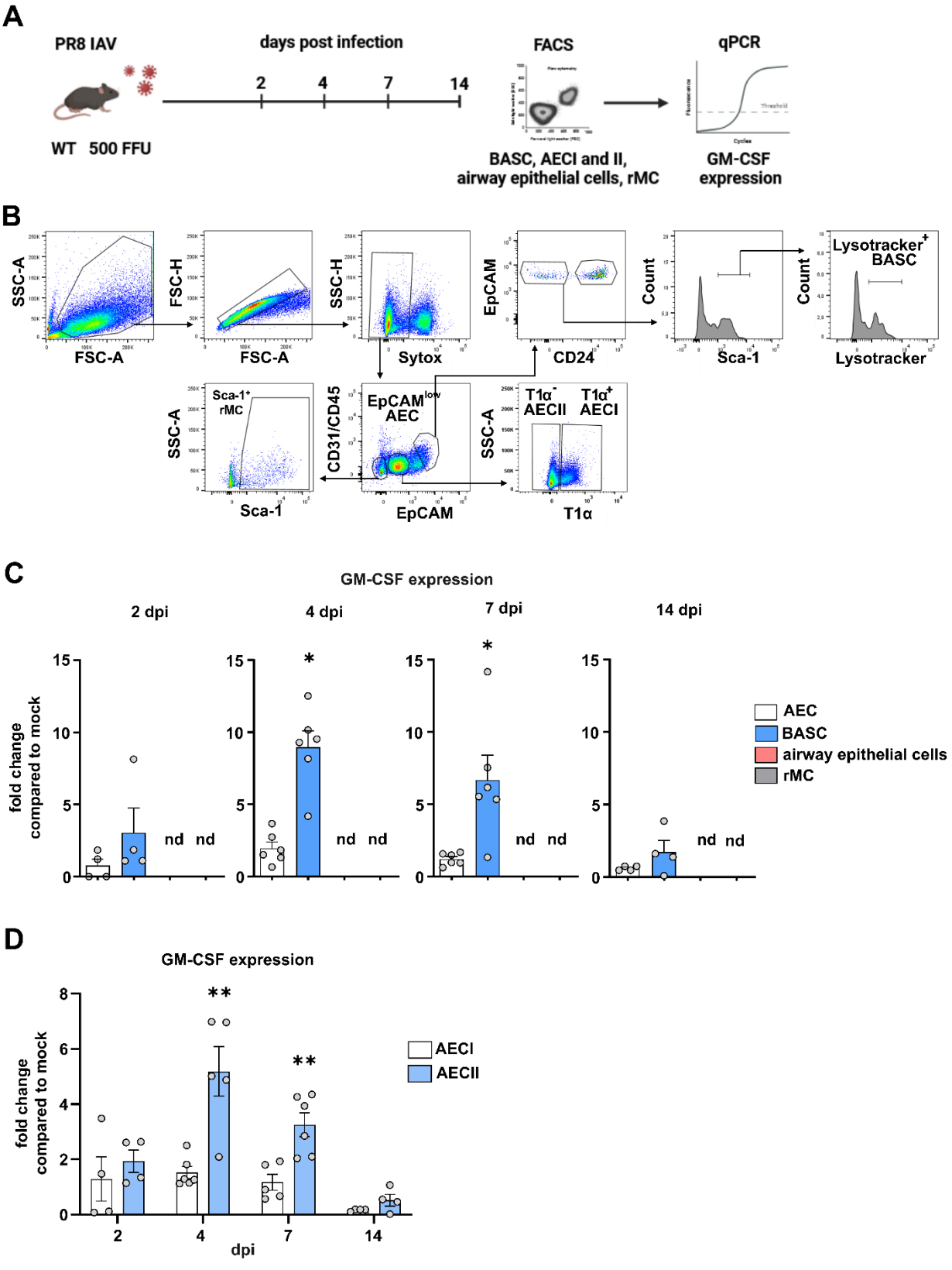

Figure 4.1: GM-CSF gene expression is upregulated in AECIIs and BASCs at 4 and 7 days after IAV infection. (A) Experimental setup: WT mice were infected with 500 FFU PR8 IAV. At 2, 4, 7, and 14 dpi, BASCs, AECs, airway epithelial cells, and rMCs were isolated from the lung homogenate using FACS to quantify GM-CSF gene expression via qPCR. Created using BioRender.com. **(B)** Gating

strategy for the isolation of living (Sytox^{-}) BASCs (CD31^{-}CD45^{-}EpCAM^{high}CD24^{low}Sca-1^{+}), AECI/IIs (CD31^{-}CD45^{-}EpCAM^{low}) type I (T1α^{+}) and type II (T1α^{-}), airway epithelial cells (CD31^{-}CD45^{-}EpCAM^{high}CD24^{high}), and rMCs (CD31^{-}CD45^{-}EpCAM^{-}Sca-1^{+}) from lung homogenate of infected WT mice. Cell debris and cell doublets were excluded. **(C-D)** GM-CSF gene expression at 2, 4, 7, and 14 dpi **(C)** in AECs, BASCs, airway epithelial cells and rMCs (n=4-6) and **(D)** in the AEC subpopulations, AECIs and AECIIs (n=4-5). Fold changes compared to mock are shown. Probabilities were determined using t-test. Graphs show means ± SEM; *=p<0.05; **=p<0.005.

4.2 During IAV infection, GM-CSF protects from lung damage by enhancing proliferation and reducing apoptosis in AECIIs and BASCs

Subsequent experiments were directed towards elucidating the impact of heightened GM-CSF levels on the proliferation and apoptosis rates of distal epithelial stem cells, including AECIIs and BASCs, specifically at 7 dpi. Moreover, the alveolar leakage was assessed**,** and lung histological sections were prepared to investigate the effect of GM-CSF on alveolar epithelial repair, particularly at 10 and 14 dpi.

In this part of the study, WT, Csf2-/-, and SPC-GM mice were utilized. Our previous studies showed that after IAV infection with a standardized infection dose of 500 FFU, discernible variability in alveolar leakage was noted among WT, Csf2-/-, and SPC-GM mice at 5 and 7 dpi.[216] This is mainly because GM-CSF improves the host's immune functions, thereby protecting the integrity of the alveolar barrier.[201] Since the concentrations of GM-CSF in the lungs of WT, Csf2-/-, and SPC-GM mice differ, it can be assumed that immune functions, and consequently virus concentrations, vary between these mouse strains.[221,251] This leads to different levels of lung injury.

To address the differing susceptibilities of WT, Csf2-/-, and SPC-GM mice to IAV infection, the infection doses were adjusted to ensure comparable virus concentrations and, consequently, similar levels of lung injury among the various mouse strains. With identical starting conditions for lung injury, it was possible to examine the effect of GM-CSF on alveolar epithelial barrier repair during the later stages of IAV infection, specifically at 10 and 14 dpi. To adjust the infection doses to achieve similar levels of virus particles in all three mouse lines, allowing to comparatively address repair processes driven by GM-CSF, the BALF collected at 3 dpi was titrated using a foci assay (Fig. **4.2 A**). The measurement at 3 dpi was chosen because IAV rapidly replicates within the first 1-2 days and reaches its peak by 3 dpi.[257] Moreover, at 7 dpi, assessment of alveolar leakage was conducted, and paraffin lung sections were stained with H&E to analyse if the induced alveolar damage is the same in all mouse strains. This analysis was performed at 7 dpi, as lung damage is expected to be most severe at this stage of IAV infection.

To reach the same viral load at 3 dpi, WT mice were infected with 500 FFU, Csf2-/- mice with 100 FFU, and SPC-GM mice with 2,000 FFU PR8 IAV. In WT mice, the

average virus titer was $4.91*10^5 \pm 1.91*10^5$, in Csf2-/- $5.9*10^5 \pm 1.53*10^5$, and in SPC-GM $4.85*10^5 \pm 1.92*10^5$ (Fig. **4.2 B**). The average virus titers among the different mouse strains differed by no more than one log unit, indicating marginal and non-significant differences. This indicates that the infection doses have been appropriately adjusted.

To further analyze if the adjusted infection doses cause equivalent levels of lung injury, alveolar leakage was quantified at 7 dpi (Fig. **4.2 C**). Alveolar leakage was determined by intravenously injecting FITC albumin and subsequently measuring the FITC fluorescence ratio in BALF over serum (where serum levels were divided by 100). Among WT (500 FFU), Csf2-/- (100 FFU), and SPC-GM (2000 FFU) mice, the observed extent of alveolar leakage revealed to be comparable, according to the well-adjusted IAV infection doses. The alveolar leakage was 0.4 AU ± 0.07, 0.35 AU ± 0.06, and 0.33 AU ± 0.04 in WT, Csf2-/-, and SPC-GM mice, respectively, indicating that the adjusted infection doses resulted in similar levels of alveolar barrier dysfunction among the different mouse strains.

Furthermore, lung sections were obtained from both WT and Csf2-/- mice infected with adjusted IAV doses to evaluate lung inflammation at 7 dpi (Fig. **4.2 D**). H&E-staining indicated comparable levels of epithelial damage and leukocyte infiltrations within the alveolar compartment in WT and Csf2-/- mice. As expected, these features were absent in the PBS-treated condition. However, a few enlarged, foamy macrophages were observed in the lungs of PBS-treated Csf2-/- mice.[221]

Overall, WT, Csf2-/-, and SPC-GM mice exhibited adjusted levels of lung injury attributable to the adjusted infection doses, therefore, allowing a comparative assessment of GM-CSF-mediated repair mechanisms after IAV injury in these mice.

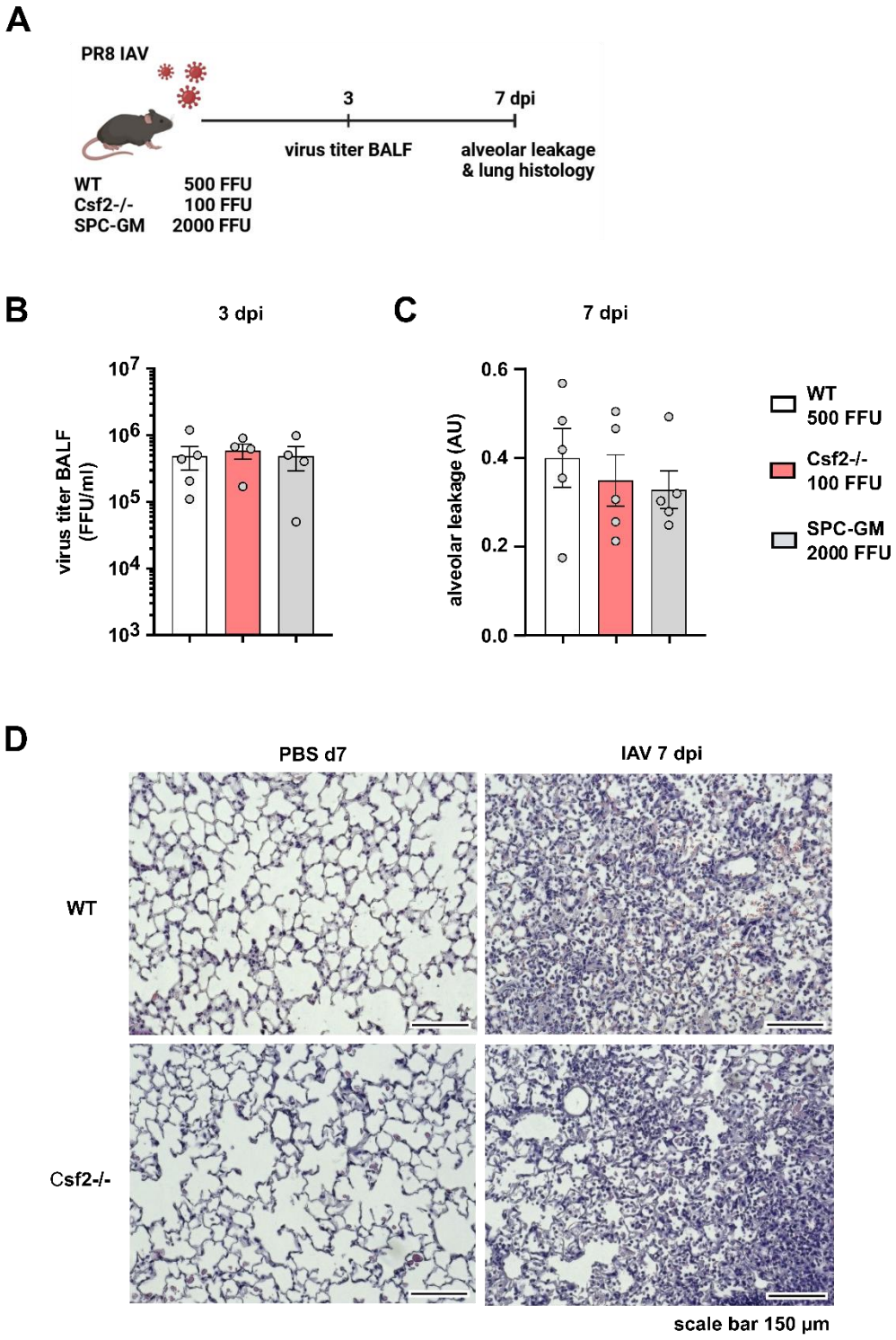

Figure 4.2: Adjusted IAV infection doses reach the same viral load and level of lung injury in WT, Csf2-/-, and SPC-GM mice. (A) Experimental setup: WT (500 FFU), Csf2-/- (100 FFU), and SPC-GM (2,000 FFU) mice were infected with PR8 IAV. At 3 dpi, the virus titer in the BALF was analyzed. At 7 dpi, alveolar leakage was determined, and histological sections were prepared. Created using BioRender.com. **(B)** BALF virus titers in WT (500 FFU), Csf2-/- (100 FFU), and SPC-GM (2,000 FFU) mice at 3 dpi (n = 4-5). Graph shows means ± SEM. **(C)** Alveolar leakage in WT (500 FFU), Csf2-/- (100 FFU), and SPC-GM (2000 FFU) mice infected with adjusted virus doses at 7 dpi (n=5). Graph

shows means ± SEM. **(D)** Representative transmission microscopy images of lung paraffin sections stained with H&E from WT (500 FFU) and Csf2-/- (100 FFU) mice 7 dpi. Scale bar represents 150 µm.

Next, quantification of proliferating and apoptotic AECIIs and BASCs at 7 days after infection with adjusted IAV doses was conducted using FACS (Fig. **4.3 A**). In the gating strategy, cell debris and doublets were excluded (Fig. **4.3 B**). The AECII-enriched population ($CD31^-CD45^-EpCAM^{low}$) and BASC-enriched population ($CD31^-CD45^-EpCAM^{high}CD24^{low}Sca\text{-}1^+$) were analyzed for the percentages of proliferating ($Ki67^+$) or apoptotic ($AnnexinV^+$) cells by comparison to the isotype or AnnexinV-unstained control.[42] At 7 dpi, the proportion of proliferating AECIIs was elevated in WT (20.6% ± 2.6) and SPC-GM (20.1% ± 1) compared to Csf2-/- (8.8% ± 1.3) mice (Fig. **4.3 C**). Similarly, BASC proliferation was increased in WT (26.1% ± 1.2) and SPC-GM (36.7% ± 3.2) compared to Csf2-/- (13.7% ± 2.6) mice. Notably, a significant difference in the proportion of proliferating BASCs was observed between WT and SPC-GM mice. The amount of apoptotic AECIIs was heightened in Csf2-/- (28.8% ± 2.2) compared to WT (20.7% ± 1.8) and SPC-GM (17.8% ± 1.4) mice. Similarly, within the BASC population, there was a significant increase in apoptosis in Csf2-/- (27.5% ± 2.2) compared to WT (20.3% ± 2.5) and SPC-GM (13% ± 1.3) mice (Fig. **4.3 D**).

In summary, the findings indicate that following IAV infection, GM-CSF promotes AECII and BASC proliferation while protecting them from apoptosis at 7 dpi. Subsequent investigations focused on understanding the influence of GM-CSF on alveolar epithelial repair mechanisms during the later stage of IAV infection at 10 and 14 dpi.

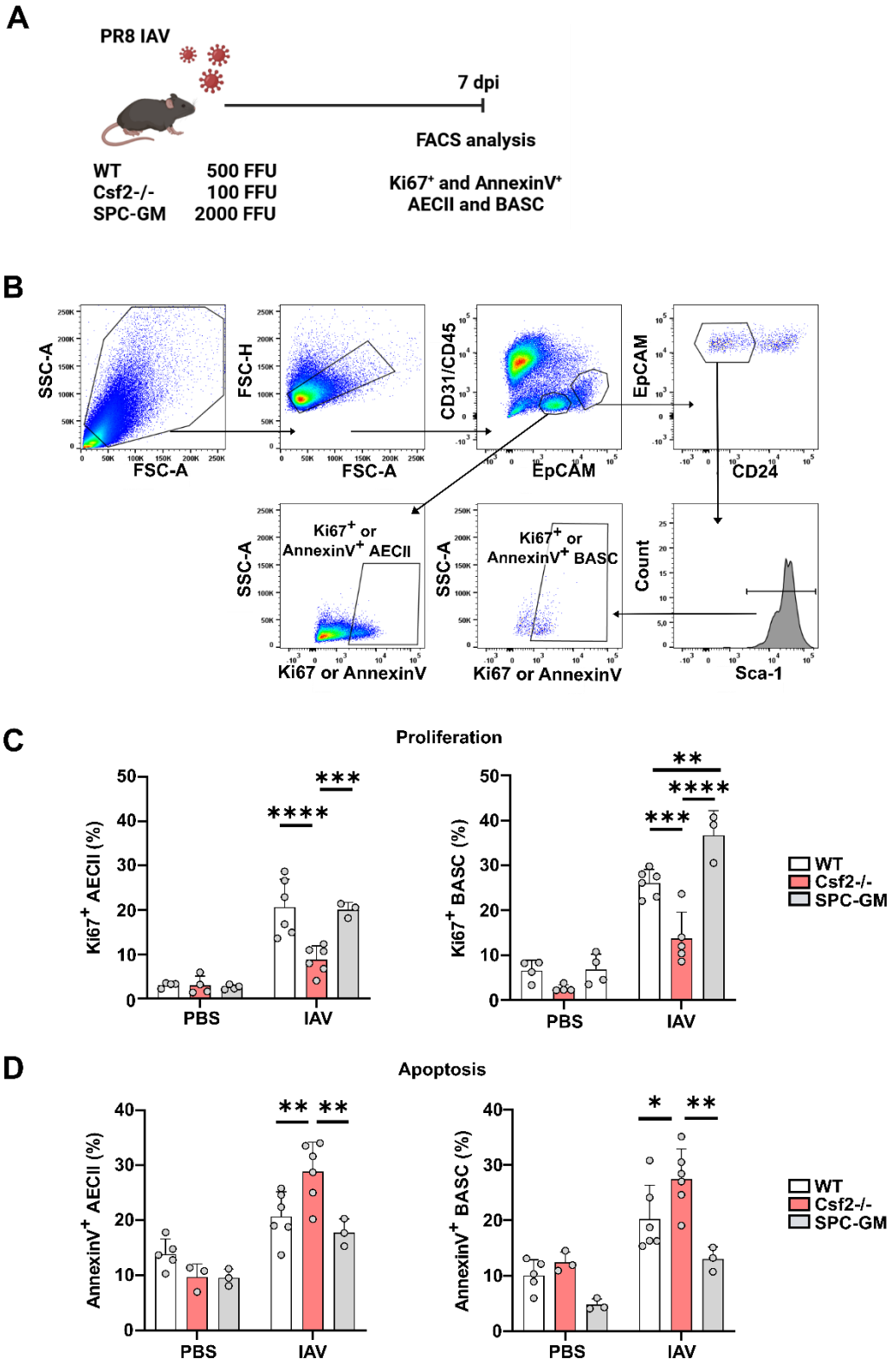

Figure 4.3: GM-CSF mediates AECII and BASC proliferation after IAV infection. **(A)** Experimental setup: WT (500 FFU), Csf2-/- (100 FFU), and SPC-GM (2,000 FFU) mice were infected with adjusted IAV doses. At 7 dpi, the amount of proliferating and apoptotic AECIIs and BASCs was determined by FACS. Created using BioRender.com. **(B)** Gating strategy for the measurement of proliferating or apoptotic AECIIs and BASCs. Cell debris and cell doublets were excluded. The AECII-

enriched ($CD31^-CD45^-EpCAM^{low}$) as well as BASC-enriched ($CD31^-CD45^-EpCAM^{high}CD24^{low}Sca\text{-}1^+$) populations were analyzed for proliferating ($Ki67^+$) and apoptotic ($AnnexinV^+$) cells. **(C)** Amount of proliferating AECIIs and BASCs at 7 dpi in WT (500 FFU), Csf2-/- (100 FFU), and SPC-GM (2,000 FFU) mice infected with adjusted IAV doses at 7 dpi (n=3-6). **(D)** Amount of apoptotic AECIIs and BASCs at 7 dpi in WT (500 FFU), Csf2-/- (100 FFU), and SPC-GM (2,000 FFU) mice infected with adjusted IAV doses at 7 dpi (n=3-6). Probabilities were determined using one-way ANOVA. Graphs show means ± SEM; *=p<0.05; **=p<0.005; ***=p<0.001; ****=p<0.0001.

In the next step, the influence of GM-CSF on alveolar epithelial repair during later stages of the disease course, where repair processes take place, was investigated.[193] Therefore, WT, Csf2-/-, and SPC-GM mice were infected with adjusted IAV doses to measure alveolar leakage and obtain lung histological sections at 10 and 14 dpi (Fig. **4.4 A**). Alveolar leakage remained increased in Csf2-/- (mean 0.5 AU ± 0.1) compared to WT (mean 0.2 AU ± 0.01) and SPC-GM mice (mean 0.17 AU ± 0.02) at 10 dpi (Fig. **4.4 B**), suggesting that presence of GM-CSF enhances alveolar barrier repair following IAV infection.

Additionally, histological examination of lung sections stained with H&E was performed on both WT and Csf2-/- mice infected with adjusted IAV doses at 10 and 14 dpi (Fig. **4.4 C and D**) to assess lung inflammation and the integrity of the alveolar epithelial barrier. In lung sections from WT mice, few intraalveolar leukocyte infiltrates are still visible at 10 dpi, but they appear to have resolved by 14 dpi, showing no discernible difference from the PBS control. Furthermore, the alveolar structure in WT mice seems recovered by 14 dpi. Conversely, in Csf2-/- mice, leukocytic infiltrates appear to be more prominent than in WT mice at both 10 and 14 dpi, with no resolution of inflammation observed until 14 dpi. These observations suggest that, despite similar levels of lung damage at 7 dpi in both WT and Csf2-/- mice (Fig. **4.4 D**), GM-CSF facilitates viral clearance, inflammation resolution, and/or lung repair in WT mice compared to Csf2-/- mice, as evidenced at 10 and 14 dpi.

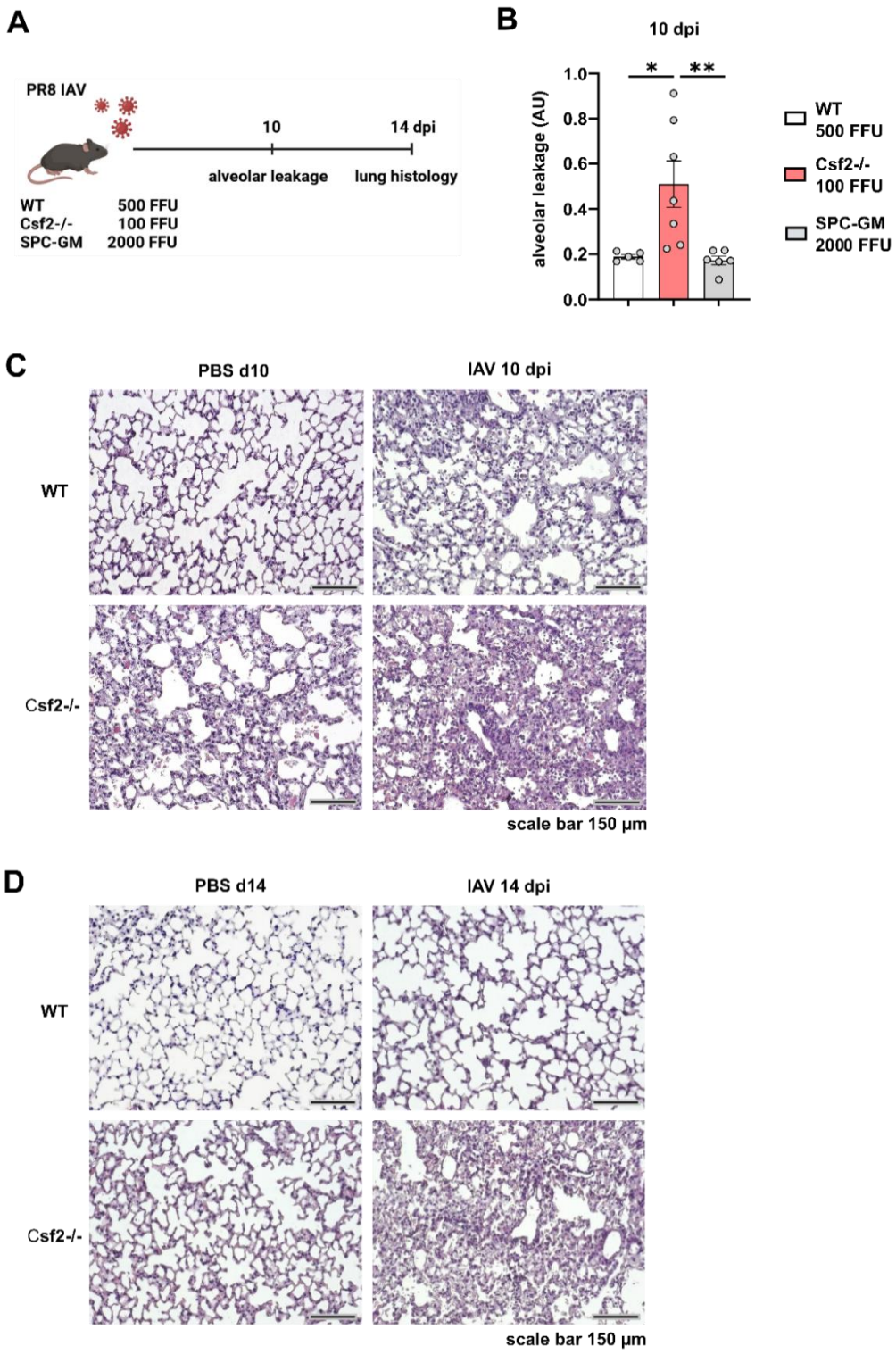

Figure 4.4: GM-CSF is crucial for alveolar barrier repair after IAV infection. (A) Experimental setup: WT (500 FFU), Csf2-/- (100 FFU), and SPC-GM (2,000 FFU) mice were infected with adjusted IAV doses to compare alveolar leakage and lung histological sections at 10 and 14 dpi. Created using BioRender.com. **(B)** Alveolar leakage in WT, Csf2-/-, and SPC-GM mice at 10 days after IAV infection with adjusted doses. **(C-D)** Representative transmission microscopy images from H&E-stained paraffin lung sections obtained from WT and Csf2-/- mice at **(C)** 10 and **(D)** 14 dpi. Probabilities were determined using one way ANOVA. Graph shows means ± SEM; *=p<0.05; **=p<0.005.

4.3 GM-CSF/GM-CSFRβ signaling is crucial for BALO development

In the subsequent part of the study, the objective was to investigate the impact of GM-CSF on the formation of alveolospheres and BALOs derived from AECIIs and BASCs.[184] Preliminary data (not shown) demonstrated that BALOs with Csf2-/- and Csf2rb-/- background were impaired in their development compared to WT BALOs. In cultures lacking GM-CSF, BALOs exhibited reduced size, decreased organoid forming efficiency (OFE), and less differentiated branching morphology compared to WT cultures. BALOs with Csf2rb-/- background maintained an unaltered OFE, but displayed impaired alveolarization when compared to day 21 WT cultures.

BALOs were generated following the previously established protocol (2020).[184] From the leukocyte/endothelial cell-depleted lung cell suspension of WT, Csf2rb-/-, or Csf2-/- mice, populations enriched with rMCs and BASCs were isolated via FACS. The rMC-enriched population was defined as $EpCAM^{-}Sca\text{-}1^{+}$, while the BASC-enriched population was characterized as $EpCAM^{high}CD24^{low}Sca\text{-}1^{+}$.[42] Both cell populations were co-cultured in Matrigel for a duration of 21 days to facilitate the growth of BALOs originating from $Sftpc^{+}Scgb1a1^{+}$ BASCs.[184]

To further elucidate the role of GM-CSF/GM-CSFRβ signaling in BALO development, BALOs derived from WT, Csf2rb-/-, and Csf2-/- rMCs and BASCs were stained for ProSPC (AECII marker) and Caveolin-1 (Cav-1, AECI marker) on day 21 of culture. Confocal microscopy z-stack images were acquired to measure the mean perimeter of the alveolar lumen (Figure **4.5 A and B**). The mean perimeter of the luminal structure was higher in Csf2rb-/- (95.22 µm ± 2.79) than in WT BALOs (71.49 µm ± 3.37) (Figure **4.5 B**). Also the mean area of the luminal structure was increased in Csf2rb-/- (633.7 μm^2 ± 41) compared to WT BALOs (332.8 μm^2 ± 40.12). In the Csf2-/- condition, the majority of BALOs remained small, with no development of alveolar structures observed (Fig. **4.5 A**). As a result, measurement of the alveolar lumen was not feasible, leading to the exclusion of Csf2-/- BALOs from the analysis. These findings indicate that the absence of GM-CSF/GM-CSFRβ signaling impairs proper BALO development and alveolarization (with developing alveoli displaying declining perimeter values), which is characterized by lower complexity along with a larger alveolar lumen.

To further explore the dependency of BALO development on the presence of GM-CSF, the concentration of GM-CSF in the supernatant (SN) of BALO cultures with

WT, Csf2-/-, and Csf2rb-/- background was quantified using ELISA (Fig. **4.5 C**). In WT BALO cultures, the concentration of GM-CSF showed an initial increase at day 6 of culture, reaching a level of 96 pg/ml ± 9.6. Subsequently, the GM-CSF concentration in WT cultures gradually declined to 13.8 pg/ml ± 3.7 by day 15. In contrast, in Csf2rb-/- cultures, the increase in GM-CSF concentration was delayed compared to WT, reaching 84.5 pg/ml ± 16.5 by day 11. From day 13 to 20, the GM-CSF concentration in Csf2rb-/- cultures remained high, ranging from 70 to 90 pg/ml, and was significantly elevated compared to the WT condition. This result indicates a compensatory overexpression of GM-CSF in AECIIs and BASCs, likely due to the absence of feedback from rMCs lacking the GM-CSF receptor. GM-CSF was not detected in the supernatants of Csf2-/- BALO cultures. These findings suggest a temporal increase in GM-CSF concentration in WT cultures, peaking at day 6, followed by a decline, which may be crucial for proper BALO development.

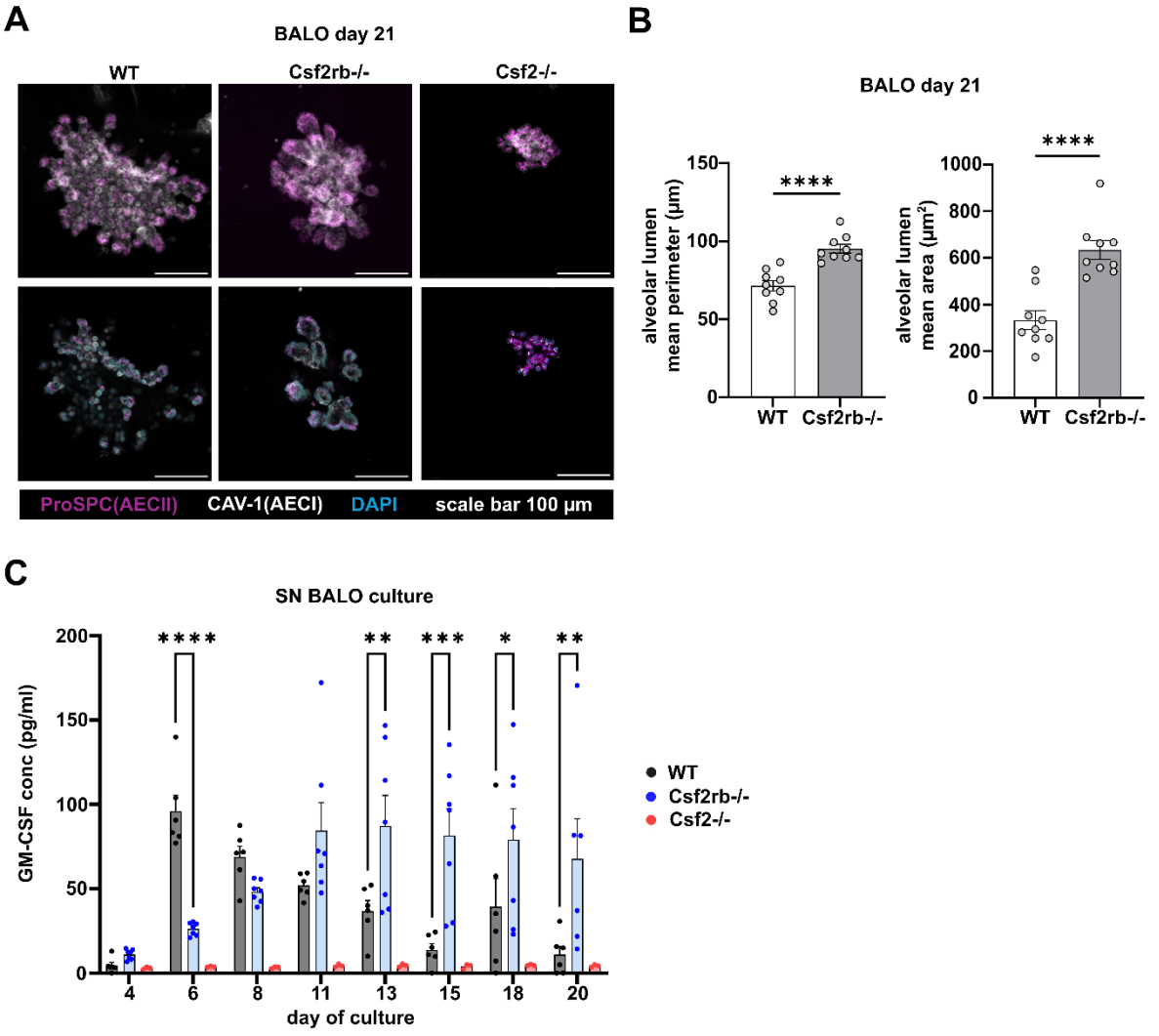

Figure 4.5: GM-CSF is released into the SN of BALO cultures and improves BALO alveolarization. (A) Representative confocal microscopy images of BALOs derived from WT, Csf2rb-/-, or Csf2-/- BASCs and rMCs. At day 21 of culture, BALOs were stained for ProSPC (AECII marker) and Cav-1 (AECI marker) to depict the alveolar regions. Scale bar represents 100 µm. **(B)** Mean perimeter of the alveolar lumen measured in WT and Csf2rb-/- BALOs at day 21 of culture. Probabilities were determined using t test. **(C)** GM-CSF concentration (pg/ml) in supernatant of BALOs derived from WT, Csf2rb-/-, or Csf2-/- BASCs and rMCs. Probabilities were determined using 2way ANOVA. Graphs show means ± SEM. *=p<0.05; **=p<0.005; ***=p<0.001; ****=p<0.0001.

To assess whether in Csf2-/- cultures the development of BALOs could be restored by the supplementation of exogenous GM-CSF into the supernatant (SN), a protocol was implemented where 50 pg/ml of GM-CSF was added to the medium from day 6 to 10 of culture, followed by 100 pg/ml from day 10 to 14, and then 50 pg/ml from day 14 to 18 (Fig. **4.6 A**). Representative transmission microscopy images illustrate that the cultures treated with GM-CSF contained several large BALOs that were absent in the untreated control by day 21 of culture (Fig. **4.6 B**). Moreover, BALOs in the GM-CSF-treated condition displayed a phenotype characterized by enhanced alveolarization compared to the untreated control (Fig. **4.6 B**). Size measurements indicated an increased area and perimeter of (bronchio)alveolar organoids in the GM-CSF-treated group at day 21 of culture (Fig. **4.6 C**). Specifically, a median area of 47,892 µm^2 was observed in the GM-CSF-treated condition, which was significantly higher than that in the control group (median 32,454 µm^2). Similarly, the perimeter of (bronchio)alveolar organoids was significantly increased in the GM-CSF-treated condition (median 836 µm) compared to untreated (median 701,4 µm). This experiment highlights that the development of Csf2-/- BALOs can indeed be restored by the addition of GM-CSF, thus stressing the role of GM-CSF in BASC and AEC proliferation and differentiation.

To further analyze if GM-CSF/GM-CSFRβ signaling induces proliferation in distal alveolar epithelial progenitor cells, AECIIs were isolated from WT and Csf2rb-/- mice via FACS. AECIIs were characterized as CD45$^-$CD31$^-$EpCAM^{low}Lysotracker$^+$ (see Fig. **4.8 B**). Subsequently, the AECIIs were cultured in Matrigel and treated with GM-CSF (100 ng/ml) for 16 h. The gene expression of *Cyclin D1* (*Ccnd1*) was analyzed using qPCR. Ccnd1 is known to regulate the transition from G1 to S-phase by binding to cyclin-dependent kinases (CDK) 4 and 6. The resulting Ccnd1/CDK4 dimer can

translocate into the nucleus, where it facilitates the activation of the transcription factor E2F, thus initiating the expression of genes required for cell proliferation.[258]

The addition of GM-CSF to the SN significantly augmented *Ccnd1* expression in WT AECIIs (fold change compared to PBS 1.5 ± 0.09) 16 h after treatment start (Fig. **4.6 D**). Conversely, there was no discernible increase in *Ccnd1* expression in AECIIs from Csf2rb-/- mice (fold change compared to PBS 0.97 ± 0.2). This result shows that GM-CSF/GM-CSFRβ signaling in distal alveolar epithelial progenitor cells enhances *Ccnd1* gene expression levels.

In a subsequent experiment, BASCs were isolated from IAV-infected WT and Csf2rb-/- mice at 7 dpi and compared to mock-treated controls for the generation of BALOs (Fig. **4.6 E**). BASCs from infected mice were co-cultured with rMCs derived from untreated WT or Csf2rb-/- mice. On day 21 of culture, the OFE was determined. Notably, in WT BALO cultures, the OFE was significantly elevated when BASCs from IAV-infected mice (1.84 ± 0.47) were used, compared to those from mock-treated controls (0.31 ± 0.03) (Fig. **4.6 F and G**). In contrast, the absence of GM-CSF/GM-CSFRβ signaling abrogated the increase in OFE observed after IAV infection (0.83 ± 0.1) relative to the mock-treated control (0.39 ± 0.09). This result suggests that the elevated expression of GM-CSF in BASCs following IAV infection (see Fig. **4.1**) enhances their capacity for organoid formation.

These findings indicate that GM-CSF is crucial for BALO development and promotes proliferation in distal epithelial stem cells. Further experiments were conducted to elucidate the mechanisms underlying these observations.

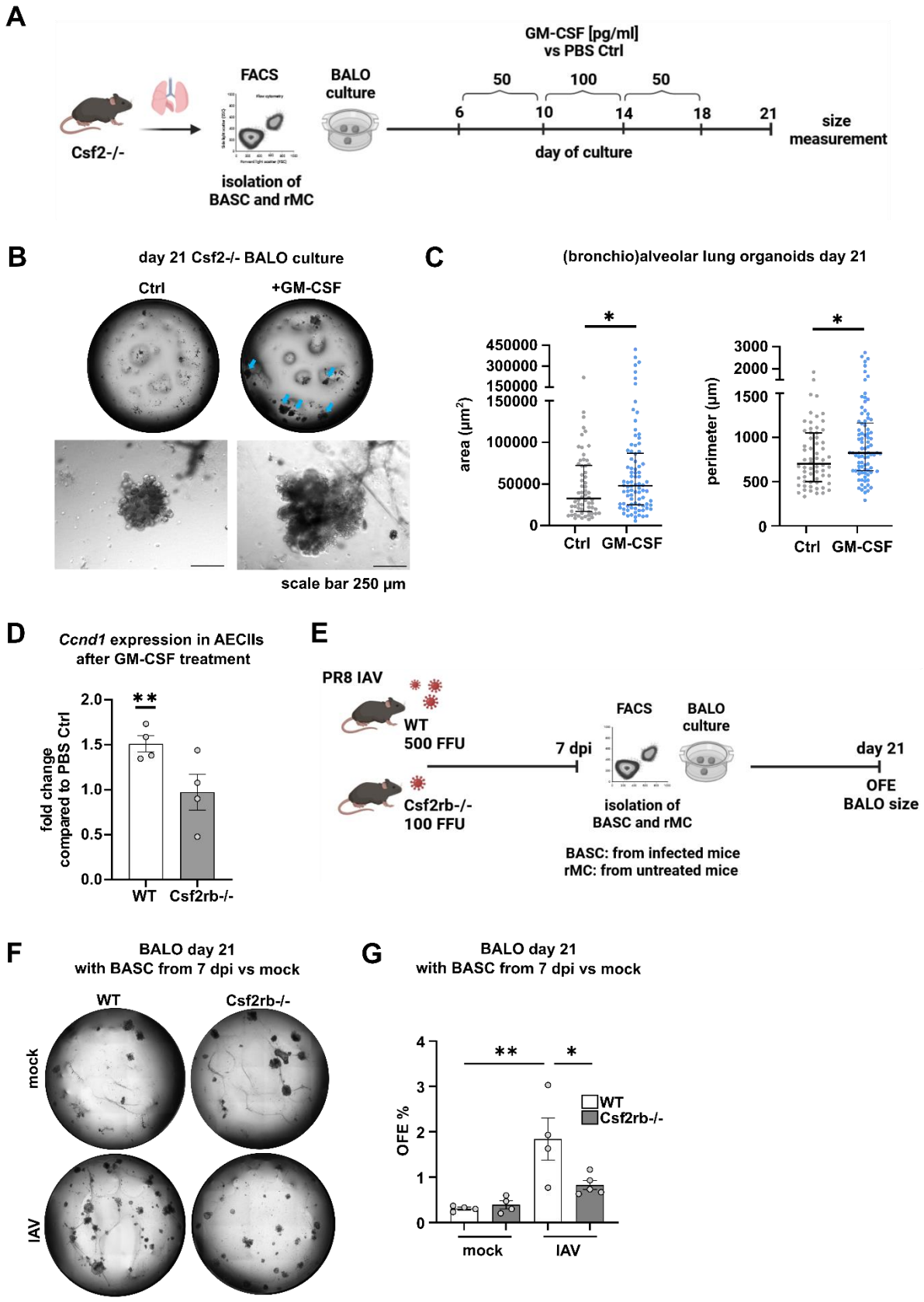

Figure 4.6: GM-CSF/GM-CSFRß signaling is crucial for BALO development and BASC proliferation. (A) Experimental setup: BASCs and rMCs were isolated from Csf2-/- mice for BALO co-culture. Exogenous recombinant GM-CSF was supplemented to the medium: 50 pg/ml from day 6 to

10, 100 pg/ml from day 10 to 14, and 50 pg/ml from day 14 to 21. Then, the size of the (bronchio)alveolar organoids was measured at day 21 of culture. Created using BioRender.com. **(B)** Representative transmission microscopy images of Csf2-/- BALO cultures treated with GM-CSF vs PBS control. Scale bar represents 500 µm. **(C)** Area and perimeter of (bronchio)alveolar lung organoids derived from Csf2-/- BALO cultures treated with GM-CSF versus PBS control. Graphs show medians with interquartile ranges. Probabilities were determined using Mann-Whitney test. *=p<0.05. **(D)** *Ccnd1* gene expression in AECIIs isolated from WT and Csf2rb-/- mice and treated with recombinant GM-CSF for 16 h *ex vivo*. Graph shows means ± SEM. Probability was determined using t-test. **(E)** Experimental setup: BASCs were isolated from WT and Csf2rb-/- mice at 7 dpi vs mock control for BALO co-culture with rMC from untreated WT or Csf2rb-/- mice. At day 21 of culture, the organoid forming efficiency (OFE) was determined. Created using BioRender.com. **(F)** Representative transmission microscopy images and **(G)** OFE (%) of BALOs generated with BASCs from IAV-infected mice versus mock control on day 21 of culture (n=4)**.** Probabilities were determined using one-way ANOVA. Graphs show means ± SEM. *=p<0.05; **=p<0.005.

4.4 GM-CSF mediates its effects by regulating the AMPK-mTORC1 signaling pathway in alveolar epithelial stem cells

The previous findings highlight the crucial role of GM-CSF/GM-CSFRβ signaling in distal epithelial stem cells by inducing proliferation and facilitating alveolar epithelial barrier repair. Subsequently, efforts were directed towards unraveling the underlying mechanisms responsible for the GM-CSF-mediated effects. To achieve this, a bulk RNA sequencing experiment was conducted utilizing BASCs from both WT and Csf2-/- mice, either 7 days after IAV infection or mock treatment (Fig. **4.7 A**). The aim was to analyze how gene expression is influenced by GM-CSF following IAV infection within the BASC compartment and identify potential GM-CSF-mediated signaling pathways.

To assess the variability in gene expression among the experimental groups, a PCA (principal component analysis) plot was generated (Fig. **4.7 B**). The analysis revealed that biological replicates from each condition clustered separately, indicating distinct differences in gene expression profiles between WT and Csf2-/- BASCs under both infected and mock-treated conditions. To identify the exact processes within the cell that are regulated by GM-CSF after IAV infection, a KEGG (Kyoto Encyclopedia of Genes and Genomes) pathway analysis was performed. The top 20 pathways with differential gene expression were summarized in a heat map (Fig. **4.7 C**). In BASCs from both infected WT and infected Csf2-/- mice, pathways associated with viral infections (such as Human T-cell leukemia virus 1 infection, Influenza A, Viral carcinogenesis, Epstein-Barr virus infection, Herpes simplex infection, and Human papillomavirus infection) showed alterations in gene expression compared to the corresponding mock-treated groups. When comparing gene expression between BASCs from WT infected and Csf2-/- infected mice, differences in pathways related to cytokine-cytokine receptor interactions were observed, suggesting variations in the inflammatory response to IAV infections between WT and Csf2-/- mice. Additionally, genes related to cell cycle and apoptosis were differentially expressed in WT infected BASCs compared to WT mock-treated control, indicating that GM-CSF might be involved in BASC proliferation and survival. Moreover, metabolic pathways and oxidative phosphorylation exhibited differential gene expression in BASCs from WT and Csf2-/- mice under infected conditions.

All in all, the KEGG pathway analysis revealed that GM-CSF seems to be important for the regulation of metabolic pathways. Previous studies have demonstrated that IAV infection alters the metabolic state of AECs by activating AMPK.[63] Another publication showed that in macrophages, the GM-CSF-mediated increase in proliferation is suppressed by AMPK activation.[139] Based on these data, the hypothesis was developed that GM-CSF induces alterations in the metabolic state of alveolar epithelial stem cells by inhibiting AMPK and subsequently activating downstream mTORC1. This cascade of events is proposed to lead to enhanced proliferation of alveolar epithelial stem cells, thereby promoting alveolar epithelial barrier repair.

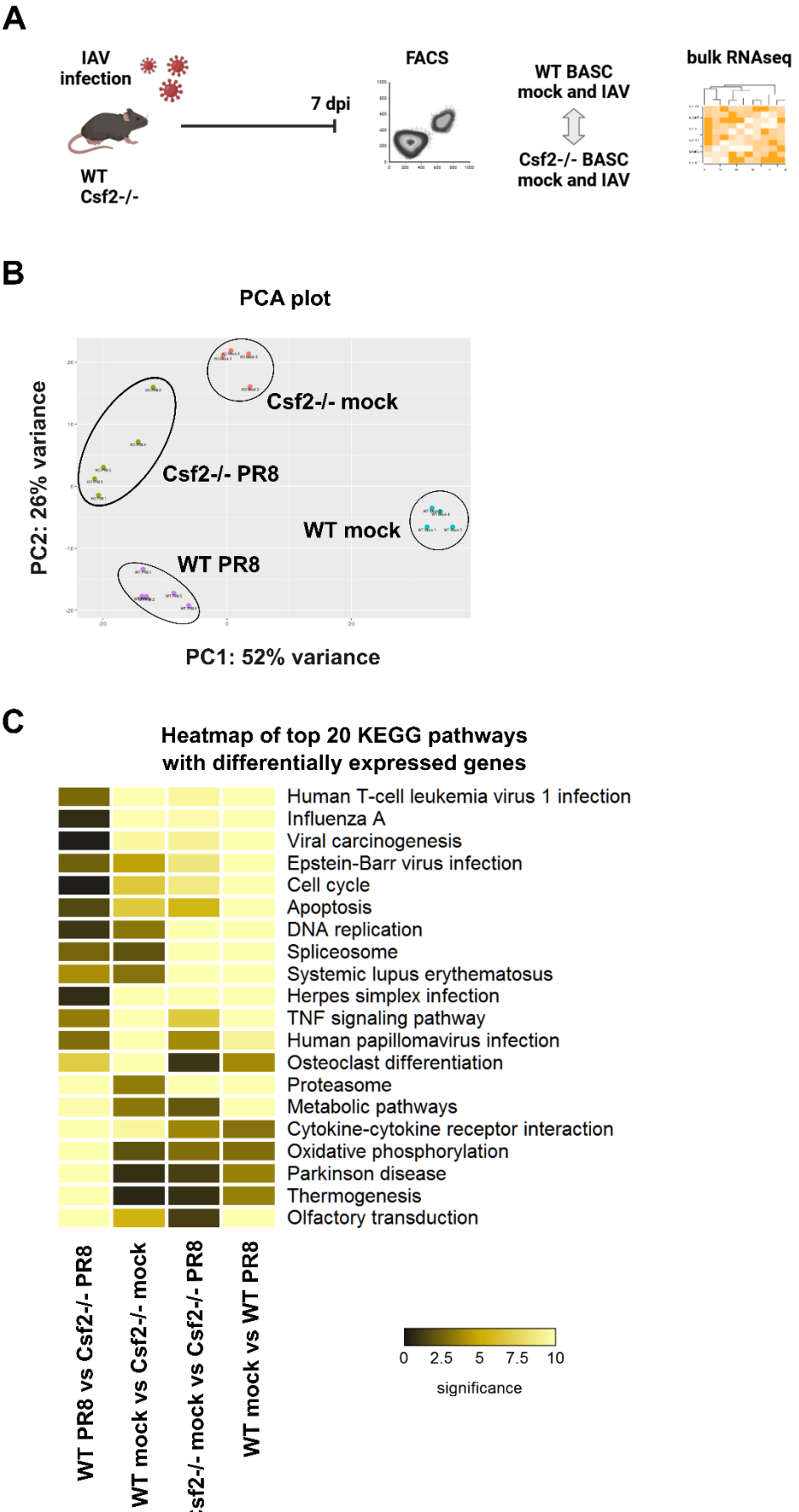
A
IAV infection
7 dpi
WT
Csf2-/-
FACS
WT BASC mock and IAV
Csf2-/- BASC mock and IAV
bulk RNAseq
B
PCA plot
Csf2-/- mock
Csf2-/- PR8
WT mock
WT PR8
PC2: 26% variance
PC1: 52% variance
C
Heatmap of top 20 KEGG pathways with differentially expressed genes
Human T-cell leukemia virus 1 infection
Influenza A
Viral carcinogenesis
Epstein-Barr virus infection
Cell cycle
Apoptosis
DNA replication
Spliceosome
Systemic lupus erythematosus
Herpes simplex infection
TNF signaling pathway
Human papillomavirus infection
Osteoclast differentiation
Proteasome
Metabolic pathways
Cytokine-cytokine receptor interaction
Oxidative phosphorylation
Parkinson disease
Thermogenesis
Olfactory transduction
WT PR8 vs Csf2-/- PR8
WT mock vs Csf2-/- mock
Csf2-/- mock vs Csf2-/- PR8
WT mock vs WT PR8
0 2.5 5 7.5 10
significance

Figure 4.7: Bulk RNA sequencing analysis reveals differential expressions of genes related to metabolic pathways between WT and Csf2-/- BASCs upon IAV infection. (A) Experimental setup: WT and Csf2-/- mice were infected with 500 FFU or mock treated. At 7 dpi, BASCs were isolated by FACS and utilized for bulk RNA sequencing (n=4-5). **(B)** PCA plot displaying clusters of WT and Csf2-/- samples, infected and mock treated (n=4-5). **(C)** Heatmap showing the top 20 KEGG pathways with differential gene expression between the depicted experimental groups. The -log(p) values denote the significance and range between 0 and 10. Higher values indicate a higher significance. Low values are represented by a black square and high values by a yellow square.

Subsequent steps focused on validating the hypothesis that GM-CSF inhibits AMPK, thereby facilitating increased mTORC1 activity. AECs were isolated from WT, Csf2-/-, and Csf2rb-/- mice for *ex vivo* 2D cell culture (Fig. **4.8 A**). These primary murine AECs were infected with PR8 IAV with an MOI of 0.1, or mock-treated, with the addition of exogenous recombinant murine GM-CSF for 24 h.

AMPK activity is regulated through various mechanisms, with its upstream kinase AMPKK playing a crucial role in its activation.[259] AMPKK is directly activated by AMP when the energy charge of the cell is low.[259] Phosphorylation of Thr^{172} in the α^1 and α^2 subunits of AMPK by AMPKK induces activation of the AMPK complex.[259] Therefore, the phospho-AMPK(Thr^{172})/AMPK ratio was utilized as a marker for AMPK activity.

In WT AECs, the phospho-AMPK(Thr^{172})/AMPK ratio increased to a mean value of 3.3 ± 0.74 upon IAV infection (Fig. **4.8 B**). Supplementation with GM-CSF into infected cultures significantly reduced this ratio to 1.16 ± 0.26 (Fig. **4.8 B**). Similarly, in Csf2-/- AECs, the phospho-AMPK(Thr^{172})/AMPK ratio showed a significant increase upon IAV infection (mean 1.82 ± 0.35), which was reversed by the addition of GM-CSF to the medium, resulting in a decreased phospho-AMPK(Thr^{172})/AMPK ratio (0.95 ± 0.12) (Fig. **4.8 C**). Notably, in mock-treated conditions, the addition of GM-CSF did not significantly affect the mean phospho-AMPK(Thr^{172})/AMPK ratio in WT (1.35 ± 0.32), Csf2-/- (0.94 ± 0.07), and Csf2rb-/- (1.21 ± 0.32) AECs. Furthermore, the level of phosphorylated AMPK was elevated in IAV-infected Csf2rb-/- AECs (mean ratio of 2.35 ± 0.75) (Fig. **4.8 D**). However, due to the absence of GM-CSF signaling, the addition of GM-CSF did not influence the phospho-AMPK(Thr^{172})/AMPK ratio (mean 2.71 ± 1.44) (Fig. **4.8 D**).

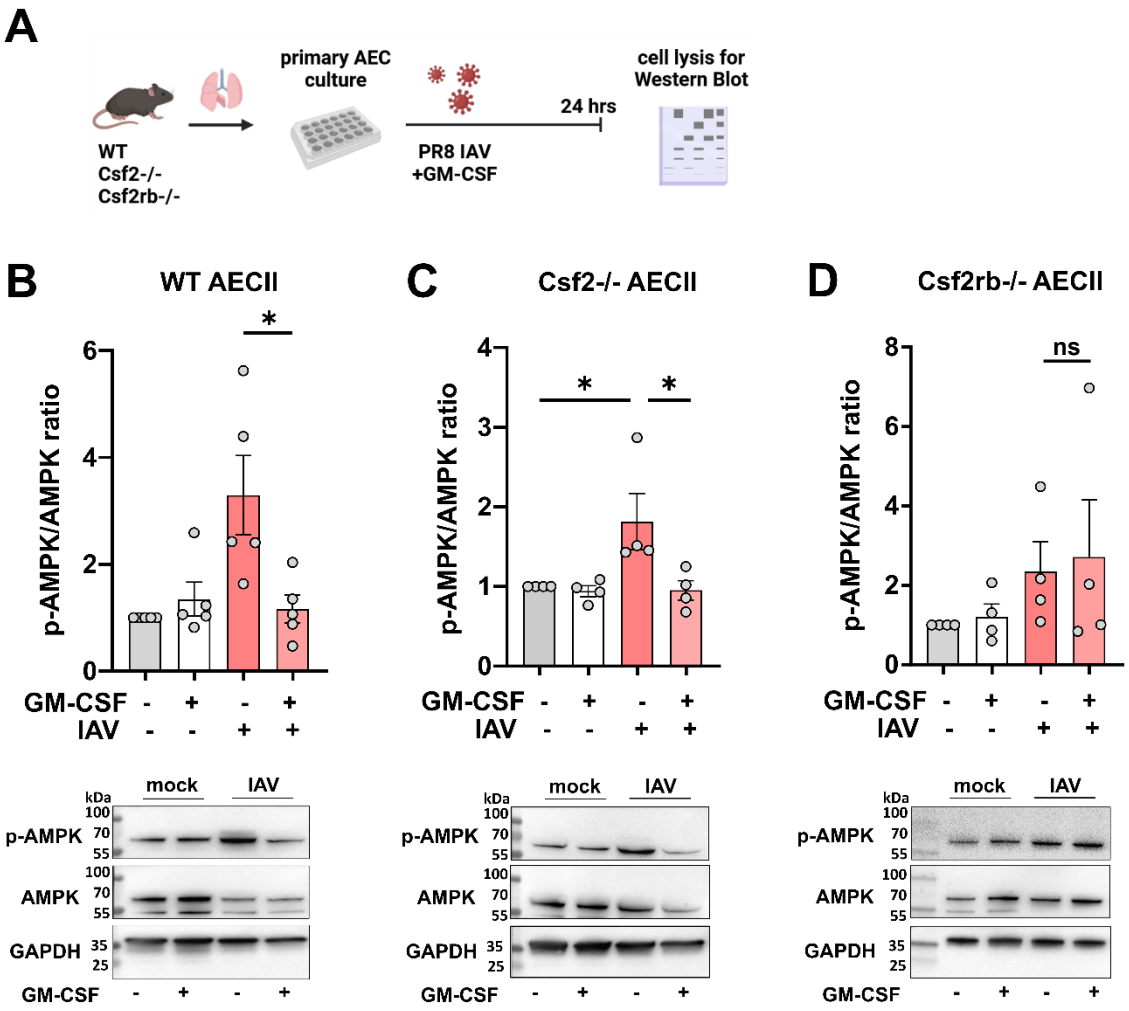

Figure 4.8: GM-CSF inhibits AMPK activity in murine AECs following IAV infection *ex vivo*. (A) Experimental setup: Lungs from WT, Csf2-/-, and Csf2rb-/- mice were collected. AECs were isolated and cultured for infection with PR8 IAV (MOI 0.1) and treatment with recombinant GM-CSF (50 ng/ml). At 24 hpi, the cell lysates were prepared, and utilized for Western Blot analysis to assess AMPK activity indicated by p-AMPK/AMPK ratio. Created using BioRender.com. **(B-D)** AMPK activity in primary murine AECs from **(B)** WT, **(C)** Csf2-/-, and **(D)** Csf2rb-/- mice 24 h after *ex vivo* PR8 IAV infection and recombinant GM-CSF treatment. Representative Western Blot images depict (p-)AMPK at 62 kDa and GAPDH at 37 kDa (n=4-5). Probabilities were determined using one-way ANOVA. Graphs show means ± SEM; *=p<0.05.

In the following experiments, it was investigated whether GM-CSF not only downregulates AMPK but also consequently activates its downstream effector mTORC1. As an indicator of mTORC1 activity, the phospho-70-kDa ribosomal protein S6 kinase (phospho-p70S6K) / p70S6K ratio was determined. One of the main targets and downstream effectors of mTORC1 is p70S6K, which phosphorylates

numerous targets, including the ribosomal protein S6 (see chapter 1.3.2).[260] This phosphorylation event enhances translation initiation and elongation, promotes ribosome biogenesis, and facilitates the translation of proteins involved in regulating cell growth and division.[260]

In IAV-infected WT AECs, the phospho-p70S6K/p70S6K ratio was increased from a mean value of 1.26 ± 0.27 to 2.36 ± 0.3 upon the addition of GM-CSF (Fig. **4.9 A**). Similarly, in Csf2-/- AECs, exogenous GM-CSF enhanced the phospho-p70S6K/p70S6K ratio upon IAV infection from a mean value of 0.29 ± 0.08 to 1.5 ± 0.26 (Fig. **4.9 B**). In infected Csf2rb-/- AECs, supplemented GM-CSF did not affect mTORC1 activity, and the mean phospho-p70S6K/p70S6K ratio remained at around 3 (Fig. **4.9 C**).

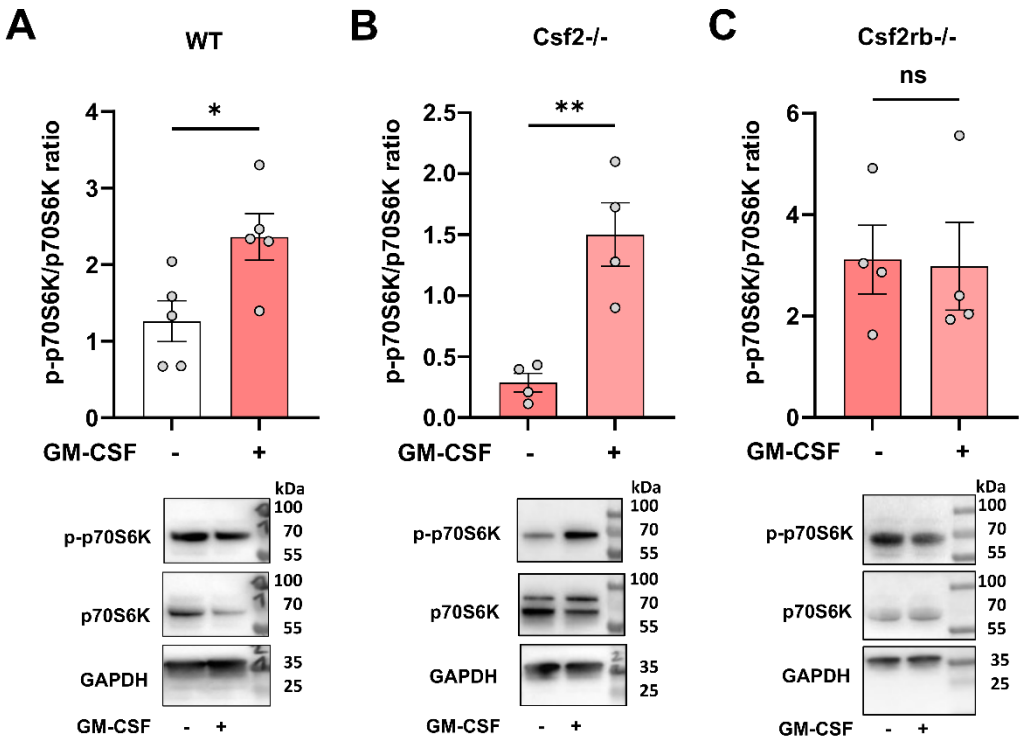

Figure 4.9: Addition of GM-CSF increases mTORC1 activity in IAV-infected murine AECs *ex vivo*. (A-C) mTORC1 activity (indicated by p-p70S6K/p70S6K ratio) in primary murine AECs from **(A)** WT, **(B)** Csf2-/-, and **(C)** Csf2rb-/- mice 24 h after *ex vivo* PR8 IAV infection and recombinant GM-CSF treatment. Representative Western Blot images show the bands of (p-)p70S6K (70 kDa) and GAPDH (37 kDa) (n=3-4). Probabilities were determined using t test. Graphs show means ± SEM; *=p<0.05; **=p<0.005.

Western Blot results obtained from *ex vivo* treated murine AECs illustrate that GM-CSF regulates the AMPK-mTORC1 pathway in AECIIs by antagonizing AMPK, thereby licensing mTORC1 activity following IAV infection *ex vivo* (Fig. **4.8 and 4.9**). To further validate these findings in an *in vivo* context, AECIIs were isolated from IAV-infected mice at 4 dpi. This specific timepoint was selected for *in vivo* analysis of the AMPK-mTORC1 signaling pathway due to previous findings indicating an increase in GM-CSF gene expression at 4 dpi (see Chapter 4.1). WT (500 FFU) and Csf2-/- (100 FFU) mice were infected, and AECIIs were isolated at 4 dpi by FACS (Figure **4.10 A**). AECIIs were identified as $EpCAM^{low}Lysotracker^{+}$, with exclusion of cell debris and doublets, and isolation of only living ($Sytox^{-}$) cells (Figure **4.10 B**).

The phospho-AMPK/AMPK ratios were significantly elevated in AECIIs isolated from Csf2rb-/- (mean 4.39 ± 0.76) and Csf2-/- (mean 4.21 ± 1.02) mice compared to WT (0.99 ± 0.07) at 4 dpi (Figure **4.10 C and D**). Correspondingly, a decrease in mTORC1 activity was observed in AECIIs from Csf2rb-/- (mean 0.25 ± 0.06) and Csf2-/- (mean 0.11 ± 0.04) mice compared to WT (mean 1.06 ± 0.11) at 4 dpi (Figure **4.10 E and F**). These results collectively confirm the role of GM-CSF in inhibiting AMPK activity and thereby licencing mTORC1 signaling in alveolar epithelial stem cells *in vivo*.

In the following experiments, the aim was to investigate the impact of GM-CSF on mTORC1 downstream effects following IAV infection. It is established that activated mTORC1 promotes the expression of the cell cycle-related gene *cMyc*.[261–264] cMyc functions as a transcription factor that interacts with its partner protein MAX, forming a heterodimeric complex.[265] Its primary role involves promoting cell growth and proliferation. However, cMyc is also associated with loss of differentiation and apoptosis.[265]

To examine whether the presence of GM-CSF influences the expression of the cell cycle-related gene *cMyc*, WT (500 FFU) and Csf2-/- (100 FFU) mice were infected with adjusted virus doses. At 4, 7, and 10 dpi, AECIIs and BASCs were isolated from the harvested lungs using FACS (Fig. **4.10 A**). The isolated AECIIs and BASCs were separated from cell debris and doublets (Fig. **4.10 B**). Living ($Sytox^{-}$) AECIIs were defined as $CD31^{-}CD45^{-}EpCAM^{low}Lysotracker^{+}$, while BASCs were identified as $CD31^{-}CD45^{-}EpCAM^{high}CD24^{low}$ $Sca\text{-}1^{+}Lysotracker^{+}$. Subsequently, the expression levels of the *cMyc* gene were assessed in the isolated AECIIs and BASCs using qPCR.

At 4 and 10 dpi, the expression of the *cMyc* gene was elevated in AECIIs from WT mice, but not in those from Csf2-/- (Fig. **4.10 G**). At 4 dpi, *cMyc* gene expression in WT AECIIs showed a significant increase with a fold change of 1.41 ± 0.1 compared to the mock-treated control. Conversely, in Csf2-/- AECIIs isolated at 4 dpi, *cMyc* expression did not significantly differ from the mock-treated control, with a fold change of 1 ± 0.32. Similarly, at 10 dpi, expression in WT AECIIs was significantly elevated with a fold induction of 1.97 ± 0.32, whereas in Csf2-/- AECIIs, the *cMyc* gene expression remained at the same level as in the mock-treated control, with a fold change of 1.12 ± 0.16.

In BASCs from WT mice, *cMyc* expression was upregulated at 7 and 10 dpi, whereas in BASCs from Csf2-/- mice, expression was not induced after IAV infection (Fig. **4.10 H**). In WT BASCs isolated at 7 dpi, *cMyc* expression increased by 3.49-fold (± 0.43) compared to the mock control. However, in Csf2-/- BASCs, the increase in expression was only 1.49-fold (± 0.14) and not significantly elevated compared to the mock control. Similarly, at 10 dpi, *cMyc* expression was upregulated by 4.24-fold (± 0.44) in infected WT BASCs compared to mock control, while the increase in Csf2-/- BASCs was not significant, with a fold change of 1.22 ± 0.2 compared to mock. These findings indicate that the presence of GM-CSF after IAV infection leads to increased expression of the cell cycle-related gene *cMyc*, a downstream effector gene of mTORC1.

The findings of this investigation suggest that during IAV infection, GM-CSF suppresses AMPK, which in turn activates mTORC1 in alveolar epithelial stem cells (Fig. **4.10 I**). In brief, IAV infection causes cell stress in AECIIs and BASCs which increases the AMP/ADP:ATP ratio to activate AMPK.[63,136,137] According to literature, this results in a cellular reprogramming where catabolic pathways are upregulated and anabolic processes are reduced.[63,136,137] GM-CSF that is released between 4 and 7 dpi by AECIIs and BASCs antagonizes AMPK activation and thereby licences mTORC1 signaling, allowing anabolic processes as evidenced by proliferation genes such as *Ccnd1* (Fig. **4.6 D**) and c*Myc* (Fig. **4.10 G and H**), essential for restoration of the alveolar epithelial barrier.

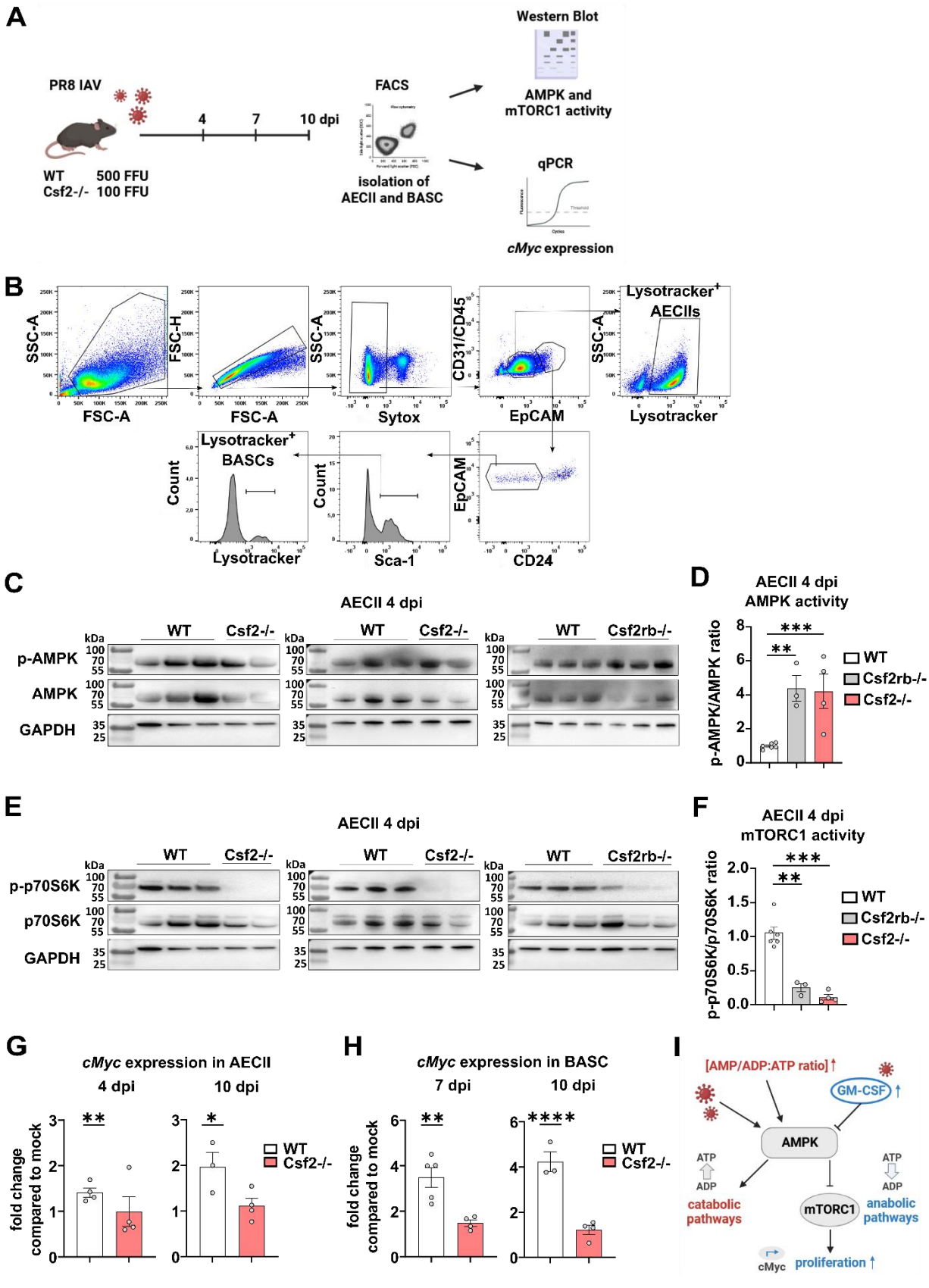
A
PR8 IAV
4
7
10 dpi
WT 500 FFU
Csf2-/- 100 FFU
FACS
isolation of AECII and BASC
Western Blot
AMPK and mTORC1 activity
qPCR
cMyc expression
B
SSC-A
FSC-A
FSC-H
Sytox
CD31/CD45
EpCAM
Lysotracker+ AECIIs
Lysotracker
Lysotracker+ BASCs
Count
Sca-1
CD24
C
AECII 4 dpi
WT
Csf2-/-
Csf2rb-/-
kDa
p-AMPK
AMPK
GAPDH
D
AECII 4 dpi
AMPK activity
p-AMPK/AMPK ratio
WT
Csf2rb-/-
Csf2-/-
E
AECII 4 dpi
p-p70S6K
p70S6K
GAPDH
F
AECII 4 dpi
mTORC1 activity
p-p70S6K/p70S6K ratio
G
cMyc expression in AECII
4 dpi
10 dpi
fold change compared to mock
H
cMyc expression in BASC
7 dpi
10 dpi
I
[AMP/ADP:ATP ratio]↑
GM-CSF ↑
AMPK
ATP
ADP
catabolic pathways
mTORC1
anabolic pathways
cMyc
proliferation ↑

Figure 4.10: GM-CSF regulates the AMPK-mTORC1 signaling pathway by antagonizing AMPK, thereby enhancing mTORC1 activity in distal epithelial stem cells following IAV infection *in vivo*. **(A)** Experimental setup: WT and Csf2-/- mice were infected with adjusted PR8 IAV doses. At 4, 7, and 10 dpi, AECIIs and BASCs were isolated from the lung homogenate and utilized for Western Blot to measure the activity of AMPK and mTORC1 or to analyze the expression of *cMyc* by qPCR. Created using BioRender.com. **(B)** Gating strategy for the isolation of living ($Sytox^-$) AECIIs ($CD31^-CD45^-EpCAM^{low}Lysotracker^+$) and BASCs ($CD31^-CD45^-EpCAM^{high}CD24^{low}Sca1^+Lysotracker^+$) from lung homogenate of WT or Csf2-/- mice. Cell debris and cell doublets were excluded. **(C)** Western Blot with AECIIs from WT, Csf2-/-, and Csf2rb-/- mice isolated at 4 dpi. Representative images are depicting (p-)AMPK at 62 kDa and GAPDH at 37 kDa. **(D)** AMPK activity (p-AMPK/AMPK ratio) in AECIIs from WT, Csf2-/-, and Csf2rb-/- mice at 4 dpi (n=3-6). Probabilities were determined using one-way ANOVA. **(E)** Western Blot with AECIIs from WT, Csf2-/-, and Csf2rb-/- mice isolated at 4 dpi. Representative images are depicting (p-)p70S6K (70 kDa) and GAPDH (37 kDa). **(F)** mTORC1 activity (p-p70S6K/p70S6K ratio) in AECIIs from WT, Csf2-/-, and Csf2rb-/- mice at 4 dpi (n=3-6). Probabilities were determined using one-way ANOVA. **(G)** *cMyc* gene expression in AECIIs from WT and Csf2-/- mice at 4 and 10 dpi. Fold change compared to mock is shown (n=3-5). Statistical significance was calculated with a t-test. **(H)** *cMyc* gene expression in BASCs from WT and Csf2-/- mice at 7 and 10 dpi. Fold change compared to mock is shown (n=3-5). Statistical significance was calculated with a t-test. **(I)** Scheme of GM-CSF-regulated AMPK-mTORC1 signaling pathway. Graphs show means ± SEM; *=p<0.05; **=p<0.005; ***=p<0.001; ****=p<0.0001.

In the subsequent experiments, the goal was to confirm the GM-CSF-mediated modulation of the AMPK-mTORC1 signaling pathway in human AECs. Human AECs were infected with PR8 IAV at MOI 1, and recombinant human GM-CSF at a concentration of 100 ng/ml was supplemented to the medium (Fig. **4.11 A**).

Upon IAV infection, the p-AMPK/AMPK ratio was increased to 2 ± 0.27, but this increase was significantly attenuated by the addition of GM-CSF, reducing the ratio to 0.57 ± 0.12 (Fig. **4.11 B**). Notably, in the mock-treated condition, the addition of GM-CSF did not significantly alter AMPK activity, with the p-AMPK/AMPK ratio remaining at 1.2 ± 0.27. Regarding mTORC1 activity, in the infected condition, GM-CSF supplementation significantly increased the p-p70S6K/p70S6K ratio to a mean of 2.36 ± 0.32 compared to 1.31 ± 0.29 in the infected condition without GM-CSF (Fig. **4.11 C**). Conversely, in the mock-treated samples, the p-p70S6K/p70S6K ratio remained unchanged at 0.97 ± 0.1 following GM-CSF treatment.

These results suggest that GM-CSF antagonizes AMPK and consequently activates mTORC1 in both mouse and human distal alveolar epithelial progenitor cells during IAV infection.

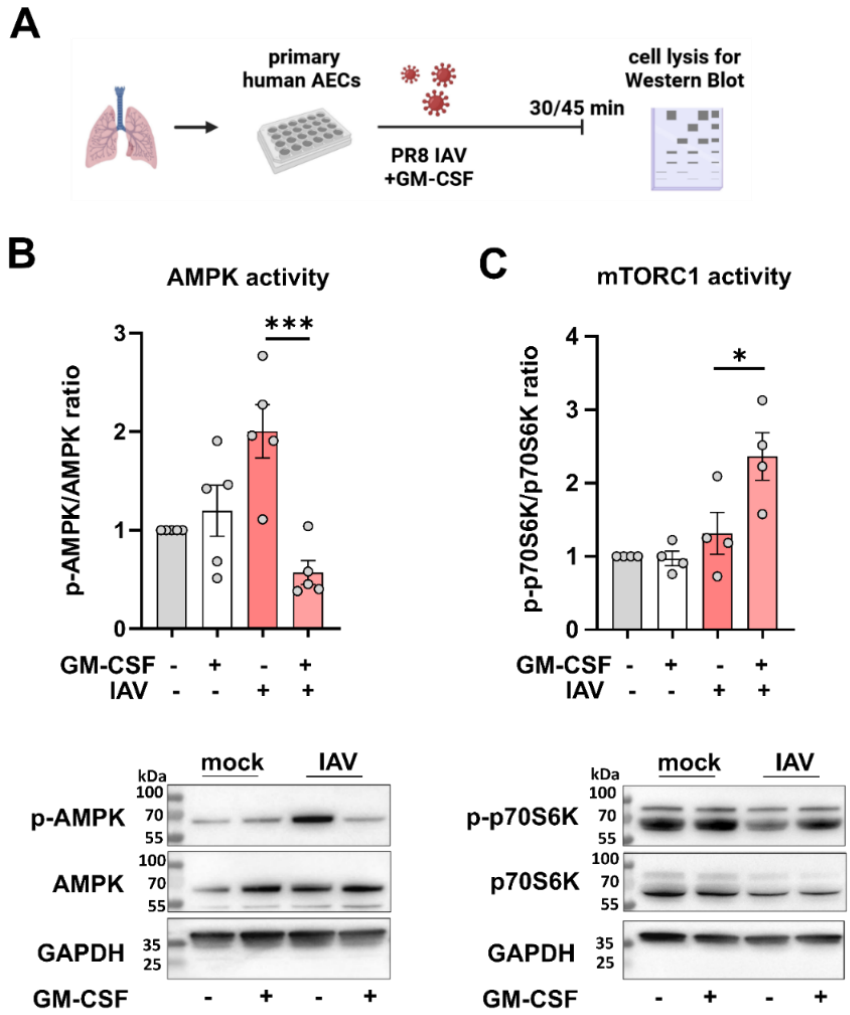

Figure 4.11: GM-CSF inhibits AMPK and licenses downstream mTORC1 activity in human AECs upon IAV infection *ex vivo*. (A) Experimental setup: Primary human AECs were infected with PR8 IAV at MOI 1, and recombinant human GM-CSF (100 ng/ml) was supplemented to the medium. After 45 min, human AECs were lysed to determine the p-AMPK/AMPK ratio, indicating AMPK activity, and after 30 min, cells were lysed to measure the p-p70S6K/p70S6K ratio, indicating mTORC1 activity by utilizing the cell lysates for Western Blot analysis. Created using BioRender.com. **(B-C)** Activity of **(B)** AMPK (p-AMPK/AMPK ratio) and **(C)** mTORC1 (p-p70S6K/p70S6K) in human AECs *ex vivo* upon IAV infection and treatment with recombinant human GM-CSF. Statistics were determined using one-way ANOVA. Graphs show means ± SEM; *=p<0.05; ***=p<0.001.

4.5 Development of BALOs and alveolospheres is affected by modulation of the AMPK-mTORC1 signaling pathway

Thus far, it was shown that GM-CSF orchestrates the AMPK-mTORC1 signaling cascade, leading to augmented cell proliferation within distal alveolar epithelial stem cells. Subsequently, the aim was to gain more insight into the effects of AMPK or mTORC1 modulation on the capability of AECIIs and BASCs for proliferation and differentiation. *Ex vivo* BALO and alveolosphere models were used to elucidate how interventions with GM-CSF and AMPK or mTORC1 modulators impact the organoid formation, alveolarization, and AECII abundance. Previous findings emphasize the dependence of BALO development on GM-CSF release (see chapter 4.3). Now, the objective was to probe the precise effects of GM-CSF-mediated regulation of the AMPK-mTORC1 signaling axis in BALOs.

For BALO generation, BASCs and rMCs were isolated from adult WT mice by FACS and co-cultured in Matrigel (see chapter 4.3).[184] Subsequently, treatments with AMPK activator AICAR (0.5 mM) and AMPK inhibitor Compound C (1 µM) were administered from day 10 to 21 of BALO culture (Fig. **4.12 A**). To determine the appropriate concentrations of AICAR and Compound C for organoid culture treatments, previous literature was used as a reference.[63] However, the concentrations reported in previous studies were reduced and optimized specifically for organoid cultures to avoid cytotoxic effects that could hinder organoid development. At day 21 of culture, measurements of the OFE and alveolar structures were conducted to assess phenotypic alterations induced by the AMPK modulator treatments.

In cultures treated with AICAR (AMPK activator), the OFE was significantly reduced to 1.08% ± 0.07 compared to the PBS control goup (2.15% ± 0.19) (Fig. **4.12 B and C**). On the contrary, following the treatment with Compound C (AMPK inhibitor), the proportion of BASCs developing into BALOs increased, with a mean value of 2.4% ± 0.15 compared to the DMSO control group (1.63% ± 0.13) (Fig. **4.12 D and E**). These data demonstrate that AMPK activation or inhibition opposingly impacts the capacity of BASCs for organoid formation.

Alveolarization in BALOs is associated with increasing numbers and decreasing size of alveoli.[184] To assess the alveolar size in BALOs treated with AMPK modulators, immunofluorescence staining for ProSPC (AECII marker), Cav-1 (AECI marker), and DAPI (nuclear staining) was performed (Fig. **4.12 F**). Z-stack images were acquired

using confocal microscopy, and the perimeter of the alveolar lumen was quantified. Following AICAR treatment, the mean perimeter of the alveolar lumen was increased to 81.41 µm ± 3.03 compared to the PBS control (59.71 µm ± 3.78) (Fig. **4.12 G**). Conversely, in Compound C-treated BALOs, the mean perimeter of luminal structures (54.32 µm ± 2.93) was reduced compared to the DMSO-treated control group (66.43 µm ± 4.46) (Fig. **4.12 H**). These findings indicate that AMPK activation or inhibition induces increase or decrease in BALO formation in general, as well as in alveolarization within single BALOs, respectively.

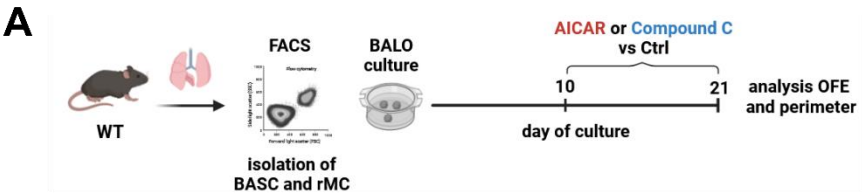
A
WT
FACS
isolation of
BASC and rMC
BALO
culture
AICAR or Compound C
vs Ctrl
10
21
day of culture
analysis OFE
and perimeter

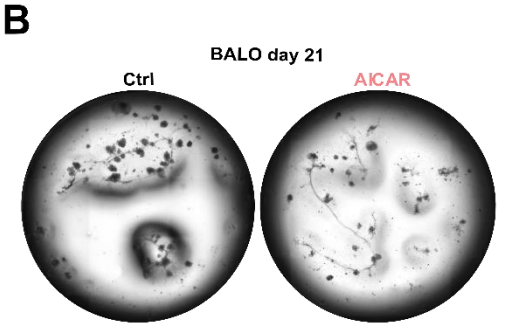
B
BALO day 21
Ctrl
AICAR

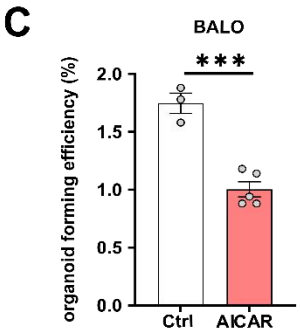
C
BALO
***
organoid forming efficiency (%)
2.0
1.5
1.0
0.5
0.0
Ctrl
AICAR

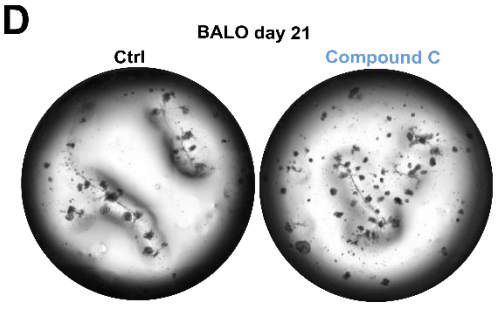
D
BALO day 21
Ctrl
Compound C

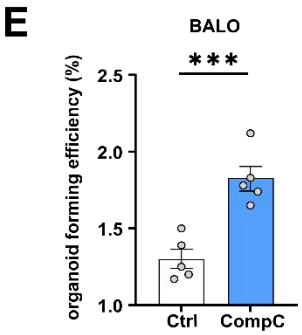
E
BALO
***
organoid forming efficiency (%)
2.5
2.0
1.5
1.0
Ctrl
CompC

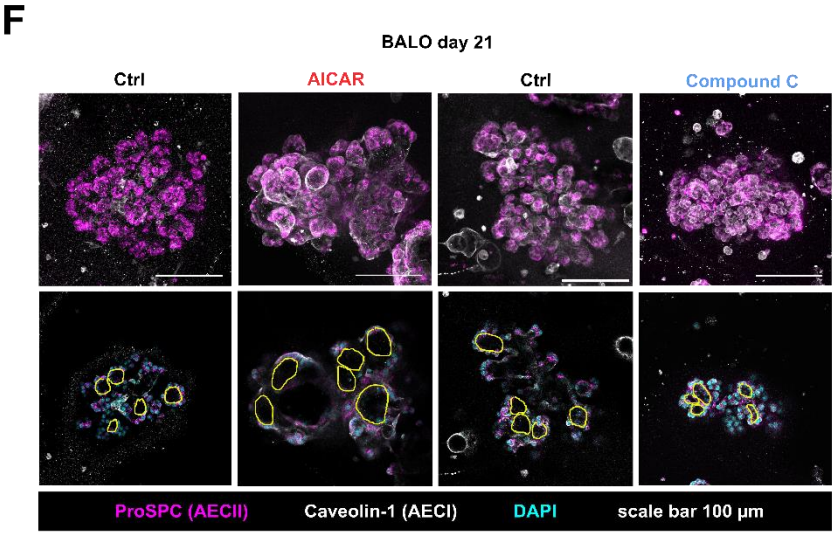
F
BALO day 21
Ctrl
AICAR
Ctrl
Compound C
ProSPC (AECII)
Caveolin-1 (AECI)
DAPI
scale bar 100 µm

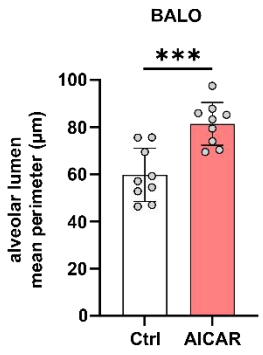
G
BALO
***
alveolar lumen
mean perimeter (µm)
100
80
60
40
20
0
Ctrl
AICAR

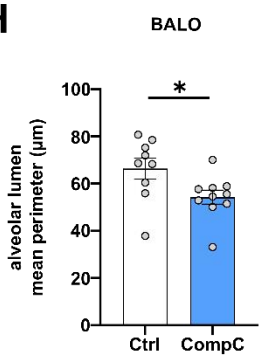
H
BALO
*
alveolar lumen
mean perimeter (µm)
100
80
60
40
20
0
Ctrl
CompC

Figure 4.12: AMPK activator treatment reduces, and AMPK inhibitor treatment enhances BALO formation and affects alveolarization. (A) Experimental setup: BALO cultures were generated through co-culture of rMCs and BASCs isolated from WT mice by FACS. At day 10 of culture, treatment with AMPK activator AICAR (0.5 mM) or AMPK inhibitor Compound C (1 µM) was started. At day 21 of culture, the OFE was analyzed, and organoids were stained for ProSPC and Cav-1 to measure the size of the alveolar structures. **(B)** Representative transmission microscopy images of BALO cultures treated with AICAR (0.5 mM) compared to the PBS control group. **(C)** OFE (%) of BALO cultures treated with AICAR vs PBS control from day 10 to 21 of culture (n=3-5). **(D)** Representative transmission microscopy images of BALO cultures treated with Compound C (1 µM) compared to the DMSO control group. **(E)** OFE (%) of BALO cultures treated with Compound C vs DMSO control from day 10 to 21 of culture. **(F)** Representative confocal microscopy images from BALO cultures treated with AICAR vs PBS control or Compound C vs DMSO control from day 10 to 21 of culture. BALOs were stained for ProSPC (AECII marker) and Cav-1 (AECI marker) to depict the alveolar regions. **(G-H)** Mean perimeter of the alveolar lumen measured in BALOs treated with **(G)** AICAR vs PBS control or **(H)** Compound C vs DMSO control. Probabilities were determined using t-test. Graphs show means ± SEM; *=p<0.05; ***=p<0.001.

Since BALO development is impaired in cultures lacking GM-CSF (see Chapter 4.3), the next aim was to determine whether BALO growth could be restored in Csf2-/- cultures through the addition of the AMPK inhibitor Compound C (Fig. **4.13 A**). The objective was to investigate whether Compound C can mimic and replace the function of the absent GM-CSF in Csf2-/- cultures. For BALO generation, rMCs and BASCs were isolated from the lung homogenate of Csf2-/- mice by FACS and co-cultured in Matrigel (see chapter 4.3). The Compound C concentrations were adjusted to the GM-CSF concentrations observed in the supernatant of WT cultures starting with lower concentrations from day 6 to 10, followed by high GM-CSF concentrations from day 10 to 14 reaching up to 100 pg/ml, and again lower concentrations from day 14 to 18 (see Fig. 4.5 C). Hence, BALOs were treated with 0.5 µM Compound C from day 6 to 10, followed by 1 µM from day 10 to 14, and 0.5 µM from day 14 to 18. The OFE was assessed on day 21. In Compound C-treated BALO cultures, the OFE was significantly increased to a mean value of 2.52 ± 0.17 compared to the DMSO control group (1.65 ± 0.14) (Fig. **4.13 B and C**). These results suggest that AMPK inhibitor treatment can substitute for GM-CSF and enhance the organoid formation capacity of BASCs in Csf2-/- BALO cultures.

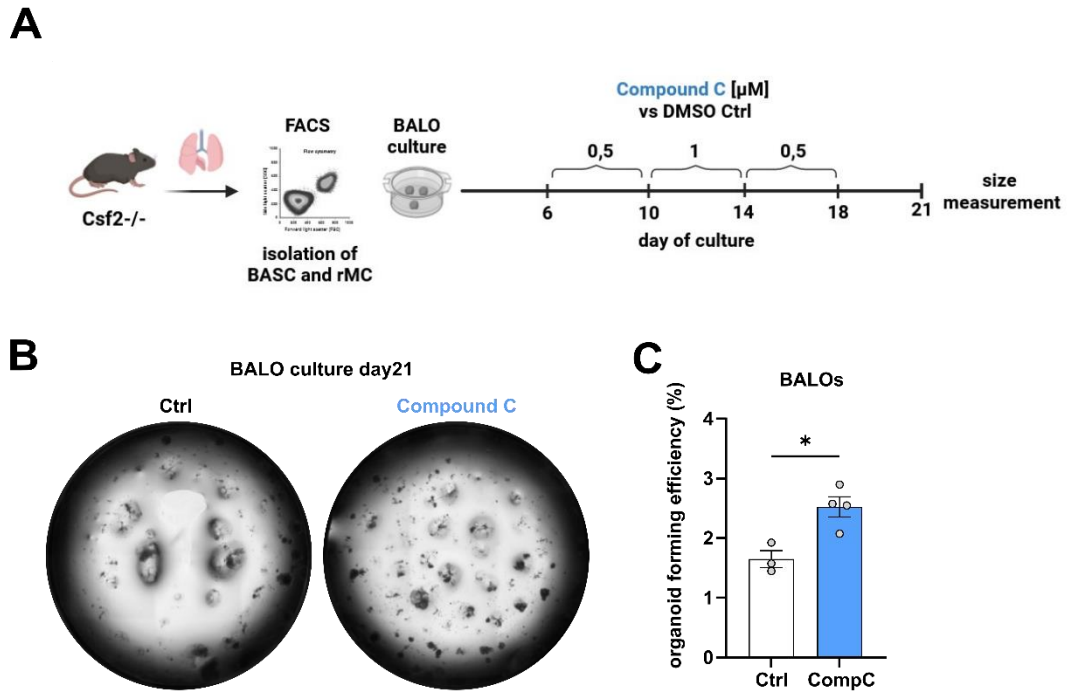

Figure 4.13: AMPK inhibition increases organoid forming capacity of BASCs in Csf2-/- BALO cultures. (A) Experimental setup: BALOs were generated by the co-culture of rMCs and BASCs isolated from the lung homogenate of Csf2-/- mice. Compound C treatment (vs DMSO control) was done in a concentration of 0.5 µM from day 6 to 10, followed by 1 µM from day 10 to 14, and 0.5 µM from day 14 to 18. The OFE was analyzed at day 21. **(B)** Representative transmission microscopy pictures of the whole well and **(C)** the OFE of Csf2-/- BALO cultures treated with Compound C vs DMSO control. Probability was determined using t-test. Graph shows mean ± SEM; *=p<0.05.

In the next step, the effect of mTORC1 activator treatment on BALO development was analyzed. It was investigated whether treatment with mTORC1 activator MHY1485 could compensate for the absence of GM-CSF in Csf2-/- BALOs. To assess this, organoid cultures were established from rMCs and BASCs isolated from Csf2-/- mice by FACS (see Chapter 4.3). These Csf2-/- BALO cultures were treated with mTORC1 activator MHY1485 at a concentration of 0.5 µM from day 6 to 10, followed by 1 µM from day 10 to 14, and 0.5 µM from day 14 to 18 (Fig. **4.14 A**). Optimal concentrations of MHY1485 were validated to avoid cytotoxic effects. On day 21 of culture, the size of the (bronchio)alveolar lung organoids was measured.

The results showed an increase in the size of Csf2-/- BALOs treated with the mTORC1 activator compared to the DMSO control group at day 21 of culture (Fig. **4.14 B and C**). Specifically, the median area was larger following MHY1485 treatment

(14,085 µm^2) compared to the DMSO control (11,507 µm^2). Additionally, the median perimeter increased from 418 µm in the DMSO control group to 467.6 µm in the MHY1485-treated group. These findings suggest that mTORC1 activator treatment can compensate for the absence of GM-CSF in the SN of Csf2-/- cultures and promote BALO growth.

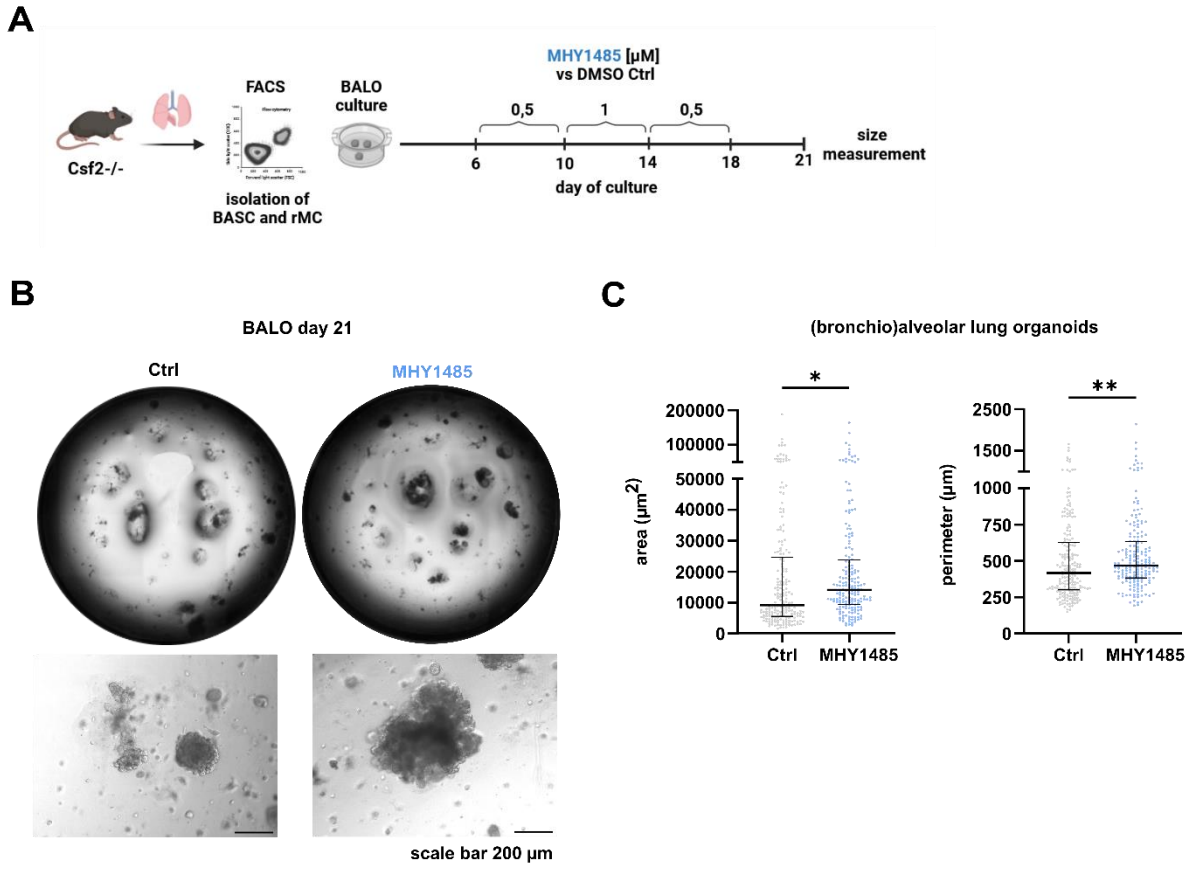

Figure 4.14: mTORC1 activator treatment restores the capacity for BALO formation and growth in Csf2-/- cultures. (A) Experimental setup: Csf2-/- BALOs were generated by the co-culture of rMCs and BASCs isolated from the lung homogenate of Csf2-/- mice by FACS. The mTORC1 activator (MHY1485) treatment was done in a concentration of 0.5 µM from day 6 to 10, followed by 1 µM from day 10 to 14, and 0.5 µM from day 14 to 18. BALO size was measured at day 21 of culture. **(B)** Representative transmission microscopy images (scale bar 200 µm) and **(C)** area and perimeter of BALOs at day 21 of culture after MHY1485 or DMSO control treatment. Graphs show medians with interquartile ranges. Probabilities were determined using Mann-Whitney test; *=p<0.05; **=p<0.005.

In the following steps, immunofluorescence stainings were employed to investigate whether GM-CSF activates and consequently inhibits mTORC1 in AECIIs present in BALOs. Cultures were treated with AMPK activator AICAR or AMPK inhibitor Compound C from day 10 to 21 of culture. Subsequently, the organoids were stained for ProSPC (AECII marker) to determine the amount of AECIIs. Confocal microscopy z-stack images were acquired, and the percentage of ProSPC$^+$ area or the mean fluorescence intensity (MFI) of ProSPC per organoid were analyzed, indicating the amount of AECIIs per BALO (Fig. **4.15 A**).

In AICAR-treated BALOs, the MFI of ProSPC (4.7e+06 ± 0.837e+06) was reduced compared to the PBS-treated control (9.6e+06 ± 1.1e+06) (Fig. **4.15 B**). Conversely, Compound C treatment increased the amount of ProSPC$^+$ area in BALOs (70.47% ± 3.83) compared to the DMSO control (37.84% ± 3.7) (Fig. **4.15 C**). These findings indicate that AMPK inhibition enhances, while AMPK activation reduces, the amount of AECIIs in BALOs.

In the next experiment, WT BALO cultures were treated with 100 ng/ml exogenous GM-CSF from day 6 to 12 of culture. The organoids were then stained for ProSPC and phospho-acetyl coenzyme A carboxylase (phospho-ACC), a marker for AMPK activity. ACC is phosphorylated by AMPK, leading to its inactivation, which is crucial in regulating fatty acid oxidation.[266] Z-stack images were acquired using confocal microscopy (Fig. **4.15 D**), and the amount of ProSPC$^+$ area per BALO (Fig. **4.15 E**), and the MFI of phospho-ACC within the ProSPC$^+$ area (Fig. **4.15 F**) was determined. The amount of ProSPC$^+$ area per BALO increased from 56.58% ± 5 in the PBS control group to 73.23% ± 4.61 in the GM-CSF-treated cultures (Fig. **4.15 E**). Furthermore, the MFI of phospho-ACC in the ProSPC$^+$ area decreased after GM-CSF treatment, with a mean value of 3,208 ± 406.4 compared to the PBS-treated control, which had a mean value of 5,441 ± 805.8 (Fig. **4.15 F**). These results demonstrate that the addition of GM-CSF increases the amount of AECIIs while reducing the acitivity of AMPK in AECIIs within BALOs.

To investigate the impact of GM-CSF on mTORC1 activity in AECIIs, BALO cultures were treated with either AMPK activator AICAR or PBS control from day 4 to 8, followed by treatment with GM-CSF or PBS control from day 8 to 12 (Fig. **4.15 G**). In its activated state, mTOR is phosphorylated at several residues, including serine 2448 (S2448).[267] mTOR complex 1 (mTORC1) and complex 2 (mTORC2) are

associated with mTOR phosphorylated at distinct residues, with mTORC1 primarily phosphorylated at S2448.[267] Therefore, IF staining of phospho(S2448)-mTOR was conducted to assess the activity of mTORC1 in AECIIs (ProSPC$^+$ area) within BALOs. Confocal z-stack images were acquired to quantify the MFI of phospho(S2448)-mTOR within the ProSPC$^+$ area (Fig. **4.15 G and H**).

The results revealed that the addition of GM-CSF increased the MFI of phospho(S2448)-mTOR in AECIIs within BALOs in both the AICAR-treated and PBS-treated control group (Fig. **4.15 H**). In the PBS control group, the MFI of phospho(S2448)-mTOR in the ProSPC$^+$ area increased from a mean value of 4,490 ± 816 to 7,666 ± 1,104 upon GM-CSF treatment. Conversely, in BALO cultures pre-treated with AICAR, the MFI of phospho(S2448)-mTOR in the ProSPC$^+$ area decreased to 1,847 ± 460 at day 12. However, in AICAR pre-treated BALOs, GM-CSF addition from day 8 to 12 resulted in an increased MFI of phospho(S2448)-mTOR within the ProSPC$^+$ area, with a mean value of 5,162 ± 750. Overall, these findings indicate that GM-CSF can reverse the effect of AMPK activator treatment and enhance the activity of mTORC1 in AECIIs within BALOs.

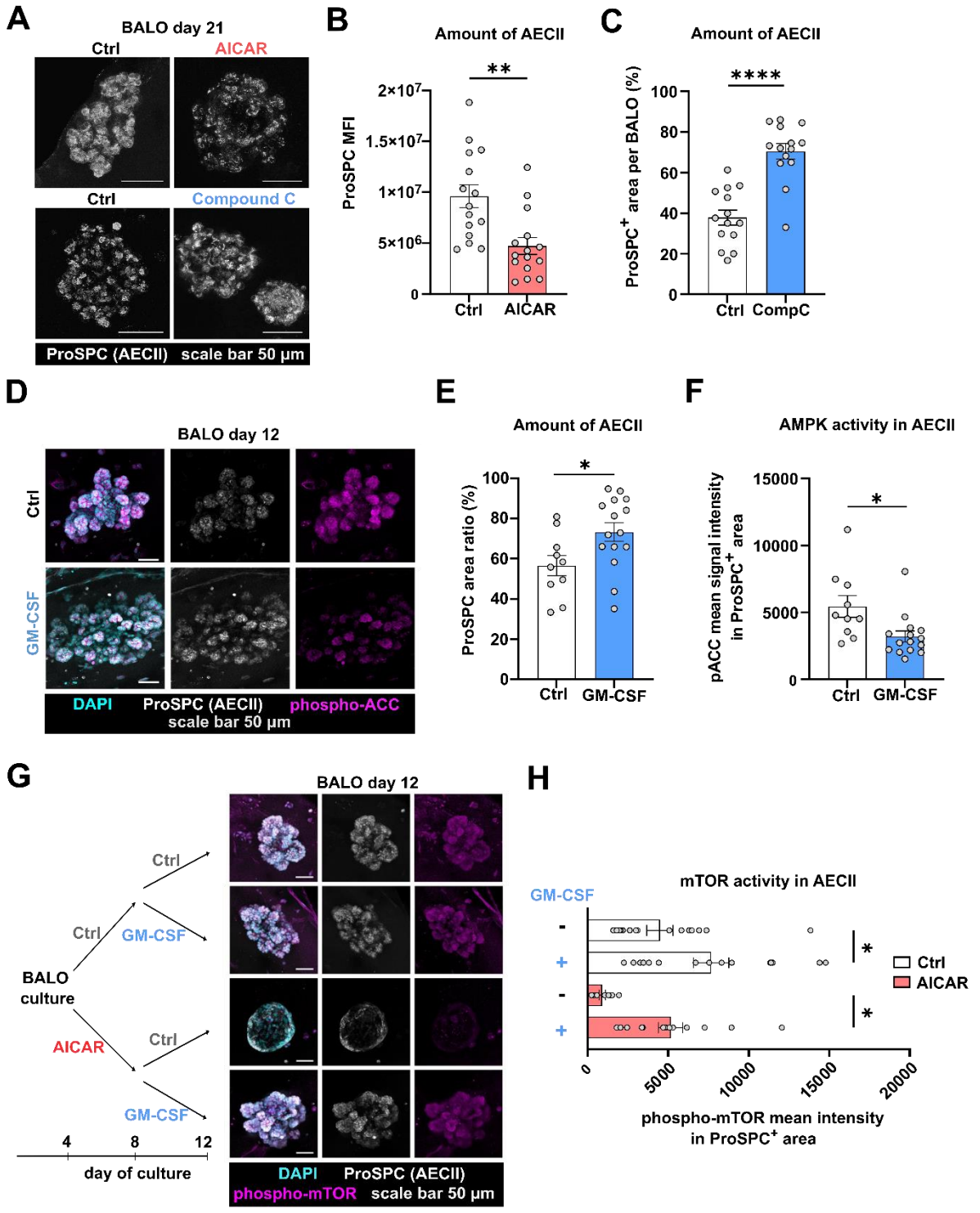

Figure 4.15: GM-CSF antagonizes AMPK, which activates mTORC1, leading to an increased number of AECIIs in BALOs. (A) Representative confocal microscopy images of BALOs treated with AICAR or Compound C from day 10 to 21 of culture stained for ProSPC. Scale bar represents 50 µm. **(B-C)** Percentage of ProSPC⁺ area (AECII) in BALOs treated with **(B)** AMPK activator (AICAR 0.5 mM) vs PBS control or treated with **(C)** AMPK inhibitor Compound C (1 µM) vs DMSO control (n=3). **(D)** Representative confocal images of BALOs treated with GM-CSF (100 ng/ml) vs PBS control from day 6 to 12 of culture stained for ProSPC (AECII marker) and p-ACC (indicating AMPK activity). **(E-F)**

BALOs treated with GM-CSF vs PBS control were analyzed for **(E)** the percentage of ProSPC$^+$ area (AECII) and **(F)** p-ACC activity (MFI) in AECIIs (ProSPC$^+$ area) (n=2-3). **(G)** Experimental setup: BALOs were treated with AMPK activator (AICAR 0.5 mM) vs PBS control from day 4 to 8 of culture. Subsequently, BALOs were treated with recombinant GM-CSF (100 ng/ml) from day 8 to 12 (vs PBS control). Representative images of BALOs stained for ProSPC (AECII marker) and phospho(S2448)-mTOR (indicating mTORC1 activity) are shown. **(H)** mTORC1 activity (phospho(S2448)-mTOR mean signal intensity) in AECIIs (ProSPC$^+$ area) in BALOs treated with AMPK activator vs PBS control from day 4 to 8 followed by recombinant GM-CSF vs PBS control treatment from day 8 to 12 (n=4). Probabilities were determined using t-test. Graphs show means ± SEM; *=p<0.05; **=p<0.005; ****=p<0.0001.

In subsequent experiments, the effects of AMPK or mTORC1 activator or inhibitor treatments on alveolosphere development were investigated. Alveolospheres, originating from a specific subset of AECIIs with differentiation potential, form compact saccular structures that model the alveolar epithelial compartment of the lung.[184] The aim was to assess how the treatment with AMPK or mTORC1 activator or inhibitor affects the stem cell potential of AECIIs for organoid formation.

Alveolospheres were generated following a protocol from our group recently published by Zabihi *et al.* (2024).[268] AECs and rMCs were isolated from leukocyte/endothelial cell-depleted lung homogenate of adult WT mice by FACS. In the gating strategy, cell debris and cell doublets were excluded. AECIIs were enriched by isolating the EpCAM^{low} AEC population, while rMCs were defined as EpCAM$^-$Sca-1$^+$. These cells were co-cultured to facilitate the development of alveolospheres (Fig. **4.16 A**). On day 10 of culture, treatments with the AMPK activator AICAR (0,5 mM) or the AMPK inhibitor Compound C (1 µM), as well as the mTORC1 activator MHY1485 (1 µM) or the mTORC1 inhibitor Rapamycin (0.5 nM), were initiated. On day 21 of culture, the OFE and the size (perimeter) of alveolospheres were determined.

In the AICAR-treated alveolosphere cultures, the OFE was significantly decreased to a mean of 0.49% ± 0.1 compared to the PBS control group (mean 1.07% ± 0.09) (Fig. **4.16 B and C**). Conversely, treatment with AMPK inhibitor Compound C significantly increased the OFE from 0.81% ± 0.09 in the DMSO control to 1.62% ± 0.19 upon Compound C treatment (Fig. **4.16 D and E**).

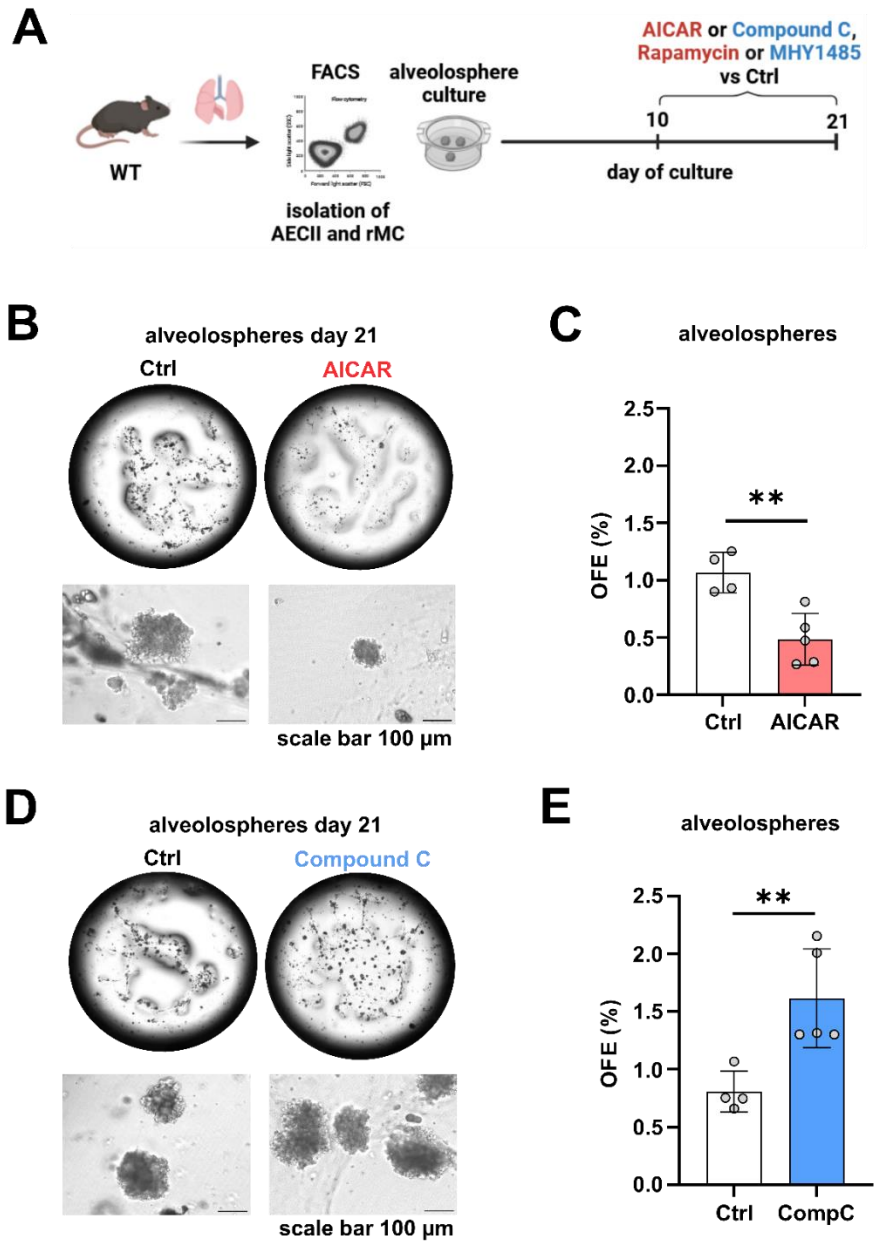

Figure 4.16: AMPK inhibition enhances, and AMPK activation decreases the capacity of AECIIs for organoid formation. (A) Scheme of experimental setup: AECs and rMCs were isolated from lung homogenate of adult WT mice for the generation of alveolosphere. Organoid cultures were treated with AMPK activator AICAR (0.5 mM), AMPK inhibitor Compound C (1 µM), mTORC1 inhibitor Rapamycin (0.5 nM) or mTORC1 activator MHY1485 (1 µM) vs DMSO or PBS control. The treatments were started at day 10 of culture and the readouts were done at day 21. **(B)** Representative transmission microscopy images of alveolosphere cultures treated with AICAR vs PBS Ctrl from day 10 to 21 of culture. Scale bars represent 100 µm. **(C)** Organoid forming efficiency (OFE) of alveolospheres treated with AICAR vs PBS control. (n=4-5). **(D)** Representative transmission microscopy images of alveolosphere cultures treated with Compound C vs DMSO Ctrl from day 10 to 21 of culture. Scale bars represent 100 µm. **(E)** OFE of alveolospheres treated with Compound C vs DMSO control (n=4-5). Probabilities were determined using t-test. Graphs show means ± SEM; **=p<0.005.

Additionally, the OFE and size of alveolospheres were affected by the treatment with mTORC1 inhibitor Rapamycin (Fig. **4.17**). The OFE decreased from 1.02% ± 0.06 in the DMSO control to 0.65% ± 0.08 after treatment with 0.5 nM of the mTORC1 inhibitor Rapamycin (Fig. **4.17 A and B**). In alveolosphere cultures treated with the mTORC1 activator MHY1485, the OFE (mean 1% ± 0.11) did not further increase compared to the DMSO-treated control, indicating that full proliferation/differentiation potential was reached in this culture conditions. The mean perimeter of alveolospheres was reduced by treatment with the mTORC1 inhibitor Rapamycin at (345 µm ± 5.66) compared to the DMSO control (456 µm ± 12.03) and the MHY1485 treated condition (402.1 µm ± 8.16) (Fig. **4.17 A and C**).

These data demonstrate that AMPK inhibition and mTORC1 activation enhance the stem cell potential of AECIIs for organoid formation, whereas this potential is diminished by AMPK activation and mTORC1 inhibition.

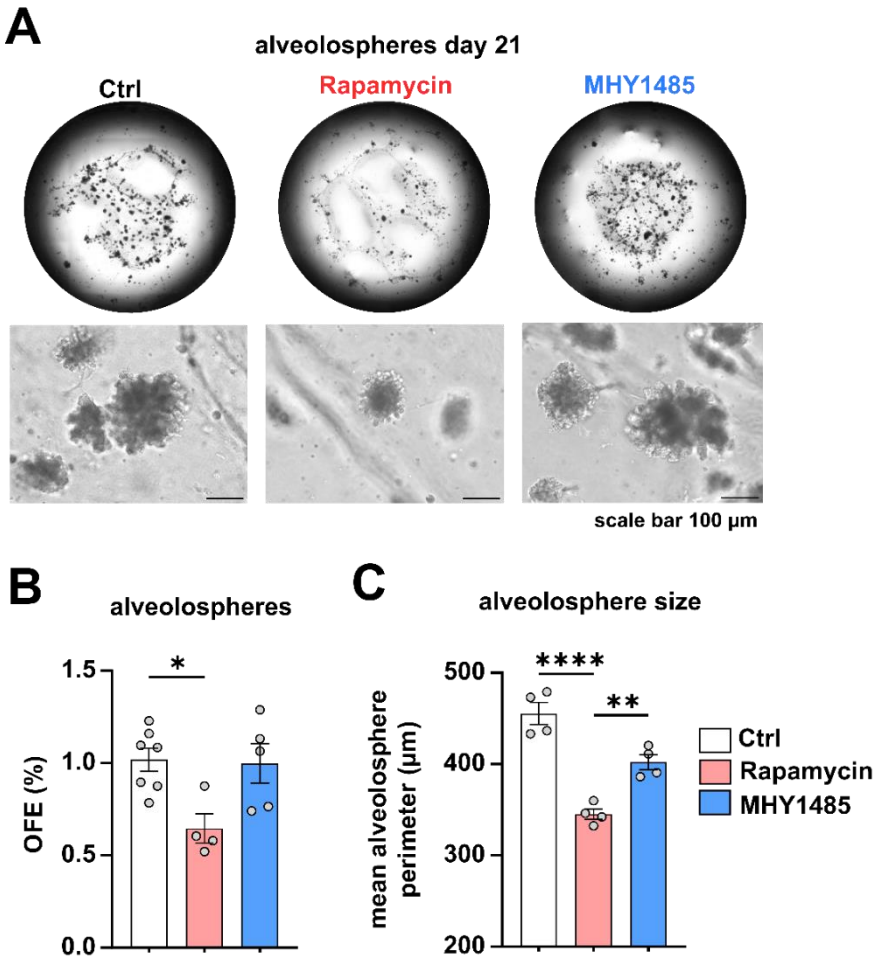

Figure 4.17: mTORC1 inhibitor treatment of alveolosphere cultures reduces OFE and organoid size. (A) Representative transmission microscopy images of alveolosphere cultures treated with mTORC1 inhibitor Rapamycin or mTORC1 activator MHY1485 vs DMSO Ctrl from day 10 to 21 of culture. Scale bars represent 100 µm. **(B)** Organoid forming efficiency (OFE) and **(C)** perimeter of alveolospheres treated with Rapamycin (mTORC1 inhibitor) or MHY1485 (mTORC1 activator) vs DMSO control. Treatment was started at day 10 and readouts were done at day 21 of culture (n=4-7). Probabilities were determined using one-way ANOVA. Graphs show means ± SEM; *=p<0.05; **=p<0.005; ****=p<0.0001.

In addition to the murine alveolosphere and BALO models, confirmation of the previous findings was sought in human alveolospheres to assess whether their development is similarly influenced by modulation of the AMPK-mTORC1 signaling pathway. Human primary AECs and cells of the MRC-5 fibroblast cell line were co-cultured to generate human alveolospheres (Fig. **4.18 A**).[254] The treatment with AMPK activator AICAR (0.5 mM) or AMPK inhibitor Compound C (1 µM) was started on day 21 of culture and the OFE was analyzed on day 28. The OFE was significantly decreased from 1.92% ± 0.13 in the PBS-treated control to 1.06% ± 0.1 in the AICAR-treated cultures (Fig. **4.18 B and C**). Conversely, in Compound C-treated alveolosphere cultures, the OFE increased to 2.13% ± 0.14 compared to the DMSO control group (1.26% ± 0.12) (Fig. **4.18 D and E**). These results indicate that the stem cell capacity of human AECIIs for organoid formation is also affected by AMPK activator and inhibitor treatments.

In summary, these findings reveal that GM-CSF antagonizes AMPK, thereby licensing mTORC1 activation in AECIIs and increasing their abundance in BALOs. Notably, treatment with AMPK inhibitor mimicked the effects of GM-CSF, enhancing organoid development and alveolarization by bolstering the stem cell potential of AECIIs and BASCs.

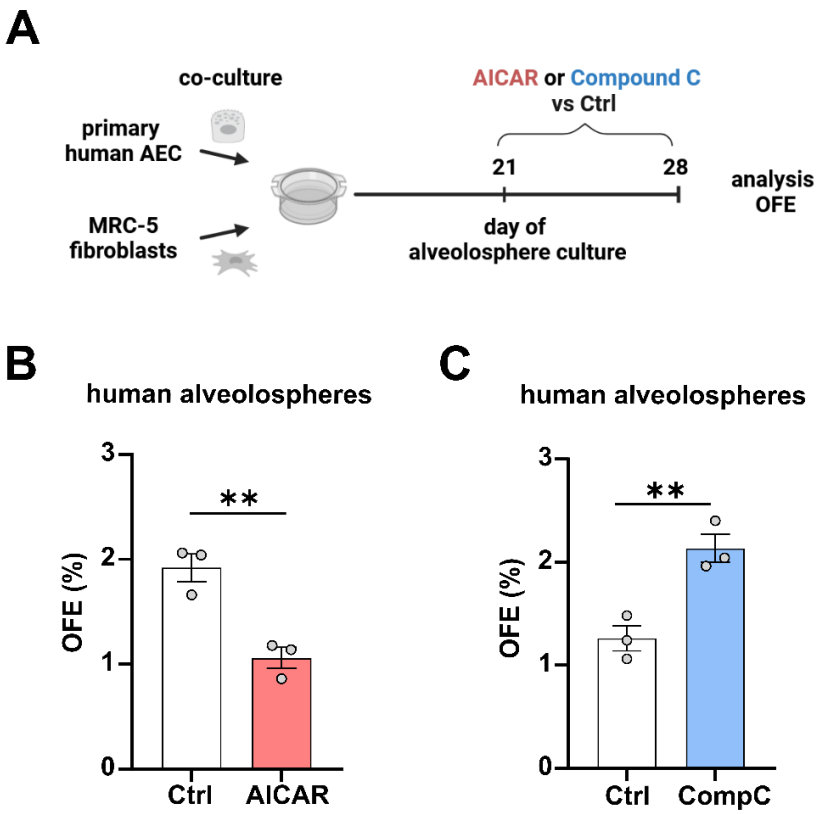

Figure 4.18: AMPK activator treatment reduces, and AMPK inhibitor treatment enhances organoid forming efficiency in human alveolosphere cultures. (A) Experimental setup: For the generation of human alveolospheres, human primary AECs and fibroblasts from the human MRC-5 cell line are co-cultured. The treatment with AMPK activator AICAR (0.5 mM) vs PBS control or AMPK inhibitor Compound C (1 µM) vs DMSO control was started at day 21 of culture. The analysis of the OFE was done at day 28. **(B-C)** OFE of human alveolospheres treated with **(B)** AMPK activator vs PBS control or **(C)** Compound C vs DMSO control (n=3). Probabilities were determined using t-test. Graphs show means ± SEM; **=p<0.005.

4.6 GM-CSF-mediated inhibition of AMPK and activation of downstream mTORC1 has a protective effect and increases AECII and BASC proliferation *in vivo*

After analyzing the effects of AMPK inhibition and downstream activation of mTORC1 on murine and human lung organoid models *ex vivo*, the effects of AMPK activator and inhibitor treatments were examined *in vivo*. WT mice were infected with 500 FFU PR8 IAV and AICAR (500 µg/g bodyweight) or Compound C (20 µg/g bodyweight) was applied i.t. at 3, 5, and 7 dpi (Fig. **4.19 A**). At 7 dpi, the amount of proliferating and apoptotic AECIIs and BASCs was determined by FACS (gating strategy see Fig. 4.3). Moreover, lung sections were prepared at 7 dpi and stained for ProSPC (AECII and BASC marker) and Ki67 (proliferation marker) to analyze the amount of proliferating AECIIs and BASCs. At 10 dpi, the alveolar leakage was measured by FITC albumin application.

In WT mice treated with AICAR, the amount of proliferating AECIIs (mean 6.24% ± 0.4) was significantly decreased compared to the Compound C-treated (20.89% ± 2.02) and control group (15.2% ± 2.26) (Fig. **4.19 B**). Similarly, the amount of proliferating BASCs decreased following AICAR treatment (22.12% ± 1.49) compared to the Compound C-treated group (40.86% ± 5.84). The amount of apoptotic AECIIs significantly increased after AICAR treatment (23.98% ± 3.81) compared to both Compound C-treated cultures (10.69% ± 1.1) and the control (13.73% ± 0.75) (Fig. **4.19 C**). Similar results were found in BASCs: the amount of apoptotic BASCs rose to 27.04% ± 2.04 after AICAR treatment compared to the Compound C-treated group (10.44% ± 1.23) and the control group (16.7% ± 1.25). Additionally, there was a significant difference in the amount of apoptotic BASCs between the Compound C-treated and the control group.

Moreover, lung sections stained for ProSPC (AECII and BASC marker), Ki67 (proliferation marker), and DAPI (nuclear staining) revealed an increase in the amount of AECIIs and BASCs per microscopic field at 7 dpi after treatment with Compound C (77.92 ± 8.6) compared to AICAR (25.63 ± 1.93) and control (41.5 ± 3.13) treatment (Fig. **4.19 D and E**). In addition to that, the amount of proliferating AECIIs and BASCs (ratio $Ki67^{+}ProSPC^{+}/ProSPC^{+}$ cells) was decreased after treatment with AICAR (0.08 ± 0.02) compared to Compound C (0.42 ± 0.1) and control (0.21 ± 0.04) treatment (Fig. **4.19 D and F**).

Consistent with these findings, alveolar leakage at 10 dpi increased after AICAR treatment (0.65 ± 0.09) compared to both the Compound C-treated (0.32 ± 0.1) and control groups (0.31 ± 0.06) (Fig. **4.19 G**).

To investigate whether the GM-CSF-mediated increase in AECII and BASC proliferation can be antagonized by AMPK activator treatment, SPC-GM mice, which exhibit high concentrations of GM-CSF in alveoli, were infected with 2,000 FFU PR8 IAV and intratracheally treated with AICAR (500 µg/g bodyweight) at 3 and 5 dpi.[216] At 7 dpi, the amount of proliferating AECIIs and BASCs was measured (Fig. **4.19 H**). In the AECII population, the percentage of proliferating cells was decreased to 5.7% ± 0.45 with AICAR treatment compared to the control (10.91% ± 1.73) (Fig. **4.19 I**). Similarly, the amount of proliferating BASCs decreased from 24.8% ± 1.87 in the PBS control to 12.47% ± 0.99 after AICAR treatment.

These findings indicate that treatment with the AMPK activator AICAR can counteract the effects induced by GM-CSF. AMPK activation increases apoptosis and reduces proliferation in distal alveolar epithelial stem cells following IAV infection, thereby impairing repair of the alveolar epithelial barrier. Conversely, treatment with the AMPK inhibitor Compound C promotes AECII and BASC proliferation while reducing apoptosis, facilitating alveolar epithelial barrier repair.

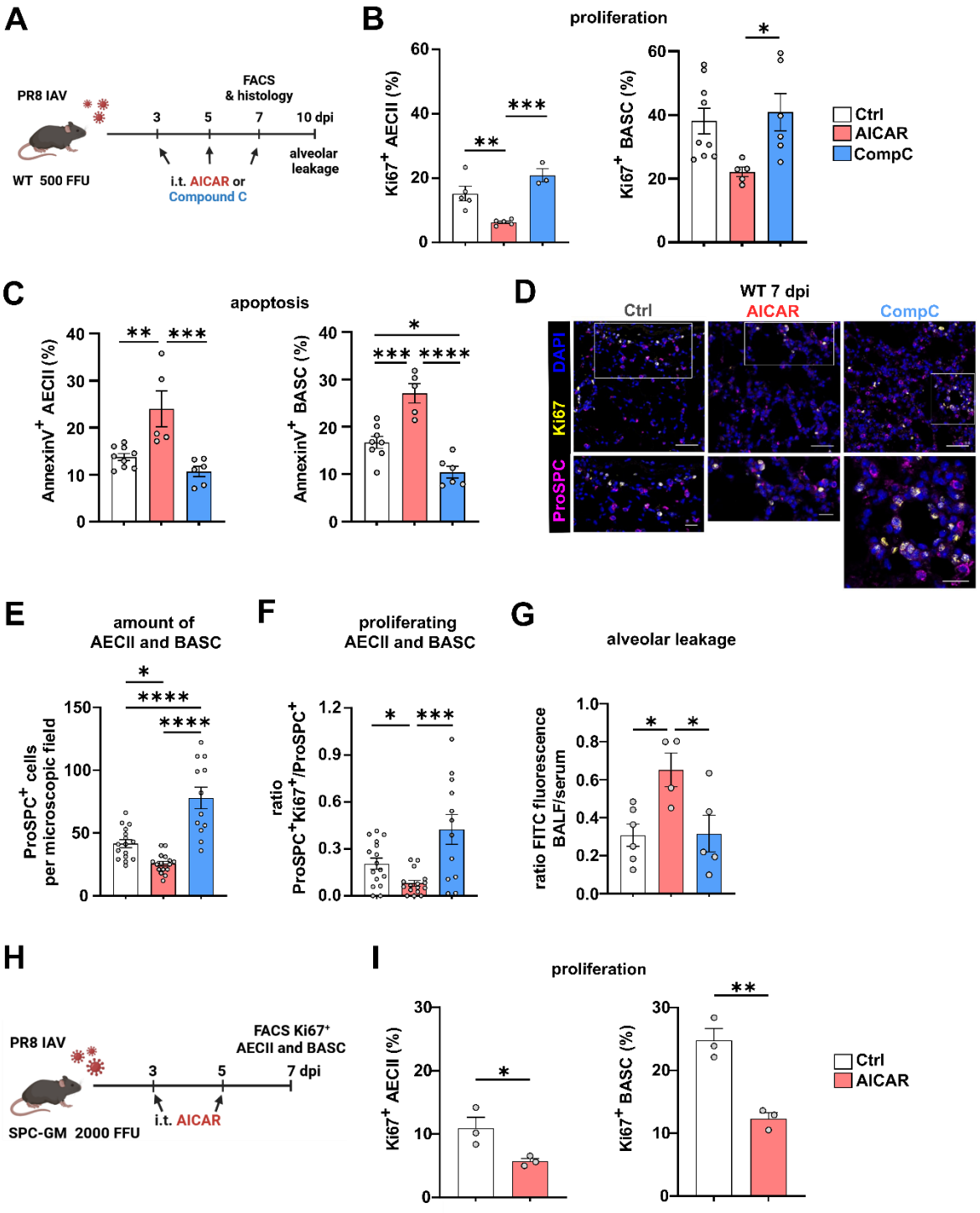

Figure 4.19: AMPK activator treatment suppresses the proliferation of AECIIs and BASCs, while enhancing apoptosis, thereby leading to increased alveolar leakage following IAV infection *in vivo*. (A) Scheme of experimental setup: C57BL/6 WT mice were infected with 500 FFU PR8 IAV. At 3 and 5 dpi AMPK activator AICAR or AMPK inhibitor Compound C vs PBS control was i.t. applied. At 7 dpi, lungs were harvested to analyze the amount of Ki67⁺ and AnnexinV⁺ AECIIs and BASCs by FACS. At 10 dpi, the alveolar leakage was determined. **(B)** Amount of proliferating (Ki67⁺) AECIIs and BASCs at 7 dpi in WT mice treated with AMPK activator AICAR or AMPK inhibitor Compound C vs PBS control. Probabilities were determined using One-way ANOVA. **(C)** Amount of apoptotic

(AnnexinV$^+$) AECIIs and BASCs at 7 dpi in WT mice treated with AMPK activator AICAR or AMPK inhibitor Compound C vs PBS control. Probabilities were determined using One-way ANOVA. **(D)** Representative confocal microscopy images of lung tissue sections collected at 7 dpi, stained for ProSPC (AECII and BASC marker), Ki67 (proliferation marker), and DAPI (nuclear staining). Scale bar represents 50 µm (upper panel) or 20 µm (lower panel). **(E)** The amount of ProSPC$^+$ cells (AECIIs and BASCs) per microscopic field and **(F)** proliferating AECIIs and BASCs (ratio Ki67$^+$ProSPC$^+$ / ProSPC$^+$ cells) were determined. Probabilities were determined using One-way ANOVA. **(G)** Alveolar leakage (ratio FITC albumin in BALF / serum) in WT mice at 10 dpi treated with AMPK activator AICAR or AMPK inhibitor Compound C vs PBS control. Probabilities were determined using One-way ANOVA. **(H)** Experimental setup: SPC-GM mice were infected with 2,000 FFU PR8 IAV. At 3 and 5 dpi AMPK activator AICAR was applied intratracheally. At 7 dpi the amount of proliferating (Ki67$^+$) AECIIs and BASCs was measured. **(I)** Amount of proliferating AECIIs and BASCs at 7 dpi in SPC-GM mice treated with AICAR vs PBS control. Probability was determined using t-test. Graphs show means ± SEM; *=p<0.05; **=p<0.005; ***=p<0.001; ****=p<0.0001.

Finally, the aim was to investigate whether treatment with AMPK inhibitor Compound C can mimick the effects mediated by GM-CSF and rescue alveolar repair in Csf2-/- mice.To achieve this, Csf2-/- mice were infected with 100 FFU PR8 IAV and administered with Compound C (20 µg/g bodyweight) i.t. at 3, 5, and 7 dpi (Fig. **4.20 A**). At 7 dpi, the percentages of proliferating and apoptotic AECIIs and BASCs were quantified. Additionally, the alveolar leakage was determined at 10 dpi.

The administration of AMPK inhibitor led to an increase in the amount of proliferating AECIIs from 10.65% ± 1.75 in the PBS control group to 19.73% ± 2.14 after treatment with Compound C (Fig. **4.20 B**). Similarly, in the BASC population, the percentage of proliferating cells rose from 16.06% ± 1.97 in the PBS control to 32.75% ± 5.39 following Compound C treatment. The amount of apoptotic AECIIs was decreased from 13.4% ± 1.99 in the PBS control to 5.67% ± 0.74 after the Compound C treatment (Fig. **4.20 C**). A reduction in apoptosis was also observed in the BASC population, with the percentage declining from 17.7% ± 3.01 in the PBS-treated control group to 8.12% ± 1.93 post Compound C treatment. Additionally, alveolar leakge at 10 dpi exhibited a significant decrease, with a mean ratio of 0.23 ± 0.03 following Compound C treatment compared to the PBS control (mean ratio 0.44 ± 0.06) (Fig. **4.20 D**).

These data point out that administering the AMPK inhibitor Compound C compensates for the absence of GM-CSF in Csf2-/- mice after IAV infection,

consequently aiding in the restoration of the alveolar epithelial barrier. This effect is achieved through the promotion of AECII and BASC proliferation and the prevention of apoptosis.

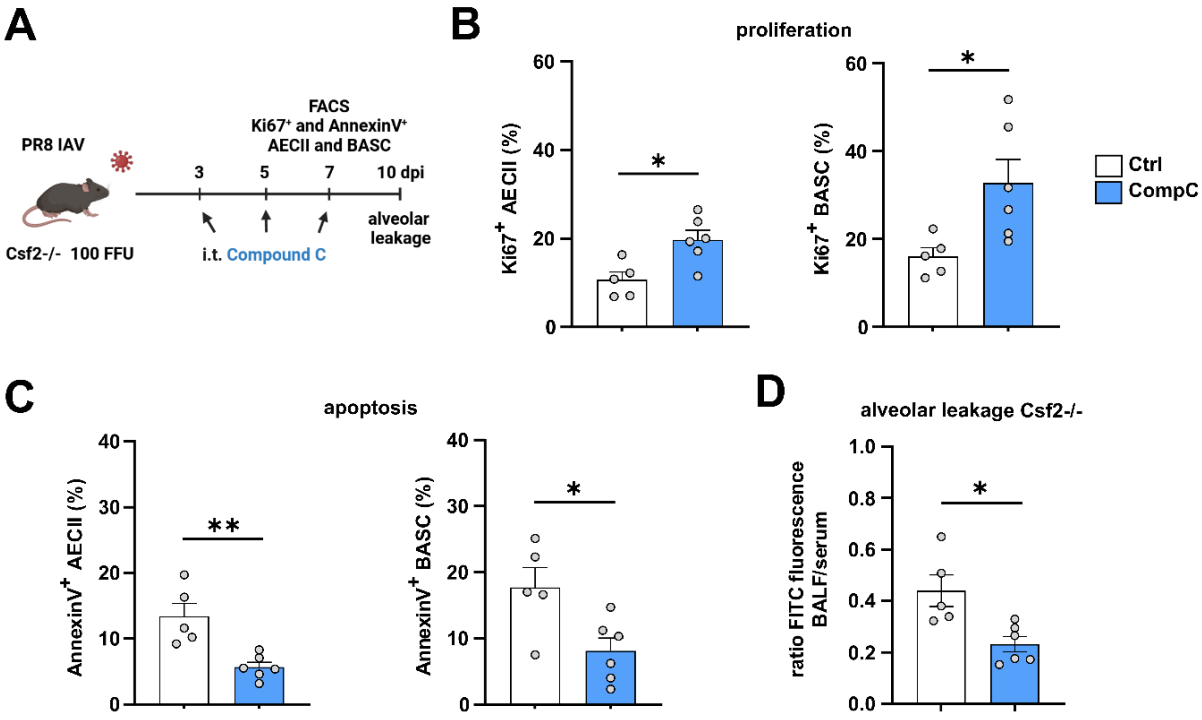

Figure 4.20: AMPK inhibitor treatment improves proliferation and reduces apoptosis in BASCs and AECIIs and rescues alveolar barrier repair after IAV infection in Csf2-/- mice. (A) Scheme of the experimental setup: Csf2-/- mice were infected with 100 FFU PR8 IAV. At 3 and 5 dpi, AMPK inhibitor Compound C or PBS control were i.t. applied. At 7 dpi, lungs were harvested to analyze the amount of Ki67$^+$ and AnnexinV$^+$ AECIIs and BASCs using FACS. At 10 dpi, the alveolar leakage was determined by FITC albumin application. **(B)** Amount of proliferating (Ki67$^+$) and **(C)** apoptotic (AnnexinV$^+$) AECIIs and BASCs in Csf2-/- mice treated with AMPK inhibitor (Compound C) or PBS control at 7 dpi. **(D)** Alveolar leakage (ratio FITC albumin in BALF / serum) in Csf2-/- mice treated with AMPK inhibitor (Compound C) or PBS control at 10 dpi. Probabilities were determined using t-test. Graphs show means ± SEM; *=p<0.05; **=p<0.005.

5 Discussion

In this study, it was identified that GM-CSF improves alveolar epithelial repair after IAV-induced injury by inhibiting AMPK and subsequently increasing downstream mTORC1 activity in AECIIs and BASCs, thereby promoting their proliferation. The treatment with inhaled GM-CSF (Sagramostim) has already been tested in ARDS patients.[149,269] The findings of this study deepen our understanding of the mechanisms behind the beneficial effects of GM-CSF, elucidate why GM-CSF is a promising treatment option, and inform further clinical trials regarding novel downstream targets for putative, and refined treatment strategies.

IAV-induced viral pneumonia can culminate in ARDS, characterized by hypoxia, pulmonary edema formation, and respiratory failure, caused by disruption of the alveolar epithelial barrier.[15] COVID-19 patients treated with inhaled GM-CSF experienced improved blood oxygenation compared to those in the standard of care group.[269] It is established that GM-CSF promotes alveolar epithelial regeneration, although the underlying molecular mechanisms remain to be elucidated.[270] Therefore, this study explored how GM-CSF enhances alveolar epithelial stem cell recovery after IAV infection and the signaling pathways involved. GM-CSF expressed by AECIIs and BASCs promotes their proliferation and reduces apoptosis, aiding alveolar barrier repair. Moreover, GM-CSF was found to be crucial for BALO formation. This study suggests GM-CSF suppresses AMPK activity, consequently licensing mTORC1 signaling to promote AECII and BASC proliferation. This was supported by *ex vivo* experiments utilizing murine and human primary AECs and lung organoid models as well as by *in vivo* experiments in mice.

GM-CSF gene expression was found to be upregulated in AECIIs at 4 and 7 days after IAV infection (Fig. 4.1, p. 56). These results corroborate the findings from Unkel et al. (2012), who demonstrated that AECIIs were the sole $CD45^-$ cell type exhibiting increased GM-CSF expression at 3 dpi.[216] Our data extend these observations, indicating that GM-CSF gene expression is not only upregulated in AECIIs but also in BASCs and persists beyond the early phase at 3 dpi, continuing until 7 dpi.

In the subsequent part of this study, the effects of GM-CSF on the proliferation and apoptosis of AECIIs and BASCs were investigated (Fig. 4.3, p. 62). The pro-proliferative role of GM-CSF in immune cells is well known.[270] Regarding AECII

apoptosis, Unkel *et al.* (2012) previously showed that GM-CSF expressed in the lung parenchyma reduces AEC apoptosis at 7 dpi, consistent with our results.[216] In the study by Unkel *et al.* (2012), infection doses were not adjusted, resulting in varying levels of lung injury across different mouse strains.[216] Consequently, the observed increase in AECII apoptosis in Csf2-/- mice was primarily attributed to a diminished adaptive immune response due to impaired DC function.[216] In contrast, our study observed significant differences in AECII and BASC proliferation and apoptosis among the various mouse strains, even though lower infection doses were administered to Csf2-/- mice and higher doses to SPC-GM mice compared to WT to normalize lung injury at 7 dpi. This finding highlights that GM-CSF is essential not only for proper immune function but also directly influences AECII and BASC apoptosis, independent of the cytopathic effects of IAV itself. Furthermore, our study is the first to demonstrate that GM-CSF influences not only AECII but also BASC proliferation and apoptosis, underscoring the critical role of GM-CSF also in bronchiolar epithelial repair.

At 10 dpi, differences in alveolar leakage between WT, Csf2-/-, and SPC-GM mice were observed (Fig. 4.4, p.64). This finding suggests that GM-CSF directly promotes alveolar epithelial repair by acting on AECIIs and BASCs, resulting in fewer damage-associated molecular patterns (DAMPs) being detected by innate immune cells, which in turn reduces the inflammatory response and lung injury.[271] However, previous research has shown that increased GM-CSF release following IAV infection enhances the innate immune functions of myeloid cells, leading to improved viral clearance and subsequent protection of AECs.[201,270] Therefore, the observed differences in lung repair among WT, Csf2-/-, and SPC-GM mice can be attributed to both enhanced immune functions and the autocrine effects of GM-CSF on AECIIs and BASCs.

In the next experiments, the effect of GM-CSF on distal epithelial stem cells was studied within the BALO model (Fig. 4.5, p. 66 and Fig. 4.6, p. 69). It was demonstrated that the growth of BALOs relies on the release of GM-CSF into the SN and GM-CSF/GM-CSFRβ signaling (Fig. 4.5). In WT BALOs, the GM-CSF concentration peaks at day 6 of culture and subsequently declines (Figure 4.5 C). Conversely, in Csf2rb-/- BALOs, the GM-CSF concentration increases with a delay and remains elevated thereafter. For BALO generation, BASCs are co-cultured with

PDGFRα⁺ rMCs, which are essential for organoid growth, cell differentiation, and branching morphogenesis. PDGFRα⁺ rMCs comprise a heterogeneous population consisting of myofibroblasts and lipofibroblasts.[184] El Agha *et al.* (2017) demonstrated that lipofibroblasts reside in close proximity to AECIIs *in vivo*, promoting AECII differentiation and epithelial growth.[272] Moreover, it is known that in alveolospheres, the self-renewal of AECIIs, as well as their differentiation into AECIs and formation of alveolar-like structures depends on lipofibroblasts.[8] It can be assumed that in BALO cultures, GM-CSF released from BASCs promotes BASC proliferation and differentiation through autocrine and paracrine mechanisms. It is presumed that binding of GM-CSF to its receptor on mesenchymal cells induces the release of growth factors such as transforming growth factor β (TGF-β) and platelet-derived growth factor (PDGF).[273] In a positive feedback loop, these growth factors enhance BASC and AECII proliferation and differentiation, resulting in improved organoid development. In Csf2rb-/- BALO cultures, the release of growth factors from rMCs is impaired due to the lacking GM-CSF/GM-CSFRβ signaling. Therefore, BASCs continue to release GM-CSF, which explains the increased GM-CSF concentrations in the SN of Csf2rb-/- BALOs until day 21 of culture (Fig. 4.5 C). Additionally, this study demonstrated that treatment with GM-CSF enhances the expression of *Ccnd1* in distal epithelial stem cells (Figure 4.6 D), indicating that GM-CSF directly stimulates proliferation in these cells, thereby supporting BALO development. It can be assumed that both the crosstalk between rMCs and BASCs, as well as the autocrine effect of GM-CSF on BASCs, contribute to the increase in Csf2-/-BALO size following GM-CSF treatment (Figure 4.6 A-C).

Moreover, it was found that the phenotype of Csf2rb-/- BALOs differs from that of WT BALOs (Fig. 4.5 A). Csf2rb-/- BALOs exhibit an increased alveolar lumen and, consequently, reduced alveolar complexity (Fig. 4.5 A and B). This can be attributed to the diminished proliferative capacity of BASCs in the absence of autocrine GM-CSF signaling. Additionally, it can be assumed that rMC functions are impaired due to the missing GM-CSF/GM-CSFRβ signaling. It is known that myofibroblasts in the neonatal lung deposit extracellular matrix (ECM), which serves as a scaffold for alveolarization.[274] In line with this, PDGFRα^{high} myofibroblasts are centrally located within BALOs and accumulate at branching sites.[184] The data from our study suggests that alveolarization in Csf2rb-/- BALOs is not only reduced due to decreased BASC

proliferation but also due to the impaired ability of rMCs to provide the necessary scaffolding for alveolarization.

In the next step of this study, the signaling pathway underlying the GM-CSF-mediated increase in proliferation was investigated. In *ex vivo* infected and recombinant GM-CSF-treated murine and human AECs as well as in AECIIs isolated from *in vivo* infected mice, it was confirmed that GM-CSF enhances anabolic processes by regulating the AMPK-mTORC1 signaling pathway (chapter 4.4). To confirm increased mTORC1 activity in distal epithelial stem cells, expression of the cell cycle related gene *cMyc* was examined. In AECIIs and BASCs isolated from IAV-infected WT and Csf2-/- mice, *cMyc* expression was only increased in the presence of GM-CSF (Fig. 4.8 G and H, p. 75). Moreover, GM-CSF treatment increased the expression of *Ccnd1* in *ex vivo* cultured primary murine AECIIs (Fig. 4.6 D, p. 69). A previous study from our group by Cakarova *et al.* (2009) highlighted that GM-CSF induces *Ccnd1* gene expression via downstream phosphorylation of STAT5 in AECIIs.[190] STAT5 forms dimers that bind to the DNA as transcription factors to regulate the expression of genes involved in cell growth, differentiation, and apoptosis.[275] Not only the AMPK-mTORC1 signaling pathway, but also activation of the JAK2-STAT5 pathway, could potentially be involved in the observed GM-CSF-mediated increase in *Ccnd1* gene expression in AECIIs (Fig. 4.6 D).

It is known that GM-CSF activates the PI3K/Akt pathway residing upstream of AMPK and mTORC1, capable of both inhibiting AMPK and activating mTORC1 through direct or indirect mechanisms.[212] Therefore, the PI3K/Akt pathway may serve as the link between the binding of GM-CSF to its receptor and the AMPK-mTORC1 signaling-dependent effects observed in this study. The GM-CSF-mediated modulation of the PI3K/Akt pathway could offer another explanation for the reduction in apoptotic AECIIs and BASCs following IAV infection (Fig. 4.3 D, p. 62). Activation of the GM-CSF-mediated PI3K/Akt pathway induces the gene expression of *Mcl-1,* which in turn protects AECs from apoptosis during oxidative stress.[276] However, the antiapoptotic protein Mcl-1 is short-lived. In the absence of GM-CSF, mTORC1 is downregulated, leading to inhibited protein translation and reduced levels of Mcl-1.[277] Conversely, this suggests that the activation of mTORC1 is essential for the translation and preservation of the antiapoptotic protein Mcl-1. This provides further support for the argument that GM-CSF-mediated inhibition of AMPK, and

consequently, activation of mTORC1 in AECIIs and BASCs, is indispensable for their protection from apoptosis.

The GM-CSF-mediated AMPK inhibition and regulation of metabolic pathways has not only been observed in our study. Wessendarp *et al.* (2022) found that in AMs proliferation is impaired in the absence of GM-CSF signaling.[278] Metabolomics analysis revealed an elevated AMP/ADP:ATP ratio in AMs from Csf2rb-/- compared to WT mice.[278] This finding suggests that the lack of GM-CSF signaling leads to AMPK activation, as AMPK is typically triggered by heightened ratios of adenosine nucleoside phosphates.[278] The modulation of metabolic pathways via AMPK appears to be significant in AMs, similar to its role in distal alveolar epithelial stem cells shown in our study.

The next experiments were focused on how GM-CSF affects the development of BALOs and alveolospheres by regulating the AMPK-mTORC1 signaling pathway (chapter 4.5). The treatment with AMPK inhibitor or mTORC1 activator replicated the effects of GM-CSF, enhancing the capacity of BASCs and AECIIs for organoid formation. Conversely, AMPK activator or mTORC1 inhibitor treatment had the opposite effect. Additionally, the amount of AECIIs in BALOs decreased following AMPK activator treatment. However, treatment with AMPK inhibitor mimicked the effect of GM-CSF and augmented the amount of AECIIs, suggesting increased AECII proliferation. Nevertheless, alterations in OFE and amount of AECIIs after AMPK and mTORC1 modulator treatments cannot solely be attributed to the regulation of the AMPK-mTORC1 signaling pathway within the epithelial compartment of BALOs. The effects of AMPK and mTORC1 modulator treatments could also impact rMCs and alter the release of growth factors, thereby influencing the pro-proliferative and organoid-forming capabilities of BASCs and AECIIs.[8,184,272,273] Moreover, differences in the alveolarization of BALOs subjected to AMPK activator or inhibitor treatment were assessed (Figure 4.12 F-H, p. 84). Treatment with AMPK activator AICAR led to an enlargement of the alveolar lumen displaying reduced complexity. Conversely, treatment with the AMPK inhibitor Compound C resulted in a more intricate alveolarization pattern marked by smaller alveolar lumen. These observations can be elucidated by both the direct impact of AMPK modulator treatments on AECIIs and BASCs, influencing their ability to proliferate, as well as by alterations in growth factor release from the mesenchymal compartment influenced by the AMPK modulator

treatments. Additionally, the ability of rMCs to provide the essential scaffold for alveolar structure formation may be altered by AMPK modulator treatments.[184,274] To overcome the problem that the AMPK and mTORC1 modulator treatments do not only affect the (bronchio)alveolar epithelial stem cells in BALO and alveolosphere cultures, but also the mesenchymal compartment, it would be an option to treat AECs or BASCs with AMPK or mTORC1 modulators prior to co-culture with untreated rMCs.

In the *in vivo* experiments performed in this study, WT and Csf2-/- mice were infected with IAV and treated with AMPK activator and inhibitor (chapter 4.6). Enhanced proliferation and reduced apoptosis of AECIIs and BASCs was observed in IAV-infected Csf2-/- mice following treatment with AMPK inhibitor Compound C (Fig. 4.20, p. 100). These findings indicate that the absence of GM-CSF can be compensated by an AMPK inhibitor, which replicates the effect of GM-CSF on distal epithelial stem cells. However, it is important to consider that treatment with an AMPK inhibitor may also exert a protective effect on AECIIs and BASCs by enhancing innate and adaptive immune functions.[149,216] Our previous research has demonstrated that GM-CSF released by AECs activates $CD103^+$ DCs, which in turn initiate adaptive immune mechanisms mediated by antigen-specific $CD4^+$ and $CD8^+$ T-cells, further improving viral clearance.[216] In a subsequent experiment, the numbers of infiltrated and activated immune cells in the lungs of infected mice after the treatment with AMPK activator or inhibitor could be analyzed.

Another relevant aspect is that GM-CSF-mediated AMPK inhibition may have a beneficial effect by improving edema fluid clearance after IAV infection. In a previous study, it was demonstrated that TRAIL released from AMs after IAV infection activates AMPK in AECs. Activated AMPK then initiates the degradation of Na,K-ATPase, reducing its abundance in the cell membrane. This process diminishes edema fluid clearance, leading to impaired blood oxygenation.[63] In a further experiment, it could be analyzed whether treatment of IAV-infected mice with GM-CSF or AMPK inhibitor increases the abundance of Na,K-ATPase in the AEC membrane, resulting in enhanced alveolar fluid clearance and improved blood oxygenation.

The effect of AMPK activator treatment on ALI has already been investigated in previous studies, but with a focus on neutrophil infiltration and activation. Neutrophils are crucial in innate immune responses.[279] While their activity is essential for eliminating microbial infections, excessive neutrophil activation, accompanied by the

enhanced release of proinflammatory cytokines, causes tissue damage and contributes to conditions such as acute lung injury.[279] Rameshrad *et al.* (2015) reported an anti-inflammatory effect of the AMPK activator A-769662 on lung tissue following LPS treatment.[280] According to their findings, the treatment with AMPK activator reduces the accumulation of neutrophils in lung tissue after LPS-challenge.[280] Additionally, in a study by Zhao *et al.* (2008), it was reported that treatment with AMPK activator AICAR mitigates the neutrophil-driven inflammatory response and reduces LPS-induced ALI.[279] These results contrast with those obtained in our study. The comparison of lung histological sections from IAV-infected WT and Csf2-/- mice suggests that in the absence of GM-CSF, which corresponds to increased AMPK activation, results in elevated leukocytic infiltrates (Figure 4.4, p. 64). Future experiments should analyze lung histological sections from IAV-infected WT and Csf2-/- mice for neutrophil infiltration following treatment with AICAR and Compound C.

In a prior investigation, it was elucidated that AECIIs are the primary source for GM-CSF in the distal lung at baseline level, with heightened production observed during IAV infection.[216] Additionally, it was demonstrated that GM-CSF derived from AECIIs, as opposed to myeloid cells, confers protection against IAV-induced lung injury.[216] Our study was specifically focused on GM-CSF secretion from the (bronchio)alveolar epithelial compartment following IAV infection. However, Csf2-/- mice lack global GM-CSF expression and exhibit comprised immune functions.[221] In a study conducted by Gschwend *et al.* (2021), $Sftpc^{Cre}$;$csf2^{fl}$ mice were utilized.[281] In these transgenic mice, a conditional GM-CSF knock-out can be induced in $Sftpc^{+}$ cells (AECIIs and BASCs) through tamoxifen application.[281] $Sftpc^{Cre}$;$csf2^{fl}$ mice exhibit a WT phenotype prior to the induction of GM-CSF knock-out, ensuring intact alveolar epithelial homeostasis and immune functions before the experiment.[281] This transgenic mouse model would allow to investigate the role of GM-CSF produced by $Sftpc^{+}$ AECIIs and BASCs on alveolar epithelial repair after IAV infection.

The results in this study indicate that the GM-CSF-mediated increase in AECII and BASC proliferation is vital for the restoration of the alveolar epithelial barrier after IAV infection. However, it is known that AECII proliferation and hyperplasia must be followed by differentiation into AECIs for barrier restoration.[282] The question remains whether AECII-to-AECI differentiation already occurs during the GM-CSF peak

between 4 and 7 dpi or if it is initiated subsequent to the decline in GM-CSF levels. In a study by Wang *et al.* (2023), it was demonstrated that AMPK activation is necessary for the differentiation of AECIIs into AECIs.[283] Specifically, they showed that the activation of AMPK-PFKFB2 signaling in AECIIs is crucial for substantial glycolytic ATP production, which supports the high energy demands required for AECII differentiation.[283] Moreover, they found that reduced AMPK-PFKFB2 signaling in AECIIs of aged lungs leads to decreased ATP production, resulting in impaired post-injury alveolar regeneration.[283] In our study, it was observed that AMPK inhibition, facilitated by GM-CSF, enhances the proliferation of AECIIs and BASCs. GM-CSF is released between 4 and 7 dpi, suggesting that AECII and BASC proliferation is particularly increased during this phase of IAV infection. Based on the findings of Wang *et al.*, we hypothesize that GM-CSF primarily drives proliferation rather than differentiation in distal epithelial stem cells. This suggests that after the GM-CSF peak declines and the AECII pool is expanded, AMPK activity increases to provide sufficient energy for the differentiation of AECIIs into AECIs and for proper alveolar repair. However, further experiments are required to validate this hypothesis.

This study specifically investigated the impact of GM-CSF on alveolar epithelial repair processes in ALI/ARDS induced by IAV infection. Given that GM-CSF enhances host defense and alveolar epithelial repair, its application is not solely restricted to IAV-induced lung injury but may also be effective against other respiratory viral infections through similar mechanisms.[201] However, ALI or ARDS can also result from non-infectious insults such as aspiration or trauma.[141] It is assumed that the beneficial effect of GM-CSF on distal lung epithelial stem cells that was investigated in this study remains applicable across diverse insults.

The main strategies to avoid or treat ARDS caused by IAV infections are vaccination and antiviral drugs.[201] However, due to the high genetic variability of IAV, continuous adjustment of the vaccine is required, and resistance to antiviral drugs can emerge (see chapter 1.2.2).[201] The administration of host-based, adjunctive therapies such as GM-CSF treatment represents a promising approach.[201]

Recombinant human GM-CSF (rhGM-CSF, Sagramostim, Leukine®), was initially approved to facilitate the recovery of bone marrow in various clinical contexts.[284] In cancer patients undergoing treatment with bone marrow-suppressive agents, rhGM-CSF enhances hematologic recovery, leading to a reduction in infection rates,

decreased therapy-related toxicity, and, in some cases, improved survival outcomes.[284] As an immune modulator, GM-CSF also augments anti-tumor responses in solid malignancies when used in combination with therapies such as checkpoint inhibitors and monoclonal antibodies.[284]

Inhaled GM-CSF could potentially reverse ARDS in patients.[149] Pulmonary GM-CSF not only provides protection against the virus itself by enhancing innate and adaptive immunity but also prevents major complications by directly promoting alveolar epithelial repair and inhibiting secondary bacterial infections.[201] Mice treated with inhaled GM-CSF during IAV infection showed a survival benefit upon secondary bacterial challenge with *S. pneumoniae*, attributed to a reduced incidence of bacteremia.[285]

In a phase II clinical trial involving patients with severe sepsis and respiratory dysfunction, low-dose intravenous recombinant human GM-CSF was administered.[286] Even though circulating neutrophils and pulmonary macrophages were activated, no significant increase in neutrophil infiltration into the lung was observed and gas exchange was improved.[286] Therefore, this study by Presneill *et al.* (2002) suggests that systemically applied low-dose GM-CSF has a homeostatic function in sepsis-related pulmonary dysfunction.[286] However, in another phase II clinical trial involving patients with ARDS, intravenous GM-CSF administration did not result in improved clinical outcomes.[287] Mouse studies indicate that high concentrations of GM-CSF in the alveolar lining fluid are more effective than systemic GM-CSF administration due to the prevention of systemic side effects.[201,288] Therefore, GM-CSF should preferably be applied via inhalation rather than systemic intravenous administration.[201] Further investigations should focus on how inhaled GM-CSF facilitates alveolar epithelial repair and which mechanisms are involved.

To investigate the potential benefits of inhaled GM-CSF on clinical outcomes in pneumonia-associated ARDS, a preliminary study on six patients was conducted. The off-label treatment with inhaled GM-CSF led to improvements in clinical parameters and enhanced host defense capacity of AMs, without observing increased alveolar neutrophil influx and organ toxicity.[149] As a result of these promising findings, the GI-HOPE study (ClinicalTrials.gov NCT02595060) was initiated. This study is a multicenter, double-blind, placebo-controlled, randomized

clinical trial designed to evaluate whether inhaled GM-CSF can enhance barrier repair and host defense mediated by AMs in ARDS patients.[289]

Since the beneficial effects of inhaled recombinant GM-CSF have been demonstrated in preclinical pneumonia studies,[233,237] investigations are underway to evaluate the treatment of COVID-19 patients with sargramostim in several clinical trials.[290,291,292,293,294,295] The phase two clinical trial GI-COVID (ClinicalTrials.gov NCT04569877) is still ongoing and investigates whether preemtive GM-CSF inhalation can prevent the progression to ARDS in patients with COVID-19 pneumonia.[294] In a study conducted by Bosteels *et al.* (2021), 81 non-ventilated COVID-19 patients with hypoxemic respiratory failure (PaO_2/FiO_2 ratio < 350mmHg) were treated with Sargramostim. On day 6, more patients from the treatment group displayed an increase in oxygenation of at least 25% compared to the standard-treated control group.[269] However, the treatment of COVID-19 patients with anti-GM-CSF or anti-GM-CSFRα antibody is also under investigation to assess whether inhibiting GM-CSF signaling prevents hyperinflammation induced by myeloid cells during the later stages of COVID-19 infection.[296,297,298,299]

Moreover, inhaled GM-CSF is being tested as a treatment for patients with respiratory virus-associated pneumonia, including but not limited to IAV and COVID-19.[300] Additionally, sagramostim treatment is evaluated in patients with severe sepsis to determine if GM-CSF can restore cellular immunity, provide protection against secondary bacterial infections, and enhance white blood cell function in individuals receiving intensive care.[301,302,303,304]

Overall, this study provides valuable insights into the diverse beneficial effects of GM-CSF, particularly on distal lung epithelial stem cells. These findings enhance our understanding of the mechanisms underlying the improved outcomes observed in ARDS patients[149] and facilitate the development of new strategies for future clinical research.

6 Summary

This study explored the beneficial effects of GM-CSF on distal alveolar epithelial stem cells after IAV infection and elucidated the molecular mechanisms involved. GM-CSF expression was upregulated in alveolar epithelial cells type II (AECII) and bronchioalveolar stem cells (BASC) at 4 and 7 dpi, boosting proliferation, reducing apoptosis, and improving alveolar epithelial barrier repair. GM-CSF was also essential for bronchioalveolar lung organoid (BALO) development.

Bulk RNA sequencing of BASCs from WT and Csf2-/- mice, both IAV-infected and mock-treated, led to the hypothesis that GM-CSF inhibits AMPK and activates mTORC1. This promotes AECII and BASC proliferation, crucial for alveolar repair post-IAV infection. To validate this hypothesis, primary murine and human AECs infected with PR8 IAV and treated with GM-CSF showed reduced AMPK and increased mTORC1 activity. In AECIIs isolated from infected mice, AMPK inhibition and mTORC1 activation also depended on GM-CSF/GM-CSFRβ signaling. Additionally, *cMyc* gene expression was upregulated in AECIIs and BASCs from IAV-infected WT, but not Csf2-/- mice. Treatment with the AMPK inhibitor (Compound C) increased organoid forming efficiency (OFE) in murine BALOs and alveolospheres, while the AMPK activator (AICAR) decreased it. The mTORC1 inhibitor (Rapamycin) reduced both OFE and size. Immunofluorescence stainings showed more AECIIs in BALOs treated with the AMPK inhibitor and fewer with the activator. IF stainings further confirmed that GM-CSF downregulates AMPK and boosts mTORC1 activity in AECIIs within BALOs. Finally, the hypothesis was tested *in vivo*. In IAV-infected WT and SPC-GM mice, intratracheal treatment with an AMPK activator reduced AECII and BASC proliferation and increased alveolar leakage. Conversely, treating IAV-infected Csf2-/- mice with an AMPK inhibitor compensated for the GM-CSF deficiency, enhancing proliferation, reducing apoptosis in AECIIs and BASCs, and decreasing alveolar leakage.

In summary, this work shows that the GM-CSF-mediated repair effects on the alveolar parenchyma after IAV-induced barrier damage are driven by inhibition of AMPK activation, licencing mTORC1 signaling and proliferation in alveolar epithelial stem cells, to achieve barrier repair (**Fig. 6**).

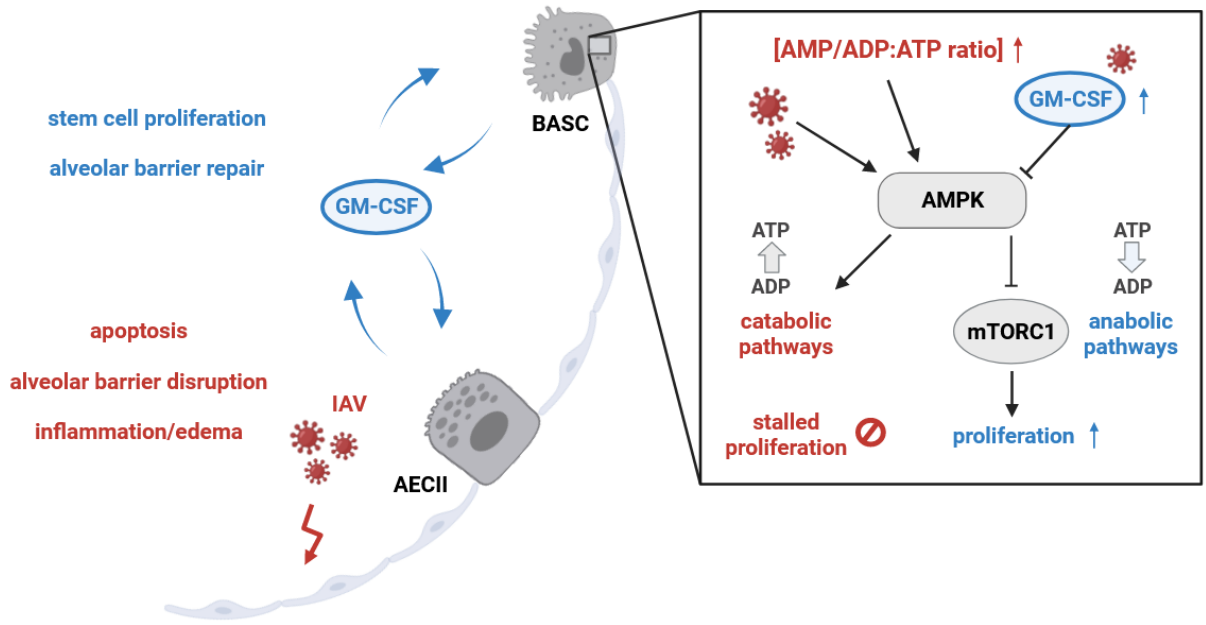

Figure 6: GM-CSF-mediated repair effects on the alveolar parenchyma after IAV-induced barrier damage are driven by inhibition of AMPK activation, licencing mTORC1 signaling and hence, proliferation in alveolar epithelial stem cells, to achieve barrier repair.

7 Zusammenfassung

Diese Arbeit untersucht, welchen positiven Einfluss GM-CSF auf distale epitheliale Stammzellen nach einer Influenza A Virus (IAV)-Infektion hat sowie die zugrunde liegenden molekularen Mechanismen. Es zeigte sich, dass die GM-CSF-Genexpression in alveolaren Epithelzellen Typ II (AECII) und bronchioalveolaren Stammzellen (BASC) an den Tagen 4 und 7 nach der IAV-Infektion erhöht war. Dies führte zu einer gesteigerten Proliferation und reduzierten Apoptose der AECII und BASC, wodurch die Reparatur des alveolaren Epithels unterstützt wurde. Zudem konnte gezeigt werden, dass die Entwicklung bronchioalveolarer Lungenorganoide (BALO) von GM-CSF abhängig ist.

Im weiteren Verlauf wurden die GM-CSF-vermittelten molekularen Mechanismen untersucht. Dazu wurde eine bulk-RNA-Sequenzierung der BASCs aus WT- und Csf2-/- Mäusen (sowohl IAV-infiziert als auch mock-behandelt) durchgeführt. Darauf basierend wurde die Hypothese entwickelt, dass GM-CSF AMPK hemmt und dadurch mTORC1 aktiviert wird. Dies steigert die Proliferation der AECII und BASC und trägt entscheidend zur Reparatur der alveolaren Barriere nach einer IAV-Infektion bei.

Zur Überprüfung dieser Hypothese wurden zunächst primäre murine und humane AECs mit PR8 IAV infiziert und mit GM-CSF behandelt. Diese Experimente zeigten eine verminderte AMPK- und eine erhöhte mTORC1-Aktivität in infizierten AECs nach GM-CSF Behandlung. Auch in AECII, die aus infizierten Mäusen isoliert wurden, war die AMPK Hemmung und mTORC1 Aktivierung nur in Anwesenheit von GM-CSF nachweisbar. Darüber hinaus war die Genexpression des Zellzyklusgens *cMyc* in AECII und BASC bei WT-Mäusen, nicht jedoch bei Csf2-/- Mäusen, erhöht. Die Behandlung mit dem AMPK-Inhibitor Compound C steigerte das Organoid-Bildungspotenzial der BASC und AECII, während der AMPK-Aktivator AICAR dieses Potenzial verringerte. Die Behandlung mit dem mTORC1-Inhibitor Rapamycin reduzierte sowohl die Organoidbildung als auch die Organoidgröße in murinen Alveolospheres. Immunfluoreszenz (IF) Färbungen zeigten eine Zunahme der AECII in BALO nach Behandlung mit dem AMPK-Inhibitor Compound C und eine Abnahme nach Behandlung mit dem AMPK-Aktivator AICAR. Zudem zeigten die IF Färbungen,

dass GM-CSF die AMPK-Aktivität in AECII in BALO herunterreguliert sowie die mTORC1-Aktivität steigert.

Schließlich wurde die Hypothese *in vivo* getestet. In IAV-infizierten WT- und SPC-GM-Mäusen (globales GM-CSF-Knock-out mit GM-CSF-Überexpression in AECII) verringerte die intratracheale Behandlung mit AMPK-Aktivator (AICAR) die Proliferation der AECII und BASC und erhöhte die Durchlässigkeit der alveolaren Barriere. Im Gegensatz dazu konnte der GM-CSF-Mangel in IAV-infizierten Csf2-/-Mäusen durch die intratracheale Behandlung mit AMPK-Inhibitor Compound C kompensiert werden. Die Compound C-Behandlung bewirkte eine gesteigerte Proliferation und reduzierte Apoptose der AECII und BASC, woraus eine geringere Durchlässigkeit der alveolaren Barriere resultierte.

Zusammengefasst konnte gezeigt werden, dass die positiven Effekte, die GM-CSF nach einer IAV-Infektion auf die Reparatur des alveolaren Epithels hat, durch AMPK Inhibierung und in Folge dessen mTORC1 Aktivierung in AECII und BASC vermittelt werden. Dies führt zu einer gesteigerten Proliferation der AECII und BASC, wodurch die Reparatur der alveolaren Barriere verbessert wird.

8 References

1. Griffiths, M. J. D., Bonnet, D. & Janes, S. M. Stem cells of the alveolar epithelium. *Lancet* **366**, 249–260 (2005).
2. Suarez, C. J., Dintzis, S. M. & Frevert, C. W. Respiratory. in *Comparative Anatomy and Histology* 121–134 (Elsevier, 2012). doi:10.1016/B978-0-12-381361-9.00009-3.
3. Mason, R. J. Biology of alveolar type II cells. *Respirology* **11**, (2006).
4. Johnson, M. D., Widdicombe, J. H., Allen, L., Barbry, P. & Dobbs, L. G. *Alveolar epithelial type I cells contain transport proteins and transport sodium, supporting an active role for type I cells in regulation of lung liquid homeostasis*. doi:10.1073/pnas.042689399.
5. Herzog, E. L., Brody, A. R., Colby, T. V., Mason, R. & Williams, M. C. Knowns and unknowns of the alveolus. *Proc. Am. Thorac. Soc.* **5**, 778–782 (2008).
6. Olajuyin, A. M., Zhang, X. & Ji, H.-L. Alveolar type 2 progenitor cells for lung injury repair. *Barlev Off. J. Cell Death Differ. Assoc.* **5**, (2019).
7. Hastings, R. H. Monitoring alveolar epithelial function in acute lung injury. *Journal of Clinical Monitoring and Computing* vol. 16 385–392 at https://doi.org/10.1023/A:1011407820548 (2000).
8. Barkauskas, C. E. *et al.* Type 2 alveolar cells are stem cells in adult lung. *J. Clin. Invest.* **123**, 3025–3036 (2013).
9. Salwig, I. *et al.* Bronchioalveolar stem cells are a main source for regeneration of distal lung epithelia in vivo. *EMBO J.* **38**, (2019).
10. Su, S., Fu, X., Li, G., Kerlin, F. & Veit, M. Novel Influenza D virus: Epidemiology, pathology, evolution and biological characteristics. (2017) doi:10.1080/21505594.2017.1365216.
11. Krammer, F. *et al.* Influenza. *Nat. Rev. Dis. Prim.* **4**, 1–21 (2018).
12. Killingley, B. & Nguyen-Van-Tam, J. Routes of influenza transmission. *Influenza and other Respiratory Viruses* vol. 7 42–51 at https://doi.org/10.1111/irv.12080 (2013).
13. Kalil, A. C. & Thomas, P. G. Influenza virus-related critical illness: Pathophysiology and epidemiology. *Critical Care* vol. 23 258 at https://doi.org/10.1186/s13054-019-2539-x (2019).
14. Tate, M. D. *et al.* Neutrophils Ameliorate Lung Injury and the Development of Severe Disease during Influenza Infection. *J. Immunol.* **183**, 7441–7450 (2009).
15. Short, K. R., Kroeze, E. J. B. V., Fouchier, R. A. M. & Kuiken, T. Pathogenesis of influenza-induced acute respiratory distress syndrome. *The Lancet Infectious Diseases* vol. 14 57–69 at https://doi.org/10.1016/S1473-3099(13)70286-X (2014).
16. Troeger, C. E. *et al.* Mortality, morbidity, and hospitalisations due to influenza lower respiratory tract infections, 2017: an analysis for the Global Burden of Disease Study 2017. (2019) doi:10.1016/S2213-2600(18)30496-X.
17. Plaza, P. I., Gamarra-Toledo, V., Rodríguez Euguí, J. & Lambertucci, S. A. Recent Changes in Patterns of Mammal Infection with Highly Pathogenic Avian Influenza A(H5N1) Virus Worldwide. *Emerg. Infect. Dis.* **30**, 444–452 (2024).
18. Pradyot Dash and Paul G. Thomas. Host Detection and the Stealthy Phenotype in Influenza Virus Infection. *Curr Top Microbiol Immunol.* **386**, (2014).
19. Benton, D. J., Wharton, S. A., Martin, S. R. & McCauley, J. W. Role of Neuraminidase in Influenza A(H7N9) Virus Receptor Binding. *J. Virol.* **91**, (2017).
20. Swayne, D. E. & Suarez, D. L. Highly pathogenic avian influenza. *OIE Rev. Sci. Tech.* **19**,

463–482 (2000).
21. Krammer, F. The human antibody response to influenza A virus infection and vaccination. *Nat. Rev. Immunol. 2019 196* **19**, 383–397 (2019).
22. Amonsin, A. *et al.* Genetic characterization of H5N1 influenza A viruses isolated from zoo tigers in Thailand. *Virology* **344**, 480–491 (2006).
23. Leguia, M. *et al.* Highly pathogenic avian influenza A (H5N1) in marine mammals and seabirds in Peru. *Nat. Commun. 2023 141* **14**, 1–11 (2023).
24. Tammiranta, N. *et al.* Highly pathogenic avian influenza A (H5N1) virus infections in wild carnivores connected to mass mortalities of pheasants in Finland. *Infect. Genet. Evol.* **111**, (2023).
25. Caserta, L. C. *et al.* Spillover of highly pathogenic avian influenza H5N1 virus to dairy cattle. *Nat. 2024* 1–3 (2024) doi:10.1038/s41586-024-07849-4.
26. Erster kanadischer Vogelgrippepatient schwer erkrankt. https://www.aerzteblatt.de/nachrichten/155704.
27. Ryu, S. & Cowling, B. J. Human Influenza Epidemiology. *Cold Spring Harb. Perspect. Med.* (2020) doi:10.1101/cshperspect.a038356.
28. Sautto, G. A., Kirchenbaum, G. A. & Ross, T. M. Towards a universal influenza vaccine: Different approaches for one goal. *Virol. J.* **15**, (2018).
29. Chambers, B. S., Parkhouse, K., Ross, T. M., Alby, K. & Hensley, S. E. Identification of hemagglutinin residues responsible for H3N2 antigenic drift during the 2014–2015 influenza season. *Cell Rep.* **12**, 1 (2015).
30. Wei, C.-J. *et al.* Next-generation influenza vaccines: opportunities and challenges. *Nat. Rev. Drug Discov.* doi:10.1038/s41573-019-0056-x.
31. World Health Organization. Background Paper on Influenza Vaccines and Immunization. 1–48 (2013).
32. Chen, C. *et al.* Global influenza vaccination rates and factors associated with influenza vaccination. *Int. J. Infect. Dis.* **125**, 153–163 (2022).
33. Hughes, K. *et al.* Effectiveness of Influenza Vaccine for Preventing Laboratory-Confirmed Influenza Hospitalizations in Immunocompromised Adults. *Clin. Infect. Dis.* **73**, e4353–e4360 (2021).
34. Tanner, A. R., Dorey, R. B., Brendish, N. J. & Clark, T. W. Influenza vaccination: protecting the most vulnerable. doi:10.1183/16000617.0258-2020.
35. Goodwin, K., Viboud, C. & Simonsen, L. Antibody response to influenza vaccination in the elderly: a quantitative review. *Vaccine* **24**, 1159–1169 (2006).
36. WHO Guidelines for Pharmacological Management of Pandemic Influenza A(H1N1) 2009 and other Influenza Viruses. 1–32 (2010).
37. McKimm-Breschkin, J. L. Influenza neuraminidase inhibitors: Antiviral action and mechanisms of resistance. *Influenza Other Respi. Viruses* **7**, 25–36 (2013).
38. Yin, H. *et al.* Development and Effects of Influenza Antiviral Drugs. *Molecules* **26**, 810 (2021).
39. Meijer, A. *et al.* Oseltamivir-Resistant Influenza Virus A (H1N1), Europe, 2007–08 Season. *Emerg. Infect. Dis.* **15**, 552–560 (2009).
40. Eun A. Kim et al. Viral Pneumonias in Adults: Radiologic and Pathologic Findings. *RadioGraphics* 137–149 (2002).
41. Kuiken, T. & Taubenberger, J. Pathology of Human Influenza Revisited. (2008) doi:10.1016/j.vaccine.2008.07.025.
42. Quantius, J. *et al.* Influenza Virus Infects Epithelial Stem/Progenitor Cells of the Distal Lung: Impact on Fgfr2b-Driven Epithelial Repair. **12**, e1005544 (2016).

43. Weinheimer, V. K. *et al.* Influenza A viruses target type II pneumocytes in the human lung. *J. Infect. Dis.* **206**, 1685–1694 (2012).
44. Matrosovich, M. N., Matrosovich, T. Y., Gray, T., Roberts, N. A. & Klenk, H. D. Human and avian influenza viruses target different cell types in cultures of human airway epithelium. *Proc. Natl. Acad. Sci. U. S. A.* **101**, 4620–4624 (2004).
45. Heaton, N. S. *et al.* Long-term survival of influenza virus infected club cells drives immunopathology. *J. Exp. Med.* **211**, 1707–1714 (2014).
46. Bruder, D., Srikiatkhachorn, A. & Enelow, R. I. Review Cellular Immunity and Lung Injury in Respiratory Virus Infection. *Viral Immunol.* **19**, (2006).
47. Högner, K. *et al.* Macrophage-expressed IFN-β Contributes to Apoptotic Alveolar Epithelial Cell Injury in Severe Influenza Virus Pneumonia. *PLoS Pathog.* **9**, (2013).
48. Hillaire, M. L. B., Rimmelzwaan, G. F. & Kreijtz, J. H. C. M. Clearance of influenza virus infections by T cells: Risk of collateral damage? *Curr. Opin. Virol.* **3**, 430–437 (2013).
49. Herold, S., Ludwig, S., Pleschka, S. & Wolff, T. Apoptosis signaling in influenza virus propagation, innate host defense, and lung injury. *J. Leukoc. Biol.* **92**, 75–82 (2012).
50. Brandes, M., Klauschen, F., Kuchen, S. & Germain, R. N. A systems analysis identifies a feedforward inflammatory circuit leading to lethal influenza infection. *Cell* **154**, 197 (2013).
51. Jain, S. *et al.* Hospitalized Patients with 2009 H1N1 Influenza in the United States, April–June 2009. *N. Engl. J. Med.* **361**, 1935–1944 (2009).
52. Mauad, T. *et al.* Lung Pathology in Fatal Novel Human Influenza A (H1N1) Infection. *Am. J. Respir. Crit. Care Med.* **181**, 72–79 (2010).
53. Vinay Kumar, Abul K. Abbas, Nelson Fausto & Jon C. Aster. *Robbins and Cotran Pathologic Basis of Diseases, 8th Edition*. (Elsevier, 2010).
54. Piantadosi, C. A. & Schwartz, D. A. The acute respiratory distress syndrome. *Ann. Intern. Med.* **141**, 460–470 (2004).
55. Ware, L. & Matthay, M. The Acute Respiratory Distress Syndrome. *N. Engl. J. Med.* (2000).
56. Gorin, A. B. & Stewart, P. A. Differential permeability of endothelial and epithelial barriers to albumin flux. *J. Appl. Physiol. Respir. Environ. Exerc. Physiol.* **47**, 1315–1324 (1979).
57. Koval, M. Claudin heterogeneity and control of lung tight junctions. *Annu. Rev. Physiol.* **75**, 551–567 (2013).
58. Folkesson, H. C. & Matthay, M. A. Alveolar epithelial ion and fluid transport: Recent progress. *Am. J. Respir. Cell Mol. Biol.* **35**, 10–19 (2006).
59. Berthiaume, Y. & Matthay, M. A. Alveolar edema fluid clearance and acute lung injury. *Respir. Physiol. Neurobiol.* **159**, 350–359 (2007).
60. Kunzelmann, K. *et al.* Influenza virus inhibits amiloride-sensitive Na+ channels in respiratory epithelia. *Proc. Natl. Acad. Sci. U. S. A.* **97**, 10282–10287 (2000).
61. Chen, X. J. *et al.* Influenza virus inhibits ENaC and lung fluid clearance. *Am. J. Physiol. - Lung Cell. Mol. Physiol.* **287**, 366–373 (2004).
62. Lazrak, A. *et al.* Influenza virus M2 protein inhibits epithelial sodium channels by increasing reactive oxygen species. *FASEB J.* **23**, 3829–3842 (2009).
63. Peteranderl, C. *et al.* Macrophage-epithelial paracrine crosstalk inhibits lung edema clearance during influenza infection. *J. Clin. Invest.* **126**, 1566–1580 (2016).
64. Uiprasertkul, M. *et al.* Apoptosis and pathogenesis of avian influenza A (H5N1) virus in humans. *Emerg. Infect. Dis.* **13**, 708–712 (2007).
65. Brydon, E. W. A., Smith, H. & Sweet, C. Influenza A virus-induced apoptosis in

bronchiolar epithelial (NCl-H292) cells limits pro-inflammatory cytokine release. *J. Gen. Virol.* **84**, 2389–2400 (2003).
66. Lam, W. Y. *et al.* Avian Influenza Virus A/HK/483/97(H5N1) NS1 Protein Induces Apoptosis in Human Airway Epithelial Cells. *J. Virol.* **82**, 2741–2751 (2008).
67. Takizawa, T., Ohashi, K. & Nakanishi, Y. Possible involvement of double-stranded RNA-activated protein kinase in cell death by influenza virus infection. *J. Virol.* **70**, 8128–8132 (1996).
68. Schultz-Cherry, S. & Hinshaw, V. S. Influenza virus neuraminidase activates latent transforming growth factor beta. *J. Virol.* **70**, 8624–8629 (1996).
69. Arndt, U. *et al.* Release of Macrophage Migration Inhibitory Factor and CXCL8/Interleukin-8 from Lung Epithelial Cells Rendered Necrotic by Influenza A Virus Infection. *J. Virol.* **76**, 9298–9306 (2002).
70. Golebiewski, L., Liu, H., Javier, R. T. & Rice, A. P. The Avian Influenza Virus NS1 ESEV PDZ Binding Motif Associates with Dlg1 and Scribble To Disrupt Cellular Tight Junctions. *J. Virol.* **85**, 10639–10648 (2011).
71. Zeng, H. *et al.* Human Pulmonary Microvascular Endothelial Cells Support Productive Replication of Highly Pathogenic Avian Influenza Viruses: Possible Involvement in the Pathogenesis of Human H5N1 Virus Infection. *J. Virol.* **86**, 667–678 (2012).
72. Ocaña-Macchi, M. *et al.* Hemagglutinin-Dependent Tropism of H5N1 Avian Influenza Virus for Human Endothelial Cells. *J. Virol.* **83**, 12947–12955 (2009).
73. Pinkerton, K. E., Gehr, P., Castaneda, A. & Crapo, J. D. Architecture and Cellular Composition of the Air-Blood Tissue Barrier. in *Comparative Biology of the Normal Lung (Second Edition)* 105–117 (Elsevier, 2015). doi:10.1016/B978-0-12-404577-4.00009-6.
74. Perrone, L. A., Plowden, J. K., García-Sastre, A., Katz, J. M. & Tumpey, T. M. H5N1 and 1918 Pandemic Influenza Virus Infection Results in Early and Excessive Infiltration of Macrophages and Neutrophils in the Lungs of Mice. *PLOS Pathog.* **4**, (2008).
75. Huber, D., Balda, M. S. & Matter, K. Transepithelial migration of neutrophils. *Invasion and Metastasis* **18**, 70–80 (1999).
76. Yang, S. C., Tsai, Y. F., Pan, Y. L. & Hwang, T. L. Understanding the role of neutrophils in acute respiratory distress syndrome. *Biomed. J.* **44**, 439–446 (2021).
77. Lacy, P. Mechanisms of degranulation in neutrophils. *Allergy Asthma. Clin. Immunol.* **2**, (2006).
78. Moraes, T. J., Zurawska, J. H. & Downey, G. P. Neutrophil granule contents in the pathogenesis of lung injury. *Curr. Opin. Hematol.* **13**, 21–27 (2006).
79. Rebetz, J., Semple, J. W. & Kapur, R. The Pathogenic Involvement of Neutrophils in Acute Respiratory Distress Syndrome and Transfusion-Related Acute Lung Injury. *Transfus. Med. Hemotherapy* **45**, 290–298 (2018).
80. Long, M. E., Mallampalli, R. K. & Horowitz, J. C. Pathogenesis of pneumonia and acute lung injury. *Clin. Sci.* **136**, 747–769 (2022).
81. Nguyen, G. T., Green, E. R. & Mecsas, J. Neutrophils to the ROScue: Mechanisms of NADPH oxidase activation and bacterial resistance. *Front. Cell. Infect. Microbiol.* **7**, (2017).
82. Pak, O. *et al.* Lung Ischaemia–Reperfusion Injury: The Role of Reactive Oxygen Species. *Adv. Exp. Med. Biol.* **967**, 195–225 (2017).
83. Winterbourn, C. C., Kettle, A. J. & Hampton, M. B. Reactive Oxygen Species and Neutrophil Function. *Annu. Rev. Biochem.* **85**, 765–792 (2016).
84. Brinkmann, V. *et al.* Neutrophil extracellular traps kill bacteria. *Science* **303**, 1532–

1535 (2004).
85. Van Avondt, K. & Hartl, D. Mechanisms and disease relevance of neutrophil extracellular trap formation. *Eur. J. Clin. Invest.* **48**, (2018).
86. Ashar, H. K. *et al.* The Role of Extracellular Histones in Influenza Virus Pathogenesis. *Am. J. Pathol.* **188**, 135–148 (2018).
87. Juliana, A., Zonneveld, R., Plötz, F. B., van Meurs, M. & Wilschut, J. Neutrophil-endothelial interactions in respiratory syncytial virus bronchiolitis: An understudied aspect with a potential for prediction of severity of disease. *J. Clin. Virol.* **123**, (2020).
88. Cortjens, B. *et al.* Neutrophil extracellular traps cause airway obstruction during respiratory syncytial virus disease. *J. Pathol.* **238**, 401–411 (2016).
89. Kopf, M., Schneider, C. & Nobs, S. P. The development and function of lung-resident macrophages and dendritic cells. *Nat. Immunol.* **16**, 36–44 (2015).
90. Malainou, C., Abdin, S. M., Lachmann, N., Matt, U. & Herold, S. Alveolar macrophages in tissue homeostasis, inflammation, and infection: evolving concepts of therapeutic targeting. *J. Clin. Invest.* **133**, (2023).
91. Tavares, L. P. *et al.* CXCR1/2 antagonism is protective during influenza and post-influenza pneumococcal infection. *Front. Immunol.* **8**, (2017).
92. Meischel, T., Villalon-Letelier, F., Saunders, P. M., Reading, P. C. & Londrigan, S. L. Influenza A virus interactions with macrophages: Lessons from epithelial cells. *Cell. Microbiol.* **22**, (2020).
93. Tumpey, T. M. *et al.* Pathogenicity of Influenza Viruses with Genes from the 1918 Pandemic Virus: Functional Roles of Alveolar Macrophages and Neutrophils in Limiting Virus Replication and Mortality in Mice. *J. Virol.* **79**, (2005).
94. Kumagai, Y. *et al.* Alveolar Macrophages Are the Primary Interferon-α Producer in Pulmonary Infection with RNA Viruses. *Immunity* **27**, 240–252 (2007).
95. Yu, W. C. L. *et al.* Viral Replication and Innate Host Responses in Primary Human Alveolar Epithelial Cells and Alveolar Macrophages Infected with Influenza H5N1 and H1N1 Viruses. *J. Virol.* **85**, (2011).
96. Liao, M. *et al.* Single-cell landscape of bronchoalveolar immune cells in patients with COVID-19. *Nat. Med.* **26**, (2020).
97. Grant, R. A. *et al.* Circuits between infected macrophages and T cells in SARS-CoV-2 pneumonia. *Nature* **590**, (2021).
98. Ghoneim, H. E., Thomas, P. G. & McCullers, J. A. Depletion of Alveolar Macrophages during Influenza Infection Facilitates Bacterial Superinfections. *J. Immunol.* **191**, (2013).
99. Santos, L. D. *et al.* TNF-mediated alveolar macrophage necroptosis drives disease pathogenesis during respiratory syncytial virus infection. *Eur. Respir. J.* **57**, (2021).
100. Li, F. *et al.* Monocyte-derived alveolar macrophages autonomously determine severe outcome of respiratory viral infection. *Sci. Immunol.* **7**, (2022).
101. Purnama, C. *et al.* Transient ablation of alveolar macrophages leads to massive pathology of influenza infection without affecting cellular adaptive immunity. *Eur. J. Immunol.* **44**, 2003–2012 (2014).
102. Schneider, C. *et al.* Alveolar Macrophages Are Essential for Protection from Respiratory Failure and Associated Morbidity following Influenza Virus Infection. *PLOS Pathog.* **10**, (2014).
103. Tate, M. D., Pickett, D. L., van Rooijen, N., Brooks, A. G. & Reading, P. C. Critical Role of Airway Macrophages in Modulating Disease Severity during Influenza Virus Infection of Mice. *J. Virol.* **84**, (2010).

104. Cardani, A., Boulton, A., Kim, T. S. & Braciale, T. J. Alveolar Macrophages Prevent Lethal Influenza Pneumonia By Inhibiting Infection Of Type-1 Alveolar Epithelial Cells. *PLOS Pathog.* **13**, (2017).
105. Wong, C. K. *et al.* Aging Impairs Alveolar Macrophage Phagocytosis and Increases Influenza-Induced Mortality in Mice. *J. Immunol.* **199**, 1060–1068 (2017).
106. Maus, U. A. *et al.* Resident Alveolar Macrophages Are Replaced by Recruited Monocytes in Response to Endotoxin-Induced Lung Inflammation. *Am. J. Respir. Cell Mol. Biol.* **35**, (2006).
107. Schneider, J. L. *et al.* The aging lung: Physiology, disease, and immunity. *Cell* **184**, 1990–2019 (2021).
108. McQuattie-Pimentel, A. C. *et al.* The lung microenvironment shapes a dysfunctional response of alveolar macrophages in aging. *J. Clin. Invest.* **131**, (2021).
109. Mould, K. J. *et al.* Cell origin dictates programming of resident versus recruited macrophages during acute lung injury. *Am. J. Respir. Cell Mol. Biol.* **57**, 294–306 (2017).
110. Herold, S. *et al.* Lung epithelial apoptosis in influenza virus pneumonia: The role of macrophage-expressed TNF-related apoptosis-inducing ligand. *J. Exp. Med.* **205**, 3065–3077 (2008).
111. Woods, P. S. *et al.* Tissue-resident alveolar macrophages do not rely on glycolysis for LPS-induced inflammation. *Am. J. Respir. Cell Mol. Biol.* **62**, 243–255 (2020).
112. Fang, F. C. Antimicrobial reactive oxygen and nitrogen species: Concepts and controversies. *Nat. Rev. Microbiol.* **2**, 820–832 (2004).
113. Szabó, C. Multiple pathways of peroxynitrite cytotoxicity. *Toxicol. Lett.* (2003) doi:10.1016/S0378-4274(02)00507-6.
114. Peteranderl, C., Herold, S. & Schmoldt, C. Human Influenza Virus Infections. *Semin. Respir. Crit. Care Med.* **37**, 487–500 (2016).
115. Szabo, P. A. *et al.* Longitudinal profiling of respiratory and systemic immune responses reveals myeloid cell-driven lung inflammation in severe COVID-19. *Immunity* **54**, 797–814 (2021).
116. Schulte-Schrepping, J. *et al.* Severe COVID-19 Is Marked by a Dysregulated Myeloid Cell Compartment. *Cell* **182**, 1419–1440 (2020).
117. Talmi-Frank, D. *et al.* Extracellular Matrix Proteolysis by MT1-MMP Contributes to Influenza-Related Tissue Damage and Mortality. *Cell Host Microbe* **20**, 458–470 (2016).
118. Wong, J. J. M., Leong, J. Y., Lee, J. H., Albani, S. & Yeo, J. G. Insights into the immuno-pathogenesis of acute respiratory distress syndrome. *Ann. Transl. Med.* **7**, 504–504 (2019).
119. Crotty, S. Follicular helper CD4 T cells (TFH). *Annu. Rev. Immunol.* **29**, 621–663 (2011).
120. Zhu, J., Yamane, H. & Paul, W. E. Differentiation of effector CD4 T cell populations. *Annu. Rev. Immunol.* **28**, 445–489 (2010).
121. Lee, H. G., Cho, M. Z. & Choi, J. M. Bystander CD4+ T cells: crossroads between innate and adaptive immunity. *Exp. Mol. Med.* **52**, 1255–1263 (2020).
122. Yunis, J., Short, K. R. & Yu, D. Severe respiratory viral infections: T-cell functions diverging from immunity to inflammation. *Trends Microbiol.* **31**, 644–656 (2023).
123. Murphy, K. M. & Stockinger, B. Effector T cell plasticity: flexibility in the face of changing circumstances. *Nat. Immunol.* **11**, 674–680 (2010).
124. Kent, S. J. *et al.* Disentangling the relative importance of T cell responses in COVID-19: leading actors or supporting cast? *Nat. Rev. Immunol.* **22**, 387–397 (2022).

125. Wherry, E. J. & Barouch, D. H. T cell immunity to COVID-19 vaccines. *Science* **377**, 821–822 (2022).
126. Samji, T. & Khanna, K. M. Understanding memory CD8+T cells. *Immunol. Lett.* **185**, 32–39 (2017).
127. Jameson, S. C. & Masopust, D. Understanding Subset Diversity in T Cell Memory. *Immunity* **48**, 214–226 (2018).
128. Sakaguchi, R. *et al.* Innate-like function of memory Th17 cells for enhancing endotoxin-induced acute lung inflammation through IL-22. *Int. Immunol.* **28**, 233–243 (2016).
129. Li, J. T. *et al.* Unexpected Role for Adaptive αβTh17 Cells in Acute Respiratory Distress Syndrome. *J. Immunol.* **195**, 87–95 (2015).
130. Wang, L. *et al.* Recovery from acute lung injury can be regulated via modulation of regulatory T cells and Th17 cells. *Scand. J. Immunol.* **88**, (2018).
131. Yi, X., Jian, W., Di, W., Jun, Z. & Mei, Y. Prognostic values of Th17 cells level in bronchoalveolar lavage fluid in children of sepsis with acute lung injury. *Chinese J. Contemp. Pediatr.* **17**, 942–945 (2015).
132. Pociask, D. A. *et al.* IL-22 is essential for lung epithelial repair following influenza infection. *Am. J. Pathol.* **182**, 1286–1296 (2013).
133. Vijayakumar, B. *et al.* Immuno-proteomic profiling reveals aberrant immune cell regulation in the airways of individuals with ongoing post-COVID-19 respiratory disease. *Immunity* **55**, 542–556 (2022).
134. Mathew, D. *et al.* Deep immune profiling of COVID-19 patients reveals distinct immunotypes with therapeutic implications. *Science* **369**, (2020).
135. Kreutmair, S. *et al.* Distinct immunological signatures discriminate severe COVID-19 from non-SARS-CoV-2-driven critical pneumonia. *Immunity* **54**, 1578–1593 (2021).
136. Garcia, D. & Shaw, R. J. AMPK: Mechanisms of Cellular Energy Sensing and Restoration of Metabolic Balance. *Mol. Cell* **66**, 789–800 (2017).
137. Jeon, S. M. Regulation and function of AMPK in physiology and diseases. *Exp. Mol. Med.* **48**, (2016).
138. Laplante, M. & Sabatini, D. M. Regulation of mTORC1 and its impact on gene expression at a glance. *J. Cell Sci.* **126**, 1713–1719 (2013).
139. Ishii, N. *et al.* Activation of AMP-activated protein kinase suppresses oxidized low-density lipoprotein-induced macrophage proliferation. *J. Biol. Chem.* **284**, 34561–34569 (2009).
140. Faivre, S., Kroemer, G. & Raymond, E. Current development of mTOR inhibitors as anticancer agents. *Nat. Rev. Drug Discov.* **5**, 671–688 (2006).
141. Fan, E., Brodie, D. & Slutsky, A. S. Acute respiratory distress syndrome advances in diagnosis and treatment. *J. Am. Med. Assoc.* **319**, 698–710 (2018).
142. Redant, S. *et al.* Diagnosing acute respiratory distress syndrome with the Berlin definition: Which technical investigations should be the best to confirm it? *J. Transl. Intern. Med.* **7**, 1–2 (2019).
143. Smith, F. G. *et al.* Effect of intravenous β-2 agonist treatment on clinical outcomes in acute respiratory distress syndrome (BALTI-2): A multicentre, randomised controlled trial. *Lancet* **379**, 229–235 (2012).
144. Perkins, G. D. *et al.* The beta agonist lung injury trial prevention a randomized controlled trial. *Am. J. Respir. Crit. Care Med.* **189**, 674–683 (2014).
145. Matthay, M. A. *et al.* Randomized, placebo-controlled clinical trial of an aerosolized β2-agonist for treatment of acute lung injury. *Am. J. Respir. Crit. Care Med.* **184**, 561–568 (2011).

146. McAuley, D. F. *et al.* Simvastatin in the Acute Respiratory Distress Syndrome. *N. Engl. J. Med.* **371**, 1695–1703 (2014).
147. Rosuvastatin for Sepsis-Associated Acute Respiratory Distress Syndrome. *N. Engl. J. Med.* **370**, 2191–2200 (2014).
148. McAuley, D. F. *et al.* Keratinocyte growth factor for the treatment of the acute respiratory distress syndrome (KARE): a randomised, double-blind, placebo-controlled phase 2 trial. *Lancet Respir. Med.* **5**, 484–491 (2017).
149. Susanne Herold, M.D., Ph.D. Katrin Hoegner, Ph.D. Istvan Vadasz, M.D. Tobias Gessler, M.D., Ph.D. Jochen Wilhelm, P. D. *et al.* Inhaled Granulocyte/Macrophage Colony–Stimulating Factor as Treatment of Pneumonia-associated Acute Respiratory Distress Syndrome. *Am. J. Respir. Crit. Care Med.* **189**, 609–611 (2014).
150. Planer, J. D. & Morrisey, E. E. After the Storm: Regeneration, Repair, and Reestablishment of Homeostasis Between the Alveolar Epithelium and Innate Immune System Following Viral Lung Injury. *Annu. Rev. Pathol.* **18**, 337–359 (2023).
151. Barkauskas, C. E. *et al.* Lung organoids: current uses and future promise. (2017) doi:10.1242/dev.140103.
152. Peroni, D. G. & Boner, A. L. Atelectasis: mechanisms, diagnosis and management. *Paediatr. Respir. Rev.* **1**, 274–278 (2000).
153. Han, S. H. & Mallampalli, R. K. The Role of Surfactant in Lung Disease and Host Defense against Pulmonary Infections. *Ann. Am. Thorac. Soc.* **12**, 765–774 (2015).
154. Williams, M. C. Alveolar Type I Cells: Molecular Phenotype and Development. *Annu. Rev. Physiol.* **65**, 669–695 (2003).
155. Evans, M. J., Cabral, L. J., Stephens, R. J. & Freeman, G. Transformation of alveolar Type 2 cells to Type 1 cells following exposure to NO2. *Exp. Mol. Pathol.* **22**, 142–150 (1975).
156. Anderson, W. R. & Thielen, K. Correlative study of adult respiratory distress syndrome by light, scanning, and transmission electron microscopy. *Ultrastruct. Pathol.* **16**, 615–628 (1992).
157. Tomashefski, J. F. Pulmonary pathology of acute respiratory distress syndrome. *Clin. Chest Med.* **21**, 435–466 (2000).
158. Desai, T. J., Brownfield, D. G. & Krasnow, M. A. Alveolar progenitor and stem cells in lung development, renewal and cancer. *Nature* **507**, 190–194 (2014).
159. Abdelwahab, E. M. M. *et al.* Wnt signaling regulates trans-differentiation of stem cell like type 2 alveolar epithelial cells to type 1 epithelial cells. *Respir. Res.* **20**, 204 (2019).
160. Zacharias, W. J. *et al.* Regeneration of the lung alveolus by an evolutionarily conserved epithelial progenitor. *Nature* **555**, 251–255 (2018).
161. Meng, X., Cui, G. & Peng, G. Lung development and regeneration: newly defined cell types and progenitor status. *Cell Regen.* **12**, (2023).
162. Nabhan, A. N., Brownfield, D. G., Harbury, P. B., Krasnow, M. A. & Desai, T. J. Single-cell Wnt signaling niches maintain stemness of alveolar type 2 cells. *Science* **359**, 1118–1123 (2018).
163. Liberti, D. C. *et al.* Alveolar epithelial cell fate is maintained in a spatially restricted manner to promote lung regeneration after acute injury. *Cell Rep.* **35**, (2021).
164. Strunz, M. *et al.* Alveolar regeneration through a Krt8+ transitional stem cell state that persists in human lung fibrosis. *Nat. Commun.* **11**, (2020).
165. Choi, J. *et al.* Inflammatory Signals Induce AT2 Cell-Derived Damage-Associated Transient Progenitors that Mediate Alveolar Regeneration. *Cell Stem Cell* **27**, 366–382 (2020).

166. Kobayashi, Y. *et al.* Persistence of a regeneration-associated, transitional alveolar epithelial cell state in pulmonary fibrosis. *Nat. Cell Biol.* **22**, 934–946 (2020).
167. Dupont, S. *et al.* Role of YAP/TAZ in mechanotransduction. *Nature* **474**, 179–183 (2011).
168. Lange, A. W. *et al.* Hippo/Yap signaling controls epithelial progenitor cell proliferation and differentiation in the embryonic and adult lung. *J. Mol. Cell Biol.* **7**, 35–47 (2015).
169. Nantie, L. B. *et al.* Lats1/2 inactivation reveals hippo function in alveolar type i cell differentiation during lung transition to air breathing. *Development* **145**, (2018).
170. LaCanna, R. *et al.* Yap/Taz regulate alveolar regeneration and resolution of lung inflammation. *J. Clin. Invest.* **129**, 2107–2122 (2019).
171. Chung, M. I., Bujnis, M., Barkauskas, C. E., Kobayashi, Y. & Hogan, B. L. M. Niche-mediated BMP/SMAD signaling regulates lung alveolar stem cell proliferation and differentiation. *Dev.* **145**, (2018).
172. Miller, A. J. *et al.* Generation of lung organoids from human pluripotent stem cells in vitro. *Nat. Protoc.* **14**, 518–540 (2019).
173. Hers, J. F. P., Masurel, N. & Mulder, J. Bacteriology and Histopathology of the Respiratory Tract and Lungs in Fatal Asian Influenza. *Lancet* **272**, 1141–1143 (1958).
174. Kumar, P. A. *et al.* Distal airway stem cells yield alveoli in vitro and during lung regeneration following H1N1 influenza infection. *Cell* **147**, 525–538 (2011).
175. Kanegai, C. M. *et al.* Persistent pathology in influenza-infected mouse lungs. *Am. J. Respir. Cell Mol. Biol.* **55**, 613–615 (2016).
176. Taylor, M. S. *et al.* Delayed alveolar epithelialization: A distinct pathology in diffuse acute lung injury. *Am. J. Respir. Crit. Care Med.* **197**, 522–524 (2018).
177. Vaughan, A. E. *et al.* Lineage-negative progenitors mobilize to regenerate lung epithelium after major injury. *Nature* **517**, 621–625 (2014).
178. Xi, Y. *et al.* Local lung hypoxia determines epithelial fate decisions during alveolar regeneration. *Nat. Cell Biol.* **19**, 904–914 (2017).
179. Sontake, V. & Tata, P. R. BALO : a “mini lung” model to study cell–cell interactions. *EMBO J.* **39**, (2020).
180. Giangreco, A., Reynolds, S. D. & Stripp, B. R. Terminal bronchioles harbor a unique airway stem cell population that localizes to the bronchoalveolar duct junction. *Am. J. Pathol.* **161**, 173–182 (2002).
181. Bender Kim, C. F. *et al.* Identification of bronchioalveolar stem cells in normal lung and lung cancer. *Cell* **121**, 823–835 (2005).
182. Liu, Q. *et al.* Lung regeneration by multipotent stem cells residing at the bronchioalveolar-duct junction. *Nat. Genet.* **51**, 728–738 (2019).
183. Basil, M. C. *et al.* Human distal airways contain a multipotent secretory cell that can regenerate alveoli. *Nature* **604**, 120–126 (2022).
184. Vazquez-Armendariz, A. I. *et al.* Multilineage murine stem cells generate complex organoids to model distal lung development and disease. *EMBO J.* **39**, (2020).
185. Katsura, H., Kobayashi, Y., Tata, P. R. & Hogan, B. L. M. IL-1 and TNFα Contribute to the Inflammatory Niche to Enhance Alveolar Regeneration. *Stem cell reports* **12**, 657–666 (2019).
186. Murray, P. J. The primary mechanism of the IL-10-regulated antiinflammatory response is to selectively inhibit transcription. *Proc. Natl. Acad. Sci. U. S. A.* **102**, 8686–8691 (2005).
187. Sabatel, C. *et al.* Exposure to Bacterial CpG DNA Protects from Airway Allergic Inflammation by Expanding Regulatory Lung Interstitial Macrophages. *Immunity* **46**,

457–473 (2017).
188. Fernandez, S., Jose, P., Avdiushko, M. G., Kaplan, A. M. & Cohen, D. A. Inhibition of IL-10 receptor function in alveolar macrophages by Toll-like receptor agonists. *J. Immunol.* **172**, 2613–2620 (2004).
189. Yu, X. *et al.* The Cytokine TGF-β Promotes the Development and Homeostasis of Alveolar Macrophages. *Immunity* **47**, 903–912 (2017).
190. Cakarova, L. *et al.* Macrophage tumor necrosis factor-α induces epithelial expression of granulocyte-macrophage colony-stimulating factor: Impact on alveolar epithelial repair. *Am. J. Respir. Crit. Care Med.* **180**, 521–532 (2009).
191. Major, J. *et al.* Type I and III interferons disrupt lung epithelial repair during recovery from viral infection. *Science* **369**, 712–717 (2020).
192. Li, G. G., Cao, Y. H., Run, Y., Xu, R. X. & Zheng, Z. D. Inhibition of CD8+ T cells and elimination of myeloid cells by CD4+ Foxp3− T regulatory type 1 cells in acute respiratory distress syndrome. *Clin. Exp. Pharmacol. Physiol.* **43**, 1191–1198 (2016).
193. Pervizaj-Oruqaj, L. *et al.* Alveolar macrophage-expressed Plet1 is a driver of lung epithelial repair after viral pneumonia. *Nat. Commun.* **15**, (2024).
194. Meng, C. *et al.* Amphiregulin inhibits TNF-α-induced alveolar epithelial cell death through EGFR signaling pathway. *Biomed. Pharmacother.* **125**, (2020).
195. Lin, K. L., Suzuki, Y., Nakano, H., Ramsburg, E. & Gunn, M. D. CCR2+ Monocyte-Derived Dendritic Cells and Exudate Macrophages Produce Influenza-Induced Pulmonary Immune Pathology and Mortality. *J. Immunol.* **180**, 2562–2572 (2008).
196. Jiang-Shieh, Y. F. *et al.* Distribution and expression of CD200 in the rat respiratory system under normal and endotoxin-induced pathological conditions. *J. Anat.* **216**, 407–416 (2010).
197. Snelgrove, R. J. *et al.* A critical function for CD200 in lung immune homeostasis and the severity of influenza infection. *Nat. Immunol.* **9**, 1074–1083 (2008).
198. Huang, S. *et al.* PPAR-γ in Macrophages Limits Pulmonary Inflammation and Promotes Host Recovery following Respiratory Viral Infection. *J. Virol.* **93**, (2019).
199. Schneider, C. *et al.* Induction of the nuclear receptor PPAR-γ by the cytokine GM-CSF is critical for the differentiation of fetal monocytes into alveolar macrophages. *Nat. Immunol.* **15**, 1026–1037 (2014).
200. Baker, A. D. *et al.* Targeted PPARγ deficiency in alveolar macrophages disrupts surfactant catabolism. *J. Lipid Res.* **51**, 1325–1331 (2010).
201. Rösler, B. & Herold, S. Lung epithelial GM-CSF improves host defense function and epithelial repair in influenza virus pneumonia—a new therapeutic strategy? *Mol. Cell. Pediatr.* (2016) doi:10.1186/s40348-016-0055-5.
202. Hamilton, J. A. Colony-stimulating factors in inflammation and autoimmunity. *Nat. Rev. Immunol.* **8**, 533–544 (2008).
203. Whetton, A. D. & Dexter, T. M. Myeloid haemopoietic growth factors. *Biochim. Biophys. Acta* **989**, 111–132 (1989).
204. Hamilton, J. A., Stanley, E. R., Burgess, A. W. & Shadduck, R. K. Stimulation of macrophage plasminogen activator activity by colony-stimulating factors. *J. Cell. Physiol.* **103**, 435–445 (1980).
205. Handman, E. & Burgess, A. W. Stimulation by Granulocyte-Macrophage Colony-Stimulating Factor of Leishmania Tropica Killing by Macrophages. *J. Immunol.* **122**, (1979).
206. Burgess, A. W. & Metcalf, D. The Nature and Action of Granulocyte-Macrophage Colony Stimulating Factors. *Blood* **56**, (1980).

207. Donald Metcalf, N. N. *The Hemopoietic Colony-stimulating Factors: From Biology to Clinical Applications*. (Cambridge University Press, 1995).
208. Griffin, J. D. *et al.* The biology of GM-CSF: Regulation of production and interaction with its receptor. *Int. J. Cell Cloning* **8**, 35–45 (1990).
209. Metcalf, D. Hematopoietic regulators: redundancy or subtlety? *Blood* **82**, 3515–3523 (1993).
210. Dougan, M., Dranoff, G. & Dougan, S. K. GM-CSF, IL-3, and IL-5 Family of Cytokines: Regulators of Inflammation. *Immunity* **50**, 796–811 (2019).
211. Sebastián, C. *et al.* Deacetylase activity is required for STAT5-dependent GM-CSF functional activity in macrophages and differentiation to dendritic cells. *J. Immunol.* **180**, 5898–5906 (2008).
212. Xu, J., Ji, J. & Yan, X. H. Cross-Talk between AMPK and mTOR in Regulating Energy Balance. *Crit. Rev. Food Sci. Nutr.* **52**, 373–381 (2012).
213. Hamilton, J. A. & Achuthan, A. Colony stimulating factors and myeloid cell biology in health and disease. *Trends Immunol.* **34**, 81–89 (2013).
214. Greter, M. *et al.* GM-CSF Controls Nonlymphoid Tissue Dendritic Cell Homeostasis but Is Dispensable for the Differentiation of Inflammatory Dendritic Cells Melanie. *Immunity* **36**, 1031–1046 (2012).
215. Louis, C. *et al.* Specific Contributions of CSF-1 and GM-CSF to the Dynamics of the Mononuclear Phagocyte System. *J. Immunol.* **195**, 134–144 (2015).
216. Unkel, B. *et al.* Alveolar epithelial cells orchestrate DC function in murine viral pneumonia. *J. Clin. Invest.* **122**, (2012).
217. Cates, E. C. *et al.* Intranasal Exposure of Mice to House Dust Mite Elicits Allergic Airway Inflammation via a GM-CSF-Mediated Mechanism. *J. Immunol.* **173**, 6384–6392 (2004).
218. Willart, M. A. M. *et al.* Interleukin-1α controls allergic sensitization to inhaled house dust mite via the epithelial release of GM-CSF and IL-33. *J. Exp. Med.* **209**, 1505–1517 (2012).
219. Ballinger, M. N. *et al.* Role of granulocyte macrophage colony-stimulating factor during gram-negative lung infection with Pseudomonas aeruginosa. *Am. J. Respir. Cell Mol. Biol.* **34**, 766–774 (2006).
220. Chen, G.-H. *et al.* Local GM-CSF–Dependent Differentiation and Activation of Pulmonary Dendritic Cells and Macrophages Protect against Progressive Cryptococcal Lung Infection in Mice. *J. Immunol.* **196**, 1810–1821 (2016).
221. Trapnell, B. C. & Whitsett, J. A. GM-CSF regulates pulmonary surfactant homeostasis and alveolar macrophage-mediated innate host defense. *Annu. Rev. Physiol.* **64**, 775–802 (2002).
222. Trapnell, B. C., Carey, B. C., Uchida, K. & Suzuki, T. Pulmonary alveolar proteinosis, a primary immunodeficiency of impaired GM-CSF stimulation of macrophages. *Curr. Opin. Immunol.* **21**, 514–521 (2009).
223. Stanley, E. *et al.* Granulocyte/macrophage colony-stimulating factor-deficient mice show no major perturbation of hematopoiesis but develop a characteristic pulmonary pathology. *Proc. Natl. Acad. Sci. U. S. A.* **91**, 5592–5596 (1994).
224. Ito, Y. *et al.* Influenza induces IL-8 and GM-CSF secretion by human alveolar epithelial cells through HGF/c-Met and TGF-α/EGFR signaling. *Am. J. Physiol. Cell. Mol. Physiol.* **308**, 1178–1188 (2015).
225. Guilliams, M. *et al.* Alveolar macrophages develop from fetal monocytes that differentiate into long-lived cells in the first week of life via GM-CSF. *J. Exp. Med.* **210**,

1977–1992 (2013).
226. Ginhoux, F. Fate PPAR-titioning: PPAR-γ 'instructs' alveolar macrophage development. *Nat. Immunol. 2014 1511* **15**, 1005–1007 (2014).
227. Ginhoux, F. & Guilliams, M. Tissue-Resident Macrophage Ontogeny and Homeostasis. *Immunity* **44**, 439–449 (2016).
228. Epelman, S., Lavine, K. J. & Randolph, G. J. Origin and Functions of Tissue Macrophages. *Immunity* **41**, 21–35 (2014).
229. van de Laar, L. *et al.* Yolk Sac Macrophages, Fetal Liver, and Adult Monocytes Can Colonize an Empty Niche and Develop into Functional Tissue-Resident Macrophages. *Immunity* **44**, 755–768 (2016).
230. Hashimoto, D. *et al.* Tissue-resident macrophages self-maintain locally throughout adult life with minimal contribution from circulating monocytes. *Immunity* **38**, 792–804 (2013).
231. Sever-Chroneos, Z. *et al.* GM-CSF modulates pulmonary resistance to influenza A infection. (2016) doi:10.1016/j.antiviral.2011.08.022.
232. Berclaz, P.-Y., Shibata, Y., Whitsett, J. A. & Trapnell, B. C. GM-CSF, via PU.1, regulates alveolar macrophage FcR-mediated phagocytosis and the IL-18/IFN-mediated molecular connection between innate and adaptive immunity in the lung. (2002) doi:10.1182/blood-2002-04-1102.
233. Huang, F.-F. *et al.* GM-CSF in the Lung Protects against Lethal Influenza Infection. (2011) doi:10.1164/rccm.201012-2036OC.
234. Subramaniam, R. *et al.* Protecting against post-influenza bacterial pneumonia by increasing phagocyte recruitment and ROS production. *J. Infect. Dis.* **209**, 1827–1836 (2014).
235. Min, L. *et al.* Cutting Edge: Granulocyte-Macrophage Colony-Stimulating Factor Is the Major CD8 + T Cell-Derived Licensing Factor for Dendritic Cell Activation . *J. Immunol.* **184**, 4625–4629 (2010).
236. Chen, Q., He, F., Kwang, J., Chan, J. K. Y. & Chen, J. GM-CSF and IL-4 Stimulate Antibody Responses in Humanized Mice by Promoting T, B, and Dendritic Cell Maturation. *J. Immunol.* **189**, 5223–5229 (2012).
237. Huang, H., Li, H., Zhou, P. & Ju, D. Protective effects of recombinant human granulocyte macrophage colony stimulating factor on H1N1 influenza virus-induced pneumonia in mice. *Cytokine* **51**, 151–157 (2010).
238. Paine, R. *et al.* Transgenic Overexpression of Granulocyte Macrophage-Colony Stimulating Factor in the Lung Prevents Hyperoxic Lung Injury. *Am. J. Pathol.* **163**, 2397–2406 (2003).
239. Sturrock, A., Mir-Kasimov, M., Baker, J., Rowley, J. & Paine, R. Key role of MicroRNA in the regulation of granulocyte macrophage colony-stimulating factor expression in murine alveolar epithelial cells during oxidative stress. *J. Biol. Chem.* **289**, 4095–4105 (2014).
240. Chen, Y., Li, F., Hua, M., Liang, M. & Song, C. Role of GM-CSF in lung balance and disease. *Front. Immunol.* **14**, (2023).
241. Shiomi, A. & Usui, T. Pivotal roles of GM-CSF in autoimmunity and inflammation. *Mediators Inflamm.* **2015**, (2015).
242. Xing, Z. *et al.* Gene transfer for cytokine functional studies in the lung: the multifunctional role of GM-CSF in pulmonary inflammation. *J. Leukoc. Biol.* **59**, 481–488 (1996).
243. Matute-Bello, G. *et al.* Modulation of neutrophil apoptosis by granulocyte colony-

stimulating factor and granulocyte/macrophage colony-stimulating factor during the course of acute respiratory distress syndrome. *Crit. Care Med.* **28**, 1–7 (2000).
244. Overgaard, C. E. *et al.* The relative balance of GM-CSF and TGF-β1 regulates lung epithelial barrier function. *Am. J. Physiol. - Lung Cell. Mol. Physiol.* **308**, 1212–1223 (2015).
245. Tazi, A. *et al.* Evidence that granulocyte macrophage-colony-stimulating factor regulates the distribution and differentiated state of dendritic cells/Langerhans cells in human lung and lung cancers. *J. Clin. Invest.* **91**, 566–576 (1993).
246. Hall, M. W. *et al.* Innate immune function and mortality in critically III children with influenza: A multicenter study. *Crit. Care Med.* **41**, 224–236 (2013).
247. Dranoff, G. *et al.* Involvement of Granulocyte-Macrophage Colony-Stimulating Factor in Pulmonary Homeostasis. *Science* **264**, 713–716 (1994).
248. Paine, R. *et al.* Granulocyte-Macrophage Colony-Stimulating Factor in the Innate Immune Response to Pneumocystis carinii Pneumonia in Mice . *J. Immunol.* **164**, 2602–2609 (2000).
249. LeVine, A. M., Reed, J. A., Kurak, K. E., Cianciolo, E. & Whitsett, J. A. GM-CSF-deficient mice are susceptible to pulmonary group B streptococcal infection. *J. Clin. Invest.* **103**, 563–569 (1999).
250. Huffman, J. A., Hull, W. M., Dranoff, G., Mulligan, R. C. & Whitsett, J. A. Pulmonary epithelial cell expression of GM-CSF corrects the alveolar proteinosis in GM-CSF-deficient mice. *J. Clin. Invest.* **97**, 649–655 (1996).
251. Huffman Reed, J. A. *et al.* GM-CSF enhances lung growth and causes alveolar type II epithelial cell hyperplasia in transgenic mice. *Lung Cell. Mol. Physiol* **17**, 715–725 (1997).
252. Human Primary Alveolar Epithelial Cells. https://cellbiologics.com/index.php?route=product/product&product_id=2374.
253. Herold, S. *et al.* Alveolar Epithelial Cells Direct Monocyte Transepithelial Migration upon Influenza Virus Infection: Impact of Chemokines and Adhesion Molecules. *J. Immunol.* **177**, 1817–1824 (2006).
254. Kathiriya, J. J. *et al.* Human alveolar type 2 epithelium transdifferentiates into metaplastic KRT5+ basal cells. *Nat. Cell Biol.* **24**, 10–23 (2022).
255. Bao, Y., Gao, Y., Shi, Y. & Cui, X. Dynamic gene expression analysis in a H1N1 influenza virus mouse pneumonia model. *Virus Genes* **53**, 357–366 (2017).
256. Pleguezuelos-Manzano, C. *et al.* Establishment and Culture of Human Intestinal Organoids Derived from Adult Stem Cells. *Curr. Protoc. Immunol.* **130**, (2020).
257. Myers, M. A. *et al.* Dynamically linking influenza virus infection kinetics, lung injury, inflammation, and disease severity. *Elife* **10**, (2021).
258. Montalto, F. I. & De Amicis, F. Cyclin D1 in Cancer: A Molecular Connection for Cell Cycle Control, Adhesion and Invasion in Tumor and Stroma. doi:10.3390/cells9122648.
259. STEIN, S. C., WOODS, A., JONES, N. A., DAVISON, M. D. & CARLING, D. The regulation of AMP-activated protein kinase by phosphorylation. *Biochem. J.* **345**, 437–443 (2000).
260. Nacarelli, T., Azar, A. & Sell, C. Aberrant mTOR activation in senescence and aging: A mitochondrial stress response? *Exp. Gerontol.* **68**, 66–70 (2015).
261. Yang, W. R. *et al.* mTOR is involved in 17β-estradiol-induced, cultured immature boar Sertoli cell proliferation via regulating the expression of SKP2, CCND1, and CCNE1. *Mol. Reprod. Dev.* **82**, 305–314 (2015).
262. Liu, P. F. *et al.* ATG4B promotes colorectal cancer growth independent of autophagic

flux. *Autophagy* **10**, 1454–1465 (2014).
263. Liu, P. *et al.* A functional mammalian target of rapamycin complex 1 signaling is indispensable for c-Myc-driven hepatocarcinogenesis. *Hepatology* **66**, 167–181 (2017).
264. Csibi, A. *et al.* The mTORC1/S6K1 pathway regulates glutamine metabolism through the eif4b-dependent control of c-Myc translation. *Curr. Biol.* **24**, 2274–2280 (2014).
265. Pelengaris, S., Khan, M. & Evan, G. c-MYC: more than just a matter of life and death. *Nat. Rev. Cancer* **2**, 764–776 (2002).
266. Zordoky, B. N. M. *et al.* AMPK-dependent inhibitory phosphorylation of ACC is not essential for maintaining myocardial fatty acid oxidation. *Circ. Res.* **115**, 518–524 (2014).
267. Copp, J., Manning, G. & Hunter, T. TORC-Specific phosphorylation of mammalian target of rapamycin (mTOR): phospho-Ser 2481 is a marker for intact mTOR signaling complex 2. *Cancer Res.* **69**, 1821–1827 (2009).
268. Zabihi, M. *et al.* An Optimized Protocol for the Generation of Alveolospheres from Wild-Type Mice. *Cells* **13**, (2024).
269. Bosteels, C. *et al.* Early treatment with inhaled GM-CSF improves oxygenation and anti-viral immunity in COVID-19 induced lung injury-a randomized clinical trial. (2021) doi:10.21203/rs.3.rs-959220/v1.
270. McCormick, T. S., Hejal, R. B., Leal, L. O. & Ghannoum, M. A. GM-CSF: Orchestrating the Pulmonary Response to Infection. *Front. Pharmacol.* **12**, (2022).
271. Hsieh, P. C. *et al.* Deciphering the role of damage-associated molecular patterns and inflammatory responses in acute lung injury. *Life Sci.* **305**, (2022).
272. El Agha, E. *et al.* Two-Way Conversion between Lipogenic and Myogenic Fibroblastic Phenotypes Marks the Progression and Resolution of Lung Fibrosis. *Cell Stem Cell* **20**, 261–273 (2017).
273. Wohlfahrt, T. *et al.* PU.1 controls fibroblast polarization and tissue fibrosis. *Nature* **566**, 344–349 (2019).
274. El Agha, E. & Bellusci, S. Walking along the Fibroblast Growth Factor 10 Route: A Key Pathway to Understand the Control and Regulation of Epithelial and Mesenchymal Cell-Lineage Formation during Lung Development and Repair after Injury. *Scientifica (Cairo).* **2014**, 1–20 (2014).
275. Hu, X., Li, J., Fu, M., Zhao, X. & Wang, W. The JAK/STAT signaling pathway: from bench to clinic. doi:10.1038/s41392-021-00791-1.
276. Sturrock, A. *et al.* GM-CSF provides autocrine protection for murine alveolar epithelial cells from oxidant-induced mitochondrial injury. **302**, (2012).
277. Villanueva-Paz, M. *et al.* AMPK Regulation of Cell Growth, Apoptosis, Autophagy, and Bioenergetics. *EXS* **107**, 45–71 (2016).
278. Wessendarp, M. *et al.* Role of GM-CSF in regulating metabolism and mitochondrial functions critical to macrophage proliferation. doi:10.1016/j.mito.2021.10.009.
279. Zhao, X. *et al.* Activation of AMPK attenuates neutrophil proinflammatory activity and decreases the severity of acute lung injury. *Am. J. Physiol. - Lung Cell. Mol. Physiol.* **295**, 497–504 (2008).
280. Rameshrad, M., Soraya, H., Maleki-Dizaji, N., Vaez, H. & Garjani, A. A-769662, a direct AMPK activator, attenuates lipopolysaccharide-induced acute heart and lung inflammation in rats. *Mol. Med. Rep.* **13**, 2843–2849 (2016).
281. Gschwend, J. *et al.* Alveolar macrophages rely on GM-CSF from alveolar epithelial type 2 cells before and after birth. *J. Exp. Med.* **218**, (2021).

282. Sun, T. *et al.* TAZ is required for lung alveolar epithelial cell differentiation after injury. *JCI Insight* **4**, (2019).
283. Wang, Z. *et al.* Enhanced glycolysis-mediated energy production in alveolar stem cells is required for alveolar regeneration. *Cell Stem Cell* **30**, 1028–1042 (2023).
284. Lazarus, H. M., Ragsdale, C. E., Gale, R. P. & Lyman, G. H. Sargramostim (rhu GM-CSF) as Cancer Therapy (Systematic Review) and An Immunomodulator. A Drug Before Its Time? *Front. Immunol.* **12**, (2021).
285. Umstead, T. M. *et al.* Lower respiratory tract delivery, airway clearance, and preclinical efficacy of inhaled GM-CSF in a postinfluenza pneumococcal pneumonia model. *Am. J. Physiol. Cell. Mol. Physiol.* **318**, 571–579 (2020).
286. Presneill, J. J., Harris, T., Stewart, A. G., Cade, J. F. & Wilson, J. W. A randomized phase II trial of granulocyte-macrophage colony-stimulating factor therapy in severe sepsis with respiratory dysfunction. *Am. J. Respir. Crit. Care Med.* **166**, 138–143 (2002).
287. Paine, R. *et al.* A randomized Trial of recombinant human granulocyte-macrophage colony stimulating factor for Patients with acute lung injury. *Crit. Care Med.* **40**, 90–97 (2012).
288. Halstead, E. S. *et al.* GM-CSF overexpression after influenza a virus infection prevents mortality and moderates M1-like airway monocyte/macrophage polarization. *Respir. Res.* **19**, 3 (2018).
289. Granulocyte Macrophage-Colony Stimulating Factor (GM-CSF) Inhalation to Improve Host Defense and Pulmonary Barrier Restoration - ClinicalTrials.gov. https://clinicaltrials.gov/ct2/show/NCT02595060.
290. A Phase II/III Study of Sargramostim in Patients with Coronavirus Disease-2019 (COVID-19) - ClinicalTrials.gov. https://clinicaltrials.gov/ct2/show/NCT04642950.
291. Sargramostim in Patients With Acute Hypoxic Respiratory Failure Due to COVID-19 (SARPAC) - ClinicalTrials.gov. https://clinicaltrials.gov/ct2/show/NCT04326920.
292. Study of Sargramostim in Patients With COVID-19 - ClinicalTrials.gov. https://clinicaltrials.gov/ct2/show/NCT04411680.
293. Sargramostim Use in COVID-19 to Recover Patient Health - ClinicalTrials.gov. https://clinicaltrials.gov/ct2/show/NCT04707664.
294. GM-CSF Inhalation to Prevent ARDS in COVID-19 Pneumonia - ClinicalTrials.gov. https://clinicaltrials.gov/ct2/show/NCT04569877.
295. Using GM-CSF as a Host Directed Therapeutic Against COVID-19 | ClinicalTrials.gov. https://clinicaltrials.gov/study/NCT04400929?cond=covid-19&intr=Sagramostim&limit=50&rank=6.
296. Study of Mavrilimumab (KPL-301) in Participants Hospitalized With Severe Corona Virus Disease 2019 (COVID-19) Pneumonia and Hyper-inflammation | ClinicalTrials.gov. https://clinicaltrials.gov/study/NCT04447469?cond=covid-19&intr=Sagramostim&limit=50&rank=10.
297. Phase 3 Study to Evaluate Efficacy and Safety of Lenzilumab in Patients With COVID-19 | ClinicalTrials.gov. https://clinicaltrials.gov/study/NCT04351152?cond=covid-19&intr=Sagramostim&limit=50&rank=5.
298. A Study to Assess the Efficacy and Safety of Gimsilumab in Subjects With Lung Injury or Acute Respiratory Distress Syndrome Secondary to COVID-19 (BREATHE) | ClinicalTrials.gov. https://clinicaltrials.gov/study/NCT04351243?cond=covid-19&intr=Sagramostim&limit=50&rank=7.
299. Burmester, G. R. *et al.* Mavrilimumab, a Fully Human Granulocyte–Macrophage Colony-Stimulating Factor Receptor α Monoclonal Antibody: Long-Term Safety and

Efficacy in Patients With Rheumatoid Arthritis. *Arthritis Rheumatol.* **70**, 679–689 (2018).

300. Inhaled GM-CSF for Respiratory Virus-Associated Severe Pneumonia | ClinicalTrials.gov. https://clinicaltrials.gov/study/NCT02601365?cond=ARDS&intr=Sagramostim&limit=50&rank=4.
301. Does GM-CSF Restore Neutrophil Phagocytosis in Critical Illness? | ClinicalTrials.gov. https://clinicaltrials.gov/study/NCT01653665?cond=Sepsis&intr=Sagramostim&limit=50&page=1&rank=3.
302. GM-CSF for Reversal of immunoparalysis in pediatric sepsis-induced MODS Study | ClinicalTrials.gov. https://clinicaltrials.gov/study/NCT03769844?cond=Sepsis&intr=Sagramostim&limit=50&page=1&rank=4.
303. GM-CSF to Decrease ICU Acquired Infections | ClinicalTrials.gov. https://clinicaltrials.gov/study/NCT02361528?cond=Sepsis&intr=Sagramostim&limit=50&page=1&rank=2.
304. Reconstruction of Monocytic Immunocompetence by Granulocyte-macrophage-colony Stimulating Factor (GM-CSF) in Patients With Severe Sepsis and Septic Shock | ClinicalTrials.gov. https://clinicaltrials.gov/study/NCT00252915?cond=Sepsis&intr=Sagramostim&limit=50&page=1&rank=1.

9 Supplement

9.1 List of figures and tables

9.2 Materials

9.2.1 Machines and devices

Device	**Manufacturers´ designation**	**Company**
Anesthesia machine	MiniHub V2.1 gas anesthesia workstation for small animals	TemSega (France)
Benchtop centrifuge	Heraeus Fresco 21 Micro Centrifuge	Thermo Fisher (United States)
Cell Counter	NucleoCounter NC-250	ChemoMetec (Denmark)
Centrifuge	Heraeus Multifuge 3 S-R Refrigerated Centrifuge	Thermo Fisher (United States)
Electrophoresis Cell	Mini-PROTEAN Tetra Vertical	Bio Rad (United States)
Flow cytometer	BD Aria	Becton Dickinson (United States)
	BD LSRFortessa	
HandyStep 1	20M93477	Brandt
Imaging system	ChemiDoc XRS+	Bio Rad (United States)
Incubator	Heracell VIOS 160i CO2 incubator single chamber	Thermo Fisher (United States)
Magnetic Particle Concentrator	Dynal MPC™-6	
Microplate reader	Microplate reader iMark	Bio Rad (United States)
Microscopes	BX41 light microscope	Olympus (Germany)
	EVOS M700 and EVOS M7000	Thermo Fisher (United States)
	SP8 confocal microscope	Leica (Germany)
NanoDrop	NanoDrop One Microvolume UV-Vis Spectrophotometer with WiFi	Thermo Fisher (United States)
Nucleic acid extraction machine	QIAcube connect	Qiagen (Netherlands)

pH meter	FiveEasy Plus pH meter FP20-Std-Kit	Mettler Toledo (United States)
Pulse oximeter	PhysioSuite MouseSTAT System	Kent Scientific (United States)
Pipettes	Eppendorf Reference® 2, 0,5 – 10 µL pipette	Eppendorf (Germany)
	Eppendorf Reference® 2, 10 – 100 µL pipette	
	Eppendorf Reference® 2, 100 – 1,000 µL pipette	
	Eppendorf Reference® 2, 2 – 20 µL pipette	
	Eppendorf Reference® 2, 20 – 200 µL pipette	
Platform shaker	Heidolph Polymax 1040	Heidolph (Germany)
Power supply	PowerPac™ Basic	Bio Rad (United States)
qPCR machines	QuantStudio™ 3 Real-Time PCR System, 96-well, 0.1 mL	Thermo Fisher (United States)
	StepOne™ Real-Time PCR System, laptop	
Serological pipet	Pipetboy	Integra (Germany)
Sterile workbench	Heraeus MSC-Advantage Class II Biological Safety Cabinets	Thermo Fisher (United States)
Thermocycler	Veriti Thermal Cycler	
Tissue dissociator	gentleMACS Dissociator	Miltenyi Biotech (Germany)
Transfer system Western Blot	Trans-Blot Turbo	Bio Rad (United States)
Vortex	Vortex-Genie 2	Thermo Fisher (United States)

9.2.2 Consumables and chemicals

Designation	Catalog number	Company
Agarose, low gelling temperature (CAS-No: 39346-81-1)	A9414	Merck (Germany)
Albumin-Fluoresceinisothiocyanat-Konjugat	A9771	
Amphotericin B solution (250 µg/ml)	A2942	
Annexin V, Pacific Blue™ conjugate, for flow cytometry	A35122	ThermoFisher (United States)
Annexin Binding Buffer (5X), for flow cytometry	V13246	
Aqua	0082479E	B.Braun (Germany)
Avicell		FMC BioPolymer
BD Eclipse Needle 23G	305892	Becton Dickinson (United States)
Bovine Serum Albumin	A7030-50G	Sigma Aldrich (United States)
Butterfly needle 21G	4056520-01	B.Braun (Germany)
Cell Culture Flask 25 cm^2	690 160	Greiner Bio-One (Germany)
Cell Culture Flask 75 cm^2	658 170	
Cell Culture Inserts 0.4 µm 12 mm diameter	PICM01250	Merck (Germany)
Cell strainer 40 and 100 µm	83.3945.040 83.3945.100	Sarstedt (Germany)
Cell Recovery Solution	354253	Corning (United States)
Citrate Buffer pH 6.0 20x Concentrate	005000	Thermo Fisher (United States)
Combi Tip advanced 0.5 ml	0030.089.782	Eppendorf (Germany)
Combi Tip advanced 5 ml	0030.089.812	
Complete Human Epithelial Cell Medium Kit	H6621	Cell Biologics (United States)

15 ml conical bottom tube	188 271	Greiner Bio-One (Germany)
50 ml conical bottom tubes	227 261	
Difco™ Skim Milk	232100	Becton Dickinson (United States)
DTT (CAS-No: 3483-12-3)	D0632	Merck (Germany)
Dynabeads™ Biotin Binder	11047	Thermo Fisher (United States)
DMEM (1x)	11960-044	Thermo Fisher (United States)
Eagle's Minimum Essential Medium (EMEM)	30-2003	ATCC (United States)
eBioscience™ Foxp3 / Transcription Factor Staining Buffer Set	00-5523-00	Thermo Fisher (United States)
EDTA (CAS-No: 6381-92-6)	108418	Merck (Germany)
EGTA (CAS-No: 67-42-5)	E3889	
FACS Clean solution	340345	Becton Dickinson (United States)
FACS Rinse solution	340346	
Falcon 5ml Round Bottom Polystyrene Test Tube, with Cell Strainer Snap Cap	352235	Corning (United States)
Feather Disposable Scalpel No 20	02.001.30.020	pfm medical (Japan)
Feather Disposable Scalpel No 11	02.001.70.011	
Fetal Bovine Serum (FBS)	10270-106	Life Technologies Gibco (United States)
Filter tip PP, premium surface, 0,1 -10 µl	06-693-530	Nerbe Plus (Germany)
Filter tip PP, premium surface, 0-20 µl	07-622-8300	
Filter tip PP, premium surface, 0-100 µl	07-642-8300	
Filter tip PP, premium surface, 0-200 µl	06-662-5300	
Filter tip PP, premium surface, 100-1,000 µl	06-693-5300	
Gelatin-Based Coating Solution	6950	Cell Biologics (United States)

Gelloader Pipette Tips 1-200 µl	70.1190.100	Sarstedt (Germany)
Glycerol (CAS-No: 56-81-5)	G2025	Merck (Germany)
HBSS	14175-053	Life Technologies Gibco (United States)
Heparin (2 mg/ml)	07980	STEMCELL Technologies (Canada)
HEPES Buffer Solution (1 M)	15630-056	ThermoFisher (United States)
Human Primary Alveolar Epithelial Cells	H-6053	Cell Biologics (United States)
Insulin syringe for U-100 Insulin (1 ml / 100 I.U.)	9161708V	Braun (Germany)
Insulin-Transferrin-Selenium (100x)	41400045	Thermo Fisher (United States)
Isoflurane 250 ml		Baxter (United States)
Ketaset 100 mg/ml injection solution		Zoetis (United States)
KPL True Blue Peroxidase Substrate	5510-0050	Sera care (Unites States)
L-Glutamine (200 mM)	17-605E	Lonza (Switzerland)
Lysing buffer 10x for RBC	555899	Becton Dickinson (United States)
LysoTracker™ Red DND-99	L7528	ThermoFisher (United States)
Matrigel Matrix	356231	Corning (United States)
MACS C Tubes	130-093-237	Miltenyi Biotech (Germany)
MEM alpha (1x)	41061-029	Thermo Fisher (United States)
MEM (2x) Modified Eagle Medium	21935-028	

MicroAmp™ Clear Adhesive Film	4306311	Applied Biosystems (United States)
MicroAmp™ Fast Optical 96-Well Reaction Plate, 0.1 mL	4346907	
Microscope Cover Glasses 22 x 22 mm 170±5 µm	LH24.1	Carl Roth (Germany)
Microscope slides 3x1 inch. Ground edges	03-0013/45	R. Langenbrinck GmbH (Germany)
Micro tube 0.5 ml	72.699	Sarstedt (Germany)
Micro tube 1.5 ml	72.690.301	
Micro tube 2 ml	72.691	
Micro tube 5 ml	72.701	
4–20% Mini-PROTEAN® TGX Stain-Free™ Protein Gels, 10 well, 50 µl	4568094	Bio Rad (United States)
14 ml PP Tube sterile	187261	greiner bio-one (Austria)
M-MLV Reverse Transcriptase Buffer	18057018	Thermo Fisher (United States)
Mouse Intubation Pack	000A3747	Hallowell EMC (United States)
MS columns	130-042-201	Miltenyi Biotech (Germany)
NaCl (CAS-No: 7647-14-5)	3957.1	Carl Roth (Germany)
NC-slide A8	942-0003	ChemoMetec (Denmark)
Neo-Clear™	1.09843.5000	Sigma-Aldrich (United States)
Nonidet P40	11754599001	Merck (Germany)
NucBlue™ Fixed Cell ReadyProbes™ Reagent (DAPI)	R37606	Thermo Fisher (United States)
Paraformaldehyde, 4% in PBS	J61899	Alfa Aesar (United States)
PCR 8er-CapStrips, colorless, domed	711040	Biozym (Germany)

PCR 8er-SoftStrips, 0.1 ml, colorless	711150	
Penicillin (10.000 U) - Streptomycin (10 mg/ml)	P0781-100ML	Sigma-Aldrich (United States)
Phosphatase Inhibitor Cocktail (100x)	5870S	Cell Signaling (United States)
Pierce™ ECL Western Blotting Substrate	32209	Thermo Fisher (United States)
pipette tips 10 µl, white	P866.1	Carl Roth (Germany)
pipette tips 200 µl, yellow	70.760.012	Sarstedt (Germany)
pipette tips 1,000 µl, blue	70.762.010	
Polypropylene Round-Bottom tube 5 ml	352063	Corning (United States)
Polystyrene Round-Bottom tube 5 ml	352054	
ProLong™ Glass Antifade Mountant	P36980	Thermo Fisher (United States)
10x Protease Inhibitor Cocktail (10x)	P2714-1BTL	Merck (Germany)
Quantikine ELISA mouse GM-CSF	SMGM00	R&D Systems (United States)
RNeasy MicroKit	74004	Qiagen (Germany)
RNaseOUT™ Recombinant Ribonuclease Inhibitor	10777019	Life Technologies (United States)
Roti®-Free Stripping Buffer	0083.1	Carl Roth (Germany)
SDS (CAS-No: 151-21-3)	L3771	Merck (Germany)
10 ml serological pipettes	607 180	Greiner Bio One (Germany)
25 ml serological pipettes	760 180	
50 ml serological pipettes	768 180	
Super Signal™ West Pico PLUS Chemiluminescent Substrate	34580	Thermo Fisher (United States)
SuperSignal™ West Femto Maximum Sensitivity Substrate	34094	
SYBR Green	172-5124	Bio Rad (United States)

SYTOX™ Blue Dead Cell Stain, for flow cytometry	S34857	Thermo Fisher (United States)
Trans-Blot Turbo Mini 0.2 µm PVDF Transfer Packs	1704156	Bio Rad (United States)
Tris	4855.2	Carl Roth (Germany)
10x Tris/Glycine/SDS	1610732	Bio Rad (United States)
Triton-X-100 (CAS-No: 9002-93-1)	X100	Merck (Germany)
Trypsin-EDTA 0.25% Solution (1X)	6914	Cell Biologics (United States)
Tween20 (CAS-No: 9005-64-5)	P7949	Merck (Germany)
Vicryl Plus 4-0 Needle/Suture combination	VCP304	Johnson & Johnson (United States)
96 Well Cell Culture Plate F-bottom	655 180	Greiner Bio One (Germany)
96 Well Cell Culture Plate U-bottom	650 180	
6 Well Cell Culture Plate	657 160	
24 Well Cell Culture Plate	662 160	
Xylariem 20 mg injection solution		Ecuphar GmbH (Germany)

9.2.3 Enzymes, recombinant proteins, inhibitors, and activators

AICA-Riboside (CAS-No.: 2627-69-2)	123040	Merck (Germany)
Compound C (CAS-No.: 866405-64-3)	171260	
Dispase	354235	Corning (United States)
DNAse (5 mg/ml)	1853502	Serva (Germany)
MHY1485 (CAS-No.: 326914-06-1)	SML0810	Merck (Germany)
Rapamycin (CAS-No.: 53123-88-9	R0395	Merck (Germany)
Recombinant Human GM-CSF Protein	215-GM	R&D Systems (United States)
Recombinant Mouse GM-CSF Protein	415-ML	

ROCK inhibitor (Y-27632)	72302	STEMCELL Technologies (Canada)
TPCK-Trypsin (1 mg/ml)	20233	Thermo Fisher (United States)
Trypsin (0.05%) – EDTA (0.02%) in PBS (without Ca^{2+}, Mg^{2+})		Universitätsklinik Gießen

9.2.4 Media and buffer

growth medium MDCKII cells and murine AECs

Reagent	Concentration
DMEM (1x)	
FCS	10%
Penicillin (100 U/ml) /Streptomycin (10 mg/ml)	1%
L-Glutamin (200 mM)	1%

growth medium MRC-5 cells

Reagent	Concentration
Eagle's Minimum Essential Medium (EMEM)	
FCS	10%

growth medium human AECs

Reagent	Concentration
F-12 Nut Mix (Ham) (1x)	
FCS	10%
Penicillin (100 U/ml) /Streptomycin (10 mg/ml)	1%
L-Glutamin (200 mM)	1%
Amphotericin B (250 µg/ml)	1%

In the infection media for murine and human AEC, FCS in the growth medium was replaced by 0.2% BSA. TPCK-Trypsin (1mg/ml) was added in a dilution of 1:2,000 in human and 1:1,500 in murine AEC infection medium.

mouse organoid medium

Reagent	**Concentration**
αMEM (1x)	
FCS	10%
Penicillin (100 U/ml) /Streptomycin (10 mg/ml)	1%
L-Glutamine (200 mM)	1%
Insulin-Transferrin-Selenium (100X)	1%
Heparin (2 mg/ml)	0.1%

human alveolosphere medium

Reagent	**Concentration**
Small Airway Epithelial Cell Growth Medium (SAGM™)	
Penicillin (100 U/ml) /Streptomycin (10 mg/ml)	1%
FCS	5%

Plaque Assay overlay medium

Reagent	**Concentration/ dilution**
MEM (2x)	
Avicell 2.5% in ddH_2O	50%
Penicillin (100 U/ml) /Streptomycin (10 mg/ml)	1%
L-Glutamin (200 mM)	1%
TPCK-Trypsin (1 mg/ml)	1:1000

Western Blot loading buffer

Reagent	Concentration
ddH_2O	
Tris	150 mM
SDS	7.5%
Glycerol (99%)	37.5%
DTT	500 mM

adjusted to pH 6.8, bromophenol blue was added as a marker

NP40 lysis buffer

Reagent	Concentration
H_2O	
Tris	20 mM
NaCl	150 mM
EDTA (pH 8.0)	1 mM
EGTA (pH 8.0)	1 mM
NP40	0.5%
Sodium Orthovanadat (pH 10.0)	1 mM

MACS buffer

Reagent	Concentration
PBS-/-	
EDTA	1 mM
FCS	0.5%

adjusted to pH 7.2

FACS buffer

Reagent	Concentration
MACS buffer	
NaN_3	0.1%

adjusted to pH 7.4

9.2.5 Antibodies

9.2.5.1 Antibodies for FACS

The target species for all listed antibodies is the mouse.

Target	**Flurochrome / dye**	**Clone**	**Isotype**	**Host species**	**Catalogue number**	**Company**
CD31	AF488	MEC 13.3	IgG2a, κ	rat	102514	Biolegend
CD45	FITC	30-F11	IgG2b, κ	rat	553080	BD Biosciences
CD31	PE	MEC 13.3	IgG2a, κ	rat	553373	
CD45	PE	30-F11	IgG_{2b}, κ	rat	553081	
CD326 (EpCAM)	APC-Cy7	G8.8	IgG2a, κ	rat	118218	Biolegend
	APC-eFluor 780	G8.8	IgG2a, k	rat	47-5791-80	Thermo Fisher
CD24	Pacific Blue	M1/69	IgG2b, κ	rat	101820	Biolegend
	PE-Cy7	M1/69	IgG2b, κ	rat	101822	
Ly-6A/E (Sca-1)	APC	E13-161.7	IgG2a, κ	rat	122512	
	Pacific Blue	D7	IgG2a, κ	rat	108120	
T1α	APC	8.1.1	IgG2a, κ	syrian hamster	127410	
Ki67	PE	16A8	IgG2a, κ	rat	652404	
Isotype	PE	RTK2758	IgG2a, κ	rat	400508	

9.2.5.2 Antibodies *for cell purification and cell culture*

The target species for all listed antibodies is the mouse.

Target	**Label**	**Clone**	**Isotype**	**Host species**	**Catalogue number**	**Company**
CD45	biotinylation	30-F11	IgG2b, κ	rat	553078	BD Biosciences
CD16/32	biotinylation	2.4G2	IgG2b, κ	rat	553143	
CD31	biotinylation	MEC13.3	IgG2a, κ	rat	553371	
GM-CSF	unlabeled	MP122E9	IgG2a	rat	MAB415	R&D Systems
Isotype	unlabeled	54447	IgG2a	rat	MAB006	

9.2.5.3 Antibodies for Western Blot and immunohistochemistry staining

Antibody	**Catalogue number**	**Company**
Anti-rabbit IgG, HRP-linked Antibody	7074	Cell Signaling
AMPKα Rabbit Antibody	2532	
Phospho-Acetyl-CoA Carboxylase (Ser79) Rabbit Antibody	3661	
p70 S6 Kinase Rabbit Antibody	9202	
Phospho-p70 S6 Kinase (Thr389) Rabbit Antibody	9205	
GAPDH (14C10) Rabbit mAb	2118	
Rabbit anti-mouse p-mTOR (Ser2448)	SAB5700327	Merck
Rat anti-mouse RAGE	MAB1179	R&D Systems
Mouse anti-mouse Hop	sc-398703	Santa Cruz
Rabbit anti-mouse ProSPC	WRAB-9337	Seven Hills
Rabbit anti-mouse p-ACC (Ser79)	PA5-17725	Invitrogen
Goat anti-rabbit IgG AF555	A-32732	
Donkey anti-rabbit IgG AF488	A-32790	

Chicken anti-rat IgG AF647	A-21472	
Rat anti-Ki67 IgG (for paraffin sections)	14-5698-82	
Goat anti-rat AF555 (for paraffin sections)	A-48263	
Rabbit anti-ProSPC (for paraffin sections)	ab90716	abcam
Donkey anti-rabbit AF647 (for paraffin sections)	ab150075	
Mouse anti-mouse ProSPC	ab167608	
Rabbit anti-mouse Cav-1	ab2910	
Goat anti-mouse IgG AF647	ab150115	
Goat anti-Mouse IgG (HRP)	ab6789	

9.3 List of Abbreviations

A	
A	ampere
ACC	acetyl coenzyme A carboxylase
ADI	alveolar intermediate cells
ADP	adenosine diphosphate
AEP	alveolar epithelial progenitors
AECI	alveolar epithelial cell type I
AECII	alveolar epithelial cell type II
AM	alveolar macrophage
AMP	adenosine monophosphate
AMPK	adenosine monophosphate kinase
ARDS	acute respiratory distress syndrome
ATP	adenosine triphosphate
Axin2	Axin-like protein
B	
BALF	bronchioalveolar lavage fluid
BASC	bronchioalveolar stem cell
BMDM	bone marrow-derived macrophages
BSA	bovine serum albumin
C	
C	celsius
Ccl2	C-C-chemokine ligand 2
Ccnd1	cyclin D1
CCR2	C-C chemokine receptor type 2
CC10	uteroglobin
Cdk1	cyclin dependent kinase 1
cDNA	copy deoxyribonucleic acid
Cldn4	Claudin 4
c-Met	mesenchymal-epithelial transition factor
CPAP	continuous positive airway pressure
Csf2	colony-stimulating factor 2
Csf2rα	colony-stimulating factor 2 receptor α
Csf2rβ	colony-stimulating factor 2 receptor β
CXCL9	C-X-C motif chemokine ligand 9
CXCL10	C-X-C motif chemokine ligand 10
CX_3CR1	C-X3-C motif chemokine receptor 1
CX43	connexin 43
D	
DC	dendritic cell
dNTP	deoxyribonucleotide triphosphate
DR5	death receptor 5
E	
EGFR	epidermal growth factor receptor
eIF4E	eukaryotic initiation factor 4E
eIF4F	eukaryotic initiation factor 4F
ENaC	epithelial sodium channel
EpCAM	epithelial cellular adhesion molecule

4EBP1	eukaryotic initiation factor 4E (eIF4E)-binding protein 1
F	
FACS	fluorescence-activated cell sorting
FcyR	Fcy receptor
FCS	fetal calf serum
FFU	foci forming unit
Fgf	fibroblast growth factor
Fgfr	fibroblast growth factor receptor
FIO2	fraction of inspired oxygen
G	
GM-CSF	granulocyte-macrophage colony-stimulating factor
H	
HA	haemagglutinin
hAEC	human alveolar epithelial cells
H&E	hematoxylin and eosin
HGF	hepatocyte growth factor
HIF1α	hypoxia-inducible factor 1α
HPAI	highly pathogenic avian influenza A
H_2O_2	hydrogen peroxide
I	
IAV	influenza A virus
IBV	influenza B virus
ICAM1	intercellular adhesion molecule 1
ICV	Influenza C virus
IFN	interferon
IFNAR	interferon alpha receptor
IL	interleukin
J	
JAK-STAT	janus kinase-signal transducer and activator of transcription
K	
KEGG	Kyoto Encyclopedia of Genes and Genomes
Krt5	Keratin 5
Krt8	keratin 8
L	
Lats2	large tumor suppressor kinase 2
LNEP	lineage-negative epithelial progenitors
LPS	lipopolysaccharide
M	
M2	matrix protein 2
mAEC	murine alveolar epithelial cell
MAPK	mitogen-activated protein kinase
MCC	mucociliary clearance
MDCKII	Madin-Darby canine kidney cells
Mki67	marker of proliferation KI 67
MLN	mediastinal lymph node
MRC-5	Medical Research Council cell strain 5
Mst1/2	mammalian sterile 20-like kinases 1 and 2
mTORC1	mechanistic target of rapamycin complex 1

N	
NA	neuraminidase
NADPH	nicotinamide adenine dinucleotide phosphate
NA+, K+-ATPase	sodium, potassium-adenosine triphosphatase
NET	neutrophil extracellular traps
NHS	normal horse serum
NIV	nonpharmaceutical interventions
NK-cell	natural killer cell
NO	nitric oxide
NOS	nitric oxide species
NOX2	NADPH oxidase complex
NS-1	non-structural protein 1
P	
PAGE	polyacrylamide gel electrophoresis
PaO2	arterial partial pressure of oxygen
PAP	pulmonary alveolar proteinosis
PCA	principal component analysis
PDGFRα	platelet-derived growth factor receptor α
PEEP	positive end-expiratory pressure
PFA	paraformaldehyde
PI3K	phosphoinositide 3-kinase
PKB/Akt	proteinkinase B
Plet1	placenta-expressed transcript 1
PNEC	pulmonary neuroendocrine cell
PPARγ	peroxisome proliferator-activated receptor γ
p70S6K	70-kDa ribosomal protein S6 kinase
Q	
qPCR	quantitative real-time polymerase chain reaction
R	
RAS	respiratory airway secretory
rhGM-CSF	recombinant human GM-CSF
rMC	resident mesenchymal cell
RNA	ribonucleic acid
RNA-seq	RNA-sequencing
ROS	reactive oxygen species
RT	room temperature
S	
S2448	serine 2448
SCGB1A1	secretoglobin family 1A member 1
sec	second
SFTPC	surfactant protein C
SPDEF	Sam-pointed domain-containing Ets-like factor
SPF	specific-pathogen-free
T	
T cell	thymus cell
TCR	T cell receptor
TEAD	transcriptional enhanced associate domain
T_{FH}	T follicular helper
Tgf	transforming growth factor

Tgf-α	transforming growth factor-α
T_H	T helper
TLR	toll-like receptor
TNF	tumor necrosis factor
TNFα	tumor necrosis factor α
TRAIL	tumor-necrosis-factor-related apoptosis-inducing ligand
TR-AM	tissue-resident alveolar macrophages
Trp63	transformation related protein 63
V	
V	volt
VCAM1	vascular cell adhesion molecule 1
VEGF	vascular endothelial growth factor
W	
WHO	world health organization
Wnt	wingless-related integration site
WT	wild type

9.4 Acknowledgements

First and foremost, I want to thank my supervisor, Prof. Dr. Susanne Herold, for providing me with the topic of my PhD project and giving me the opportunity to work in such an interesting field. Thank you for the valuable advice, insightful discussions, and guidance throughout the project. During my doctoral studies, I had the best conditions and access to all the resources necessary for my scientific work. Thank you for that!

My thanks also go to Ana Ivonne Vazquez-Armendariz for her support throughout my PhD journey and for supervising me during the first years. Your excellent advice and significant recommendations greatly benefited my experiments and the overall project.

Moreover, I want to thank PD Dr. Torsten Hain and his his team at the Institute of Medical Microbiology at Justus-Liebig-University Giessen for conducting the bulk RNA sequencing and subsequent data analysis.

Special thanks to Ioannis Alexopoulos, head of the Imaging Unit at the Institute for Lung Health (ILH) at Justus-Liebig-University Giessen, for his support with image acquisition and analysis.

At this point, I would also like to thank the PostDocs from our group: Ulrich Matt, Irina Kuznetsova, Learta Pervizaj-Oruqaj, Maximiliano Ferrero, Christina Malainou, and Margarida Barroso. You contributed to the project by supporting me whenever I had struggles or any scientific questions. I would like to specifically mention Monika Heiner, who frequently discussed my PhD project with me and gave me profound scientific advice.

I am also thankful to my fellow PhD students Julian, Mo, and Anna-Lena for our discussions about our projects and experiments. It was a pleasure to attend the MBML graduate school alongside you. I would especially like to thank Ludmilla Sperling, who contributed to the generation of the data in Figure 4.1.

And I want to acknowledge the excellent technical support provided by Larissa Hamann, Florian Lück, Julia Stark, Josefine Guth, Stefanie Jarmer, and Hannah Hofmann - your expertise was essential to this work.

Außerdem möchte ich meinen Eltern und meiner Schwester dafür danken, dass sie mich seit dem ersten Tag meines Studiums immer unterstützt haben. Ohne euch wäre diese Doktorarbeit nicht möglich gewesen.

Und vielen Dank Martin für deine Geduld während der letzten Jahre. Du hast mich immer motiviert und an mich geglaubt. Ich weiß nicht, wie ich es ohne deine Unterstützung und Ermutigungen hätte schaffen können.

9.5 Affirmation

Hiermit erkläre ich, dass ich die vorliegende Arbeit selbständig und ohne unzulässige Hilfe oder Benutzung anderer als der angegebenen Hilfsmittel angefertigt habe. Alle Textstellen, die wörtlich oder sinngemäß aus veröffentlichten oder nichtveröffentlichten Schriften entnommen sind, und alle Angaben, die auf mündlichen Auskünften beruhen, sind als solche kenntlich gemacht. Bei den von mir durchgeführten und in der Dissertation erwähnten Untersuchungen habe ich die Grundsätze guter wissenschaftlicher Praxis, wie sie in der „Satzung der Justus-Liebig-Universität Gießen zur Sicherung guter wissenschaftlicher Praxis“ niedergelegt sind, eingehalten sowie ethische, datenschutzrechtliche und tierschutzrechtliche Grundsätze befolgt. Ich versichere, dass Dritte von mir weder unmittelbar noch mittelbar geldwerte Leistungen für Arbeiten erhalten haben, die im Zusammenhang mit dem Inhalt der vorgelegten Dissertation stehen. Die vorgelegte Arbeit wurde weder im Inland noch im Ausland in gleicher oder ähnlicher Form einer anderen Prüfungsbehörde zum Zweck einer Promotion oder eines anderen Prüfungsverfahrens vorgelegt. Alles aus anderen Quellen und von anderen Personen übernommene Material, das in der Arbeit verwendet wurde oder auf welches direkt Bezug genommen wird, wurde als solches kenntlich gemacht. Insbesondere wurden alle Personen genannt, die direkt und indirekt an der Entstehung der vorliegenden Arbeit beteiligt waren. Mit der Überprüfung meiner Arbeit durch eine Plagiatserkennungssoftware bzw. ein internetbasiertes Softwareprogramm erkläre ich mich einverstanden.

Gießen, den _____ _____

Theresa Schäfer